

Exploration of Electrolytes for Zn Anode Rechargeable Batteries: Room Temperature Ionic  
Liquids as Major or Supporting Components

by

Min Xu

A thesis submitted in partial fulfillment of the requirements for the degree of

Doctor of Philosophy

in Materials Engineering

Department of Chemical and Materials Engineering

University of Alberta

© Min Xu, 2014

## Abstract

For Zn anode rechargeable batteries, there are a number of shortcomings associated with using traditional KOH aqueous electrolytes. These include drying-out of the electrolyte due to water evaporation and dendrite formation at the Zn electrode during recharging, which severely impair battery performance (e.g., cycle life and capacity) and limit their application. In particular, to solve the problem of dendrite formation that could cause short-circuit issues, many attempts have been made to modify the Zn electrode and the electrolyte, as well as to choose a desirable and robust separator. However, no breakthrough has been achieved on the basis of conventional KOH aqueous electrolytes. It is, therefore, critical to either modify conventional KOH aqueous electrolytes or explore alternative electrolytes to eliminate these bottlenecks to the development of a feasible Zn anode rechargeable battery system. Room temperature ionic liquids (RTILs) in recent years have been increasingly recognized as potential electrolytes or electrolyte components for rechargeable batteries. Applying non-volatile RTILs as electrolytes provides potential benefits of achieving a longer service life, as drying out due to water evaporation is no longer a problem. Furthermore, RTILs demonstrate the capacity to modify metal deposit morphology, which may contribute greatly to preventing Zn dendrite formation and improving battery cycle life. On the other hand, compared with alkaline electrolytes, a simple electrolyte system composed of an RTIL as the sole component faces the challenge of enhancing its low conductivity (one to two orders of magnitude lower than aqueous electrolytes) before it can be practically applied in a battery.

With the purpose of developing electrolyte systems that can harness the benefits from both RTILs (Zn morphology control) and aqueous electrolytes (rapid Zn redox kinetics), two groups of electrolytes are investigated in this study. One is based on RTILs, composed of pyrrolidinium

or imidazolium cations and bis(trifluoromethanesulfonyl)imide or dicyanamide anions, with the incorporation of diluents (water and/or dimethyl sulfoxide (DMSO)). Another one adopts RTILs as additives to modify conventional KOH aqueous electrolytes. A larger portion of this work was focused on the former group. By applying cyclic voltammetry (CV), potentiodynamic polarization and chronoamperometry (CA), the kinetics, reversibility and cyclability of Zn redox behavior is explored in the studied electrolytes. The morphology of Zn deposits is observed and analyzed using scanning electron microscopy (SEM). With respect to RTIL-based electrolytes, conductivity measurements, together with Fourier transform infrared spectroscopy (FTIR), differential scanning calorimetry (DSC) and gas-phase density functional theory (DFT) are performed to investigate water interaction with RTIL ions and to shed light on the mechanisms for improved Zn redox behavior with water addition.

For RTIL-based electrolytes, to balance the pros (improved electrolyte conductivity and Zn redox kinetic performance) and cons (reduced electrochemical stability of RTILs) of adding diluent(s) is of great importance in the development of workable electrolyte systems. Among six kinds of studied RTILs, i.e., 1-butyl-1-methylpyrrolidinium bis(trifluoromethanesulfonyl)imide (BMP-TFSI), 1-methyl-1-propylpyrrolidinium bis(trifluoromethanesulfonyl)imide (MPrP-TFSI), 1-methyl-1-pentylpyrrolidinium bis(trifluoromethanesulfonyl)imide (MPP-TFSI), 1-ethyl-3-methylimidazolium bis(trifluoromethanesulfonyl)imide (EMI-TFSI), 1-butyl-1-methylpyrrolidinium dicyanamide (BMP-DCA) and 1-ethyl-3-methylimidazolium dicyanamide (EMI-DCA), an electrolyte system composed of EMI-DCA with the addition of both water and DMSO at a mole ratio of EMI-DCA:H<sub>2</sub>O:DMSO = 1:1.1:2.3 exhibits the best performance in terms of electrolyte conductivity, electrochemical properties for Zn redox reactions and Zn deposit morphology.

For conventional alkaline aqueous electrolytes, adding an appropriate RTIL as the electrolyte additive can effectively eliminate Zn dendrite formation during electrodeposition. It is worth noting that hydrophilic RTILs are better relative to hydrophobic RTILs when it comes to obtaining desirable Zn morphologies and preventing dendritic Zn formation. An electrolyte composed of 9.0 M KOH + 5.0 wt% ZnO with a hydrophilic RTIL, i.e., 0.5 wt% EMI-DCA, appears to be a promising electrolyte system. These results give insights into developing novel alkaline aqueous electrolytes, which are deliberately modified with hydrophilic RTILs, for Zn anode rechargeable batteries.

## Preface

### (Mandatory due to collaborative work)

This thesis research was conducted at the Environment, Mining and Energy, National Research Council (EME-NRC) in Vancouver, BC, Canada. The identification of this research program was accomplished by my supervisor, Professor Douglas G. Ivey (University of Alberta, UA), together with Wei Qu and Zhong Xie from EME-NRC. The technical apparatus used for this research was setup by myself, with the assistance of Wei Qu, Zhong Xie and Yong-Hong Bing (previous research associate in EME-NRC). The literature review in Chapter 2, and the performance of experiments and the collection and analysis of research data in Chapters 3-6 are my original work, with some contribution from Eben Dy and Xiao-Zi Yuan as stated in detail below.

Chapter 3 of this thesis includes two published papers. One is a Journal paper, i.e., M. Xu, D.G. Ivey, Z. Xie, W. Qu, *Electrochimica Acta* 89 (2013) 756-762; another one is a conference proceedings paper, i.e., M. Xu, D.G. Ivey, W. Qu, Z. Xie, Y.H. Bing, *ECS Transactions*, 50 (25) 13-22 (2013). I was responsible for the data collection and analysis as well as the manuscript composition. Professor Douglas G. Ivey, Wei Qu and Zhong Xie contributed to manuscript editing. Yong-Hong Bing assisted with SEM image collection.

Chapter 4 of this thesis includes one conference proceedings paper, i.e., M. Xu, D.G. Ivey, W. Qu, Z. Xie, X.Z. Yuan, *ECS Transactions* 53 (36) 41-50 (2013), with a full paper published, i.e., M. Xu, D.G. Ivey, W. Qu, Z. Xie, E. Dy, X.Z. Yuan, *Journal of The Electrochemical Society*, 161 (1) A128-A136 (2014). Chapter 4 also includes a Journal paper, i.e., M. Xu, D.G. Ivey, Z. Xie, W. Qu, E. Dy, *Electrochimica Acta*, 97 (2013) 289-295. I was responsible for the majority of data collection and analysis as well as the manuscript composition. Eben Dy was responsible for modeling data analysis and involved with manuscript composition regarding DFT calculations. Xiao-Zi Yuan contributed to the manuscript in terms of the conductivity measurements. Professor Douglas G. Ivey, Wei Qu and Zhong Xie contributed to concept formulation and manuscript editing.

Chapter 5 includes one published Journal paper, i.e., M. Xu, D.G. Ivey, W. Qu, Z. Xie, *Journal of Power Sources*, 252 (2014) 327-332. I was responsible for the data collection and analysis as

well as the manuscript composition. Professor Douglas G. Ivey, Wei Qu and Zhong Xie contributed to concept formulation and manuscript editing.

Chapter 6 includes a book chapter, i.e., M. Xu, D.G. Ivey, W. Qu, Z. Xie, E. Dy, Exploration of electrolytes for Zn-anode rechargeable batteries: room temperature ionic liquids as major or supporting components, in: *Ionic Liquids: Synthesis, Characterization and Applications*, A. Brooks (Eds.), Nova Science Publishers, Inc., 2014. I was responsible for the data collection and analysis as well as the manuscript composition. Eben Dy contributed to the manuscript through DFT calculations. Professor Douglas G. Ivey, Wei Qu and Zhong Xie contributed to concept formulation and manuscript editing.

## Acknowledgements

My PhD study has been a memorable life experience. When I reflect on these past four years, the excitement when I began this PhD program, the feelings of encouragement and frustration with the experimental results and the feelings of happiness and discouragement from reviewers' decisions for our submitted Journal papers all come to my mind and all had value. I would like to take this opportunity to give my sincere appreciation to all who have generously given me their support over the years and shared this life journey with me.

First, I must thank my supervisor, Professor Douglas G. Ivey, for providing me with this interesting research project. I am very grateful for his patient guidance and thoughtful encouragement during my PhD study. I feel lucky to have a supervisor who cares about my research progress and always gives insightful feedback to my work promptly. I must also express my gratitude to Wei Qu and Zhong Xie (EME-NRC) for their unreserved and significant assistance in steering my experimental direction, without which this research work could not have progressed smoothly. Their astute comments to my work have aided me in deepening my understanding of electrochemistry. I would like to extend my thanks to Yong-Hong Bing, Eben Dy, Xiao-Zi Yuan and Zheng Shi from EME-NRC for their brainstorming ideas related to my research project. I especially acknowledge Eben Dy for his time and effort in providing modeling data to explain my experimental results. I thank Xiao-Zi Yuan for her supportive comments and advice regarding my electrochemistry experiments. During the path of my research, I have enjoyed the scientific discussions during regular meetings with the group members mentioned above; these discussions have significantly aided my learning and growing as a researcher.

I thank all who have offered me their technical support for the fulfillment of my experiments. I am grateful to Banafsheh Babakhani (former PhD student from Professor Douglas G. Ivey's group) and Nima Shaigan (EME-NRC), who shared with me their experiences in and knowledge of electrodeposition. I thank Dave Edwards, Mark Robertson and Eben Dy (EME-NRC), who added to my knowledge in differential scanning calorimetry (DSC), scanning electron microscopy (SEM), X-ray diffraction (XRD) and Fourier transform infrared spectroscopy (FTIR), and trained me to use these techniques. In addition, I am grateful to Ken Tsay for his help with conductivity measurements. My gratitude is extended to Derrick Horne from the UBC Bioimaging Facility for his assistance and training with the field emission SEM. Special

appreciation is given to Brian McLernon and David Semczyszyn (EME-NRC) for their kind mentoring in Western culture and arts, which have greatly enriched my experience at EME-NRC.

The financial support from the Transportation Development Centre of Transport Canada, the International Zinc Association (IZA) and the Natural Sciences and Engineering Research Council (NSERC) is gratefully acknowledged. I would also like to express my sincere appreciation to EME-NRC for providing access to laboratory facilities to carry out the research work for my PhD project.

Finally, I want to thank my parents and parents-in-law for their love and encouragement throughout my graduate study. I also want to express my special thanks to my husband Jun Ou. I am really blessed that we were able to carry out our PhD studies together. I thank him for caring about me greatly in my daily life through the years. Knowing that he is always there to share my burdens and happiness has provided the strong support needed to complete my PhD journey.

## Table of Contents

Chapter 1 Introduction .....	1
1.1 Background .....	1
1.2 Structure of thesis .....	3
Chapter 2 Literature review .....	6
2.1 Zn anode rechargeable batteries: Advantages and limitations.....	6
2.1.1 Typical Zn anode rechargeable batteries and their advantages .....	6
2.1.2 Limitations for commercializing Zn anode rechargeable batteries.....	8
2.1.3 Summary .....	16
2.2 Room temperature ionic liquids (RTILs) and their applications .....	18
2.2.1 Structure and physicochemical properties of RTILs .....	18
2.2.2 Application of RTILs in electrodeposition and energy storage devices .....	24
2.2.3 Summary .....	27
2.3 Novel electrolyte systems for Zn anode rechargeable batteries.....	27
2.3.1 Functionalized RTILs systems.....	27
2.3.2 Mixed electrolyte systems.....	28
2.3.3 Summary .....	29
Chapter 3 Preliminary characterization of selected RTILs: Study of Zn redox behavior .....	30
3.1 Overview .....	30
3.2 Experimental methods .....	30
3.2.1 DSC measurements.....	30
3.2.2 Electrochemical measurements.....	31
3.2.3 SEM observation.....	32
3.3 Results and discussion .....	32
3.3.1 Thermal properties for each blank RTIL .....	32

3.3.2 Electrochemical window for each blank RTIL .....	32
3.3.3 Electrochemistry of Zn in studied RTILs .....	33
3.4 Summary .....	44
Chapter 4 Electrolytes composed of water added RTILs with TFSI <sup>-</sup> anions.....	46
4.1 Overview.....	46
4.2 Experimental methods .....	46
4.2.1 Conductivity Measurements .....	47
4.2.2 FTIR Measurements.....	47
4.2.3 DSC Measurements .....	47
4.2.4 Electrochemical Measurements .....	48
4.2.5 First-principles modeling.....	48
4.2.6 Electrodeposition and SEM .....	49
4.3 Results and discussion .....	49
4.3.1 Conductivity dependence of studied RTILs with water addition .....	49
4.3.2 Kinetic properties and reversibility for Zn redox reactions .....	52
4.3.3 Zn deposit morphology in studied RTILs without or with water addition .....	59
4.4 Summary .....	61
Chapter 5 Electrolytes composed of water and dimethyl sulfoxide added RTILs with DCA <sup>-</sup> anions.....	63
5.1 Overview.....	63
5.2 Experimental methods .....	63
5.2.1 Conductivity measurements.....	64
5.2.2 Electrochemical measurements.....	64
5.2.3 SEM and XRD observations.....	64
5.3 Results and discussion .....	65

5.3.1	Conductivities of water and/or DMSO added EMI-DCA electrolytes .....	65
5.3.2	Mechanisms for Zn redox reactions in EMI-DCA with water and DMSO .....	66
5.3.3	Zn deposit morphology in EMI-DCA with water and/or DMSO addition .....	72
5.4	Summary .....	74
Chapter 6	Electrolytes based on KOH aqueous solution with addition of RTILs with EMI <sup>+</sup> cations .....	75
6.1	Overview .....	75
6.2	Experimental methods .....	75
6.2.1	Electrochemical measurements .....	76
6.2.2	Electrodeposition and SEM .....	76
6.3	Results and discussion .....	76
6.3.1	Comparison of EMI-TFSI and EMI-DCA as additives in alkaline electrolytes .....	76
6.3.2	Zn morphology as a function of EMI-DCA concentration and current density .....	78
6.3.3	Mechanisms of Zn morphology control in alkaline electrolytes with EMI-DCA .....	82
6.4	Summary .....	84
Chapter 7	Conclusions and Recommendations .....	86
7.1	Electrolyte system based on RTILs with the addition of diluents .....	86
7.2	Electrolyte system based on alkaline aqueous solutions with the addition of RTILs .....	89
References	.....	92

## List of Tables

Table 1-1 Structure and physicochemical properties of the studied RTILs.....	3
Table 2-1 Comparison of specific energy/power for Zn anode batteries and Li-based batteries ...	6
Table 2-2 Passivation sub-mechanisms for a porous Zn anode (summarized according to [43])	14
Table 2-3 Typical cations for RTILs .....	19
Table 2-4 Typical anions for RTILs .....	20
Table 3-1 Cathodic/anodic limit potentials for studied RTILs .....	33
Table 3-2 Characterization of Zn redox in four RTILs.....	36
Table 3-3 Kinetic parameters for Zn redox reactions in four RTILs .....	40
Table 4-1 Kinetic properties for Zn redox in three RTILs with TFSI <sup>-</sup> anions.....	56
Table 4-2 Gas-phase binding energies between BMP <sup>+</sup> , TFSI <sup>-</sup> and Zn <sup>2+</sup> and H <sub>2</sub> O species determined by B3LYP/6-311G(df,p) DFT calculations .....	57
Table 4-3 Charge integrated for Zn redox in three RTILs with TFSI <sup>-</sup> anions before and after water addition.....	57
Table 5-1 Electrochemical behavior of Zn redox in EMI-DCA based electrolytes .....	68
Table 6-1 Kinetic properties for Zn redox in 9.0 M KOH + 5.0 wt% ZnO added with EMI-DCA .....	80

## List of Figures

Fig. 2-1 Electrodeposit morphology on the surface of a Zn electrode from (a) an electrolyte with no additives and (b) an electrolyte containing 0.12 g/L $\text{Sn}^{2+}$ [37].	10
Fig. 2-2 Functional imidazolium salts for task-specific ionic liquids [74].	20
Fig. 2-3 Viscosity at 20°C of co-solvents and BMI- $\text{BF}_4$ mixtures vs. mole fraction of co-solvents [88].	22
Fig. 3-1 DSC traces for the four blank RTILs.	32
Fig. 3-2 CV results for the four blank RTILs (at a scan rate of 500 mV/s).	33
Fig. 3-3 CV results for 0.1 M $\text{Zn}^{2+}$ in (a) BMP-TFSI, (b) MPP-TFSI, (c) EMI-TFSI and (d) BMP-DCA at different scan rates (20 mV/s, 50 mV/s and 100 mV/s).	35
Fig. 3-4 CV results (3 cycles at 100 mV/s) for 0.1 M $\text{Zn}^{2+}$ in (a) BMP-TFSI, (b) MPP-TFSI, (c) EMI-TFSI and (d) BMP-DCA.	37
Fig. 3-5 Polarization curves obtained at a scan rate of 1 mV/s for Zn species in RTILs: (a) BMP-TFSI, (b) MPP-TFSI, (c) EMI-TFSI and (d) BMP-DCA.	39
Fig. 3-6 Relationship of current vs. $t^{1/2}$ for chronoamperometry experiments for Zn species reduced in the four studied RTIL.	42
Fig. 3-7 CV cycling at 10mV/s for 100 cycles (# refers to cycle number): (a) BMP-TFSI, (b) MPP-TFSI, (c) EMI-TFSI and (d) BMP-DCA.	43
Fig. 3-8 SEM secondary electron (SE) images of Zn deposits after CV cycling from RTILs: (a) BMP-TFSI, (b) MPP-TFSI, (c) EMI-TFSI and (d) BMP-DCA.	44
Fig. 4-1 Conductivity of studied RTILs with different amounts of water.	49
Fig. 4-2 FTIR spectra for each RTIL with different amounts of water additions: (a) BMP-TFSI, (b) MPrP-TFSI and (c) EMI-TFSI.	50
Fig. 4-3 DSC traces for each RTIL with different amounts of water additions: (a) BMP-TFSI, (b) MPrP-TFSI and (c) EMI-TFSI (M, M' and $M_0$ denote melting peaks).	51
Fig. 4-4 CV results for the electrochemical window in: (a) BMP-TFSI, (b) MPrP-TFSI and (c) EMI-TFSI.	53

Fig. 4-5 CV results for Zn redox in: (a) BMP-TFSI, (b) MPrP-TFSI and (c) EMI-TFSI. ....	55
Fig. 4-6 Current vs. time curves (left) and Tafel plots (right) for Zn redox in each RTIL with water additions: (a) BMP-TFSI, (b) MPrP-TFSI and (c) EMI-TFSI.....	56
Fig. 4-7 B3LYP/6-311+G(2d,2p) optimized geometric structures for: (a) $Zn(H_2O)^{2+}$ , (b) $Zn(H_2O)_2^{2+}$ , (c) $Zn(H_2O)_6^{2+}$ and (d) $Zn(H_2O)_6^{2+}$ with the Polarizable Continuum Model used to approximate the effect of additional layers of water molecules; (e) $BMP^+-H_2O$ , (f) $TFSI-H_2O$ , (g) $BMP^+-TFSI$ , (h) $Zn(TFSI)^+$ , (i) $Zn(TFSI)_2$ , (j) $Zn(TFSI)_2(H_2O)$ , (k) $Zn(TFSI)_2(H_2O)_2$ and (l) $Zn(TFSI)_2(H_2O)_2^+OH_2$ .....	59
Fig. 4-8 SEM SE images of Zn deposits prepared by potentiostatic deposition from: (a) BMP-TFSI, (b) MPrP-TFSI, (c) EMI-TFSI, (d) BMP-TFSI with 2.0 wt% $H_2O$ , (e) MPrP-TFSI with 2.0 wt% $H_2O$ and (f) EMI-TFSI with 2.5 wt% $H_2O$ .....	60
Fig. 5-1 Conductivity of EMI-DCA with addition of water and/or DMSO. ....	65
Fig. 5-2 CV plots at 50 mV/s for Zn redox in EMI-DCA based electrolytes: (a) E: EMI-DCA, (b) $W_1$ : EMI-DCA + $H_2O$ (1:1.1), (c) $W_2$ : EMI-DCA + $H_2O$ (1:6.6), (d) D: EMI-DCA + DMSO (1:2.3), (e) $D/W_1$ : EMI-DCA + $H_2O$ + DMSO (1:1.1:2.3), (f) $D/W_2$ : EMI-DCA + $H_2O$ + DMSO (1:6.6:2.3) and (g) electrochemical window for each electrolyte in the absence of Zn ions.....	67
Fig. 5-3 Cyclability of Zn redox in EMI-DCA based electrolytes at 10 mV/s: (a) E: EMI-DCA, (b) $W_1$ : EMI-DCA + $H_2O$ (1:1.1), (c) $W_2$ : EMI-DCA + $H_2O$ (1:6.6), (d) D: EMI-DCA + DMSO (1:2.3), (e) $D/W_1$ : EMI-DCA + $H_2O$ + DMSO (1:1.1:2.3) and (f) $D/W_2$ : EMI-DCA + $H_2O$ + DMSO (1:6.6:2.3). (“#” denotes the cycle number.).....	70
Fig. 5-4 SEM SE images of deposits on the substrate surface after cycling for 200 cycles in EMI-DCA based electrolytes: (a) E: EMI-DCA, (b) $W_1$ : EMI-DCA + $H_2O$ (1:1.1), (c) $W_2$ : EMI-DCA + $H_2O$ (1:6.6), (d) D: EMI-DCA + DMSO (1:2.3), (e) $D/W_1$ : EMI-DCA + $H_2O$ + DMSO (1:1.1:2.3) and (f) $D/W_2$ : EMI-DCA + $H_2O$ + DMSO (1:6.6:2.3). Inset images in b, c and f are taken at the same location with a lower accelerating voltage of 0.8 kV; darker regions are ZnO and lighter contrast regions are Zn.....	71
Fig. 5-5 XRD pattern for the deposit after 200 cycles in electrolyte $W_1$ : EMI-DCA + $H_2O$ (1:1.1).....	72

Fig. 5-6 SEM SE images of Zn electrodeposited from EMI-DCA based electrolytes: (a) E: EMI-DCA, (b) W<sub>1</sub>: EMI-DCA + H<sub>2</sub>O (1:1.1), (c) W<sub>2</sub>: EMI-DCA + H<sub>2</sub>O (1:6.6), (d) D: EMI-DCA + DMSO (1:2.3), (e) D/W<sub>1</sub>: EMI-DCA + H<sub>2</sub>O + DMSO (1:1.1:2.3) and (f) D/W<sub>2</sub>: EMI-DCA + H<sub>2</sub>O + DMSO (1:6.6:2.3)..... 73

Fig. 6-1 SEM SE images of Zn electrodeposited on Pt coated Si substrates at a constant potential (-0.15 V vs. Zn wire) from: (a) 9.0 M KOH + 5.0 wt% ZnO, (b) 9.0 M KOH + 5.0 wt% ZnO + 0.1 wt% EMI-TFSI and (c) 9.0 M KOH + 5.0 wt% ZnO + 1.0 wt% EMI-DCA. .... 77

Fig. 6-2 SEM SE images of Zn electrodeposited on Pt coated Si substrates at a constant current density (20 mA/cm<sup>2</sup>) from: (a) 9M KOH + 5 wt% ZnO, (b) 9M KOH + 5 wt% ZnO + 0.01 wt% EMI-DCA, (c) 9M KOH + 5 wt% ZnO + 0.1 wt% EMI-DCA and (d) 9M KOH + 5 wt% ZnO + 1 wt% EMI-DCA. .... 79

Fig. 6-3 Potential vs. time plots (at a current density of 20 mA/cm<sup>2</sup>) during Zn electrodeposition from 9.0 M KOH + 5.0 wt% ZnO electrolytes with the addition of different concentrations EMI-DCA. .... 79

Fig. 6-4 CV plots at 50 mV/s for Zn redox in 9.0 M KOH + 5.0 wt% ZnO electrolytes with the addition of different concentrations EMI-DCA..... 80

Fig. 6-5 SEM SE images of Zn deposited on Pt coated Si substrates from 9.0 M KOH + 5.0 wt% ZnO (left column) and 9.0 M KOH + 5.0 wt% ZnO + 0.5 wt% EMI-DCA (right column) at different current densities: (a) (b) 40 mA/cm<sup>2</sup>, (c) (d) 60 mA/cm<sup>2</sup>, (e) (f) 80 mA/cm<sup>2</sup> and (g) (h) 100 mA/cm<sup>2</sup>. .... 81

Fig. 6-6 Potential vs. time plots (at a current density of 80 mA/cm<sup>2</sup>) during Zn electrodeposition for electrolytes composed of 9.0 M KOH + 5.0 wt% ZnO, without and with 0.5 wt% EMI-DCA. .... 83

Fig. 6-7 Nyquist plots at a deposition current density of 80 mA/cm<sup>2</sup> for electrolytes composed of 9.0 M KOH + 5.0 wt% ZnO, without and with 0.5 wt% EMI-DCA..... 84

## List of Abbreviations

- 1-butyl-3-methylimidazolium hexafluorophosphate (BMI-PF<sub>6</sub>)
- 1-butyl-3-methylimidazolium tetrafluoro-borate (BMI-BF<sub>4</sub>)
- 1-butyl-1-methylpyrrolidinium bis(trifluoromethanesulfonyl)imide (BMP-TFSI)
- 1-butyl-1-methylpyrrolidinium dicyanamide (BMP-DCA)
- 1-ethyl-3-methylimidazolium bis(trifluoromethanesulfonyl)imide (EMI-TFSI)
- 1-ethyl-3-methylimidazolium dicyanamide (EMI-DCA)
- 1-ethyl-3-methylimidazolium ethyl sulfate (EMI-ES)
- 1-ethyl-3-methylimidazolium tetrafluoroborate (EMI-BF<sub>4</sub>)
- 1-methyl-1-pentylpyrrolidinium bis(trifluoromethanesulfonyl)imide (MPP-TFSI)
- 1-methyl-1-propylpyrrolidinium bis(trifluoromethanesulfonyl)imide (MPrP-TFSI)
- Atomic force microscopy (AFM)
- Attenuated total reflectance (ATR)
- Chronoamperometry (CA)
- Conductor-like screening model for real solvents (COSMO-RS)
- Counter electrode (CE)
- Cyclic voltammetry (CV)
- Deionized (DI)
- Density functional theory (DFT)
- Deuterated triglycine sulfate (DTGS)
- Differential scanning calorimetry (DSC)

Dimethyl sulfoxide (DMSO)

Electrochemical deposition (ECD)

Electrochemical impedance spectroscopy (EIS)

Electrochemical window (EW)

Ferrocene/ferrocenium ions (Fc/Fc<sup>+</sup>)

Fourier transform infrared spectroscopy (FTIR)

Electrical energy storage (EES)

Nuclear magnetic resonance (NMR)

Open circuit potential (OCP)

Plug-in hybrid electric vehicle (PHEV)

Polymer electrolytes (PEs)

Polymer electrolyte membrane fuel cells (PEMFC)

Polytetrafluoroethylene (PTFE)

Poly(vinyl chloride) (PVC)

Potassium hydroxide (KOH)

Protic ILs (PILs)

Reference electrode (RE)

Room temperature ionic liquids (RTILs)

Scanning electron microscopy (SEM)

Scanning tunnelling microscopy (STM)

Secondary electron (SE)

Sodium dodecyl benzene sulfonate (SDBS)

Solid electrolyte interface (SEI)

Task specifically functionalized ionic liquids (TSILs)

Tetramethylene sulfone (TMS)

Triethanolamine (TEA)

Tris(4-bromophenyl)amine (TBPA)

Vogel-Fulcher-Tammann (VFT)

Working electrode (WE)

X-ray diffraction (XRD)

Zero-point (ZP)

Zn bis(trifluoromethanesulfonyl)imide (Zn-TFSI)

# Chapter 1 Introduction

## 1.1 Background

Declining oil reserves, in conjunction with new environmental legislation, has driven the development of green energy carriers for road/marine transportation. Such displacement of oil by electrical energy is beneficial for reducing fuel consumption, promoting a low carbon economy and enhancing energy security via geographic diversification of the available energy sources. High efficiency electrical energy storage (EES) devices, with the potential of facilitating large-scale deployment of various renewable electricity generation sources, are a key component in achieving these goals. The search for a suitable energy storage device to electrify road transportation has been the subject of many investigations and has progressed along three main directions, i.e., rechargeable batteries, fuel cells and electrochemical supercapacitors. Of the three EES devices, at the present time, rechargeable batteries are the key power resource, with the other two devices as auxiliary components. Battery technologies, accelerated by the increasing interest in the development and commercialization of battery-powered transportation (e.g., electric vehicles/boats), have improved significantly in the last two decades.

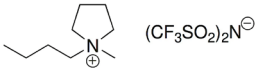
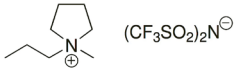
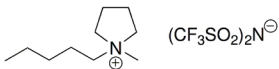
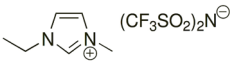
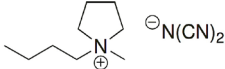
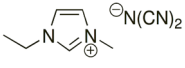
Zinc anode rechargeable batteries, characterized by low cost, abundant supply and widespread availability of Zn raw materials and environmentally benign nature, are vital energy storage devices to electrify road/marine transportation, as well as stationary utilities. Nevertheless, a conventional Zn anode rechargeable battery using an alkaline aqueous electrolyte suffers from an inherent drawback of limited cycle life (the number of possible charge–discharge cycles accomplished just before failure takes place). Its short lifetime is partly due to the drying out of the aqueous electrolyte. Furthermore, failure of the Zn electrode also accounts for the short lifetime. During cycling, Zn dendritic growth induced shorting circuiting is a general problem for Zn anode batteries, which restricts rechargeability. During the past half-century, the most common ways to minimize these problems have been to incorporate additives in the electrode or electrolyte. Nevertheless, the current methods cannot completely eliminate the problems, particularly dendrite formation. Alternative methods are still needed to achieve a breakthrough for improving cycle life performance for Zn anode rechargeable batteries. Replacement or

modification of traditional aqueous electrolytes with novel electrolyte systems appears to be a promising way to bridge the current research gap.

Room temperature ionic liquids (RTILs, i.e., salts that melt at or below room temperature), with their desirable properties of low or no volatility, low melting temperature, high thermal stability, low flammability and wide electrochemical window (EW), have received growing interest in recent years for application as advanced and safe electrolytes/electrolyte components for rechargeable batteries. Zinc anode rechargeable batteries using RTILs as their electrolytes have the potential to function significantly longer because failure due to water evaporation is no longer a problem. In addition, RTILs exhibit the capacity to modify metal deposit morphology [1], which may contribute greatly to improving battery lifetime. It is thus proposed in this work to adopt RTILs to replace or modify conventional alkaline aqueous electrolyte for Zn anode rechargeable batteries. Information regarding the ion-based properties serves as a powerful guide for the selection of RTILs in battery applications. In terms of the cations, RTILs with imidazolium cations have low viscosity, which contributes to improved ionic conductivities at room temperature, and have been commonly mixed with polymer electrolytes for state-of-art Li-based batteries [2]. RTILs with pyrrolidinium cations have competitive features such as low melting temperature, high cathodic stability and excellent ability for modifying deposit morphology [3]. For anions with high resistance to moisture absorption and low solubility for water, RTILs with bis(trifluoromethanesulfonyl)imide anions have attracted significant interest for both electrochemical deposition (ECD) [4] and Li-based batteries [5]. In addition, RTILs with dicyanamide anions have been exploited for ECD due to their low viscosity [6] and ability to improve deposit morphology [7]. Therefore, in this thesis, six different ionic liquids (with pyrrolidinium or imidazolium cations and bis(trifluoromethanesulfonyl)imide or dicyanamide anions), i.e., 1-butyl-1-methylpyrrolidinium bis(trifluoromethanesulfonyl)imide (BMP-TFSI), 1-methyl-1-propylpyrrolidinium bis(trifluoromethanesulfonyl)imide (MPrP-TFSI), 1-methyl-1-pentylpyrrolidinium bis(trifluoromethanesulfonyl)imide (MPP-TFSI), 1-ethyl-3-methylimidazolium bis(trifluoromethanesulfonyl)imide (EMI-TFSI), 1-butyl-1-methylpyrrolidinium dicyanamide (BMP-DCA) and 1-ethyl-3-methylimidazolium dicyanamide (EMI-DCA) are investigated as potential electrolytes for Zn anode rechargeable batteries.

The structures of the studied RTILs, together with their physicochemical properties, are presented in Table 1-1. It is clear from Table 1-1 that all the studied RTILs suffer a critical shortcoming, i.e., relatively low conductivity (1.3-25 mS/cm vs. 540 mS/cm for a 29.4 wt% KOH aqueous solution [8]), which could severely restrict their use in energy storage applications. Henceforth, for electrolytes based on RTILs, water and dimethyl sulfoxide (DMSO) are selected as diluents to improve the conductivity of RTILs before their merits can be fully utilized. Electrolytes composed of a traditional alkaline aqueous solution with RTILs as additives are also investigated, with the purpose of adopting the benefits of modifying Zn deposit morphology from RTILs. To sum up, two kinds of electrolyte systems are explored in this thesis for potential application in Zn anode rechargeable batteries, with RTILs act as either the main components (with the incorporation of diluents) or supporting additives to alkaline aqueous electrolytes.

Table 1-1 Structure and physicochemical properties of the studied RTILs

Electrolyte	Structure	Melting temperature (°C)	Electrochemical window (V)	Conductivity (mS/cm)
BMP-TFSI		-18.1	5.7	3.4
MPrP-TFSI		+10.0	5.7	3.9
MPP-TFSI		+9.0	5.5	1.3
EMI-TFSI		-13.5	4.7	8.6
BMP-DCA		-21.1	3.2	9.8
EMI-DCA		-21.0	3.3	25

## 1.2 Structure of thesis

A brief introduction, which provides research background and relevant subject matter, is outlined in this section. This includes the order of the chapters to be presented, as well as associated journal and conference papers derived from this work.

Chapter 2 first reviews the advantages and limitations associated with the development of Zn anode rechargeable batteries. RTILs are then introduced as promising electrolytes, with applications focused on batteries and electrodeposition. The need and potential of applying RTILs as electrolyte components for Zn anode rechargeable batteries is further discussed.

Chapter 3 presents preliminary results regarding Zn redox behavior in four RTILs, i.e., BMP-TFSI, MPP-TFSI, EMI-TFSI and BMP-DCA, and establishes an understanding on the dependence of Zn redox reversibility, kinetic properties, reaction mechanisms and cyclability on the types of cations and anions of RTILs. The outcome further sheds light on the screening of desirable RTILs candidates for Zn anode rechargeable batteries.

- M. Xu, D.G. Ivey, Z. Xie, W. Qu, Electrochemical behavior of Zn/Zn(II) couples in aprotic ionic liquids based on pyrrolidinium and imidazolium cations and bis(trifluoromethanesulfonyl)imide and dicyanamide anions, *Electrochimica Acta* 89 (2013) 756-762.
- M. Xu, D.G. Ivey, W. Qu, Z. Xie, Y. H. Bing, Cyclic voltammetry of Zn/Zn(II) couple in dicyanamide anion and bis(trifluoromethanesulfonyl)imide anion based ionic liquids, *ECS Transactions*, 50 (25) 13-22 (2013).

Chapter 4 discusses the study on electrolytes composed of RTILs with water as a diluent. Emphasis is given to hydrophobic RTILs with bis(trifluoromethanesulfonyl)imide anions. The interaction of water with the ions of these RTILs, as well as the effect of water on the electrolyte conductivity, Zn redox kinetics and Zn deposit morphology, are investigated. The mechanisms associated with the effect of water are also elucidated.

- M. Xu, D.G. Ivey, Z. Xie, W. Qu, E. Dy, The state of water in 1-butyl-1-methylpyrrolidinium bis(trifluoromethanesulfonyl)imide and its effect on Zn/Zn(II) redox behavior, *Electrochimica Acta*, 97 (2013) 289-295.
- M. Xu, D.G. Ivey, W. Qu, Z. Xie, E. Dy, X. Z. Yuan, Zn/Zn(II) redox kinetics and Zn deposit morphology in water added ionic liquids with bis(trifluoromethanesulfonyl)imide anions, *Journal of The Electrochemical Society*, 161 (1) A128-A136 (2014).

- M. Xu, D.G. Ivey, W. Qu, Z. Xie, X. Z. Yuan, The effect of water addition on Zn/Zn(II) redox reactions in room temperature ionic liquids with bis(trifluoromethanesulfonyl)imide anions, *ECS Transactions*, 53 (36) 41-50 (2013).

Chapter 5 continues the investigation of electrolytes composed of RTILs with the addition of diluents, with the focus adjusted to a hydrophilic RTIL with a dicyanamide anion, i.e., EMI-DCA, since it has superior conductivity to its hydrophobic counterparts studied in Chapter 4. The addition of both water and DMSO diluents is found to exert a synergistic effect for improving Zn redox kinetics, reversibility and cyclability in EMI-DCA.

- M. Xu, D.G. Ivey, W. Qu, Z. Xie, Improved Zn/Zn(II) redox kinetics, reversibility and cyclability in 1-ethyl-3-methylimidazolium dicyanamide with water and dimethyl sulfoxide added, *Journal of Power Sources*, 252 (2014) 327-332.

Chapter 6 explores a novel electrolyte system composed of RTILs as additives to conventional alkaline electrolytes. With the capability of modifying metal deposit morphology, RTILs are found to be effective in inhibiting Zn dendrite formation in KOH aqueous electrolytes.

- M. Xu, D.G. Ivey, W. Qu, Z. Xie, E. Dy, Exploration of electrolytes for Zn-anode rechargeable batteries: room temperature ionic liquids as major or supporting components, in: *Ionic liquids: synthesis, characterization and applications*, A. Brooks (Eds.), Nova Science Publishers, Inc., 2014, pp. 99-123.

Chapter 7 presents final conclusions based on the results of this thesis. Recommendations for future work are also given, with the purpose of sharing ideas on modifying electrolytes for application in Zn anode rechargeable batteries.

## Chapter 2 Literature review

In this chapter, the benefits of deploying Zn anode rechargeable batteries as power sources for both mobile and stationary energy storage applications are presented. Zinc-air batteries, characterized by extraordinarily high specific energy and specific power, are discussed as a representative in particular. Typical problems that hinder the commercial application of Zn anode rechargeable batteries are then addressed, followed by the introduction of RTILs electrolyte as promising alternatives or supplements to tackle these problems.

### 2.1 Zn anode rechargeable batteries: Advantages and limitations

Since 1859, following the invention of lead acid batteries, i.e., the first rechargeable batteries, by Gaston Planté, a diversity of rechargeable battery technologies have emerged for the increasing need to power automotive and domestic utilities. Among them, Zn anode rechargeable batteries are attractive and desirable systems, with their applications covering a broad spectrum, i.e., ranging from hybrid/electric vehicles to utility/custom-side load-levelling and new portable devices.

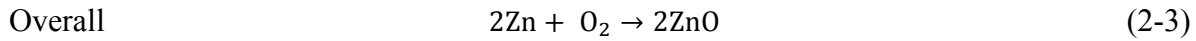
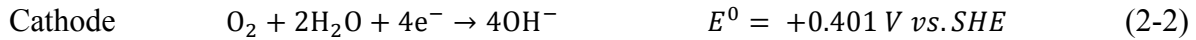
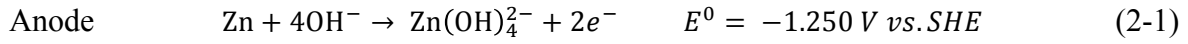
#### 2.1.1 Typical Zn anode rechargeable batteries and their advantages

In the past three to four decades, there has been significant advancement in Zn anode batteries along with the recognition of their good performance, such as high specific energy and specific power. Well-established systems involve Zn-Ni batteries, Zn-bromine batteries, Zn-polymer batteries, Zn-MnO<sub>2</sub> batteries and Zn-air batteries. The typical electrochemical performance of these batteries is summarized and compared with selected Li-based batteries in Table 2-1.

Table 2-1 Comparison of specific energy/power for Zn anode batteries and Li-based batteries

Battery system	Theoretical specific energy (Wh/kg)	Achieved specific energy (Wh/kg)	Achieved specific power (W/kg)
Zn-Ni	340 [9]	55-85 [10]	140-200 [10]
Zn-bromine	440 [11]	65-75 [12]	90-110 [12]
Zn-Polymer	NA	150-170 [13, 14]	NA
Zn-MnO <sub>2</sub>	290 [15]	77 [15]	NA
Zn-air	1300 [16]	100-300 [17]	80-105 [17, 18]
Li-ion	631 [19]	100-150 [20]	80-300 [21]
Li-air	13300 [16]	800-2500 [21]	200-600 [21]

Of these Zn anode batteries, Zn-air batteries are the most attractive ones due to their superior specific energy, which is comparable to Li-based batteries. The high specific energy of Zn-air batteries is mainly because that one of its electroactive materials, i.e., oxygen, does not require storage. The anode, cathode and overall reactions for a Zn-air battery using an alkaline aqueous electrolyte during discharge are summarized as follows [22, 23]:



Generally, Zn-air rechargeable batteries are classified into electrically rechargeable Zn-air batteries and mechanically rechargeable Zn-air batteries. Electrically rechargeable Zn-air batteries can be considered as a battery-fuel cell hybrid system, since one of the reactants, oxygen, is from the atmosphere and is outside the battery system. In order to accomplish electrical recharge, either an additional electrode is needed for oxygen evolution during charging or a bifunctional air electrode is required to achieve both oxygen reduction and evolution. The design and fabrication of a workable bifunctional air electrode with desirable performance remains a major technical obstacle. Mechanically rechargeable Zn-air batteries can be directly treated as fuel cells. In addition to oxygen being supplied from the surroundings, the Zn reactant or Zn anode in mechanically rechargeable systems also needs to be replenished or replaced from an external source.

When it comes to evaluating a battery technology as a power source for either automotive or stationary utility applications, several critical factors other than electrochemical performance must be considered; these include cost, safety and material availability, which are discussed in the following paragraphs. Based on these criteria, Zn anode rechargeable batteries exhibit great potential for being the backbone technology in the future, even compared with state-of-art Li-based batteries that have excellent electrochemical performance.

(1) Cost is always the most fundamental issue that restricts the application and commercialization of battery products. Zinc anode rechargeable batteries are cost effective

systems (e.g., \$35-50/kWh for Zn-air batteries [24]). Li-ion batteries are considered as the best current technology to propel electric drive vehicles, but are very expensive with a cost in the range of \$750-1000/kWh in 2008. Even with plug-in hybrid electric vehicle (PHEV) programs PHEV-10 and PHEV-40, where costs are expected to decline due to the use of smaller batteries, optimistic estimated costs for using Li-ion batteries are not much below \$300/kWh by the end of 2020 [25]. Thus, mass production of Li-ion batteries is not viable for modern electric drive vehicles.

(2) Safety is another important issue when adopting rechargeable batteries for either industry or domestic applications. Safety problems, such as electrolyte fires, possible thermal runaway and even explosion due to the reactivity of the materials involved [26] are crucial troubles rooted in the application of Li-based batteries. Zinc-based rechargeable batteries, on the other hand, are considered a safe technology.

(3) Widespread availability and accessibility of Zn raw materials throughout the world is another advantage of Zn anode rechargeable batteries, so that long-term application for the mass market is guaranteed. Metal production of Zn is sufficient due to its abundant presence in the Earth's crust, i.e., ranked the fourth in the world, just after Fe, Cu and Al. Specifically in Canada, there are several world-class Zn mining companies, such as Teck Metal Ltd. and Xstrata Zinc. According to a report by Tahil in 2007 [27], however, there is insufficient Li supply and future production of Li cannot meet the needs of the global automotive market. Additionally, the geographic availability limitation of Li (only abundant in the Andes and Tibet) constrains its further development.

### **2.1.2 Limitations for commercializing Zn anode rechargeable batteries**

Even though Zn anode rechargeable batteries are promising power sources and energy storage devices, practical application is critically restricted by their limited cycle life. Four main problems, including dendritic growth, shape change, passivation and self-discharge, that lead to the Zn anode failure are considered to be responsible for the poor cycle life performance. In the following paragraphs, approaches that have been attempted to solve these problems are discussed. The research gaps regarding improvement of the cycle life for alkaline Zn anode rechargeable batteries are then listed and summarized.

### 2.1.2.1 Dendrite formation

Zinc dendritic deposits that form during charging in alkaline aqueous electrolytes severely decrease the cycle life of Zn anode rechargeable batteries. It is the uneven deposition of Zn at active sites, where discharged Zn species gather, that results in the formation of Zn dendrites. Dendrites can grow and then penetrate the separator, reach the counter electrode and cause eventual short circuiting [28]. There has been considerable effort to retard and suppress Zn dendrite formation and propagation. The key idea is to promote uniform deposition of Zn on charging and inhibit successive dendrite growth.

Among the established approaches, incorporation of additives in either the electrode or the electrolyte is one way to modify Zn deposit morphology. Lee and his colleagues [29] improved the electrochemical behavior of the Zn anode for a Zn-air battery by applying a small amount of Ni and In as electrode additives. They suggested that the use of a Zn-Ni-In alloy anode can prevent Zn dendrite formation as well as improve the reversibility of the anode. In addition to direct addition to the Zn electrode, wrapping the Zn electrode with a thin film has also proven to be a feasible way to impede dendrite formation. Zhu and Zhou [30] studied the coating of La and Nd hydroxides on the surface of Zn electrodes. By decreasing the amount of dissolved Zn discharged species (Zn oxide and zincate ions) in the electrolyte, these coatings can promote a smoother Zn deposit surface. Zhu and Zhou further investigated an alternative organic ionomer as the coating material and found similar improvement to Zn deposit morphology [31]. The fabricated Zn-ionomer electrode can significantly lower the solubility of Zn discharge products in the electrolyte which, in turn, inhibits Zn dendrite growth. One drawback of additives in the Zn electrode is the increased total weight of the electrode, which is unfavorable for specific energy.

Compared with electrode additives, incorporation of additives into the electrolyte is a more common way to prevent Zn dendritic growth. The main focus of this approach is to screen desirable Zn deposit morphology modifiers, either inorganic or organic candidates. Lead has long been considered as a favorable electrolyte additive for improving Zn deposit morphology. It acts as a dendrite inhibitor that suppresses the initiation and propagation of Zn dendrites by specifically adsorbing on dendrite sites [32, 33]. Mixing the alkaline potassium hydroxide electrolyte, which is commonly used in Zn anode rechargeable batteries, with certain amounts of

potassium fluoride, phosphate or borate salts, leads to low solubility for the Zn discharge species (Zn oxide) and thus suppresses dendrite growth. However, a mixed electrolyte can have deleterious effects on cell resistance and electrode utilization, leading to a reduction in energy or power density [34]. The effectiveness of Bi ions, as a Zn deposit-enhancing additive in the electrolyte, was presented by Wang et al. [35]. They attributed the function of Bi ions to a so-called substrate effect, i.e., with a more positive electrode potential than Zn, Bi ions can be reduced prior to Zn deposition, forming a conductive Bi matrix to promote more uniform Zn distribution and active Zn deposits with improved Zn morphology [36]. A similar mechanism was also claimed for Sn ion additions as an electrolyte additive to prevent Zn dendrite formation [37]. As seen in Fig. 2-1, classic Zn dendrites with side branches were observed in the electrolyte with no additives. In electrolyte containing Sn ions, Zn deposit morphology was modified to some extent, i.e., Zn dendrites were converted to compact cylinders with rounded tops, which can mitigate their penetration to the separator.

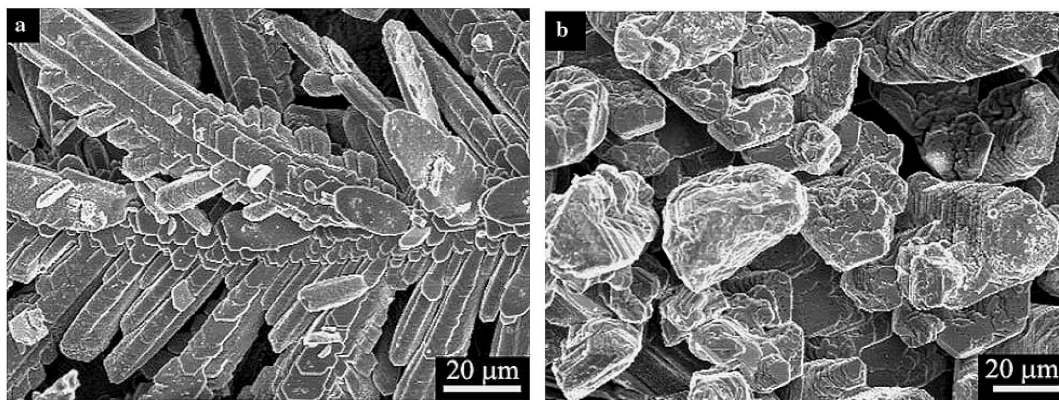


Fig. 2-1 Electrodeposit morphology on the surface of a Zn electrode from (a) an electrolyte with no additives and (b) an electrolyte containing 0.12 g/L  $\text{Sn}^{2+}$  [37].

There is a trend to applying organic additives in traditional alkaline electrolytes as dendrite inhibitors for Zn anode rechargeable batteries. Of these organic additives, ammonia-derived organic compounds have attracted the most attention. Wilcox and Mitchell [38] examined quaternary ammonium compounds as Zn electrodeposit enhancers. Quaternary ammonium in low concentrations, with a large cationic group, was favorable for the reduction of dendritic growth. More recently, Lan et al. [39] performed a comprehensive investigation of tetra-alkyl-ammonium hydroxides as electrolyte additives on controlling the deposit morphology of Zn

anodes. A blocking effect, due to physical adsorption of non-polar alkyl groups on the Zn electrode surface, was proposed as the mechanism for dendrite inhibition. These alkyl groups can specifically attach and cover the active sites where Zn dendrites grow much faster and thus work as dendrite resistors. It is noted that moderate polarity is required for uniform coverage of alkyl groups and dendrite prevention; therefore, the chain length, i.e., the type of alkyl group, should be properly selected. Additionally, an impressive feature of tetra-alkyl-ammonium hydroxide additives is that no drop in ionic conductivity of the mixed electrolyte was observed. A slight increase was found instead, which may be due to the ionic conductive contribution from extra free hydroxide ions or the alkyl ammonium cations.

An improvement in the cycle life, restricted by the Zn dendrite problem, also relies on the performance of the separator systems in Zn anode rechargeable batteries. Cellulose has been the conventional separator material employed in battery systems. However, due to its poor durability caused by oxidation, many other organic materials have been studied as alternatives [24]. Of these candidates, poly(vinyl alcohol) (PVA) is the most common separator material. Sato et al. [40] proposed that PVA films containing  $H_3BO_3$  acid coated on a thin nylon non-woven cloth was as an excellent separator for Zn dendrite suppression in Zn-Ni rechargeable batteries, since it can efficiently inhibit zincate ion penetration while preserving a high ionic conductivity. A microporous separator may be a favorable choice for Zn anode batteries, since it possesses a unique mass transfer property contributing to Zn dendrite minimization [41]. Yang et al. [42] synthesized a microporous PVA and poly(vinyl chloride) (PVC) composite polymer separator with an optimal pore size (60-120 nm) and this separator was shown to be beneficial in preventing Zn dendrite formation during charging. Generally speaking, to be a competent separator in alkaline Zn anode rechargeable batteries, the separator must maintain a high ionic conductivity while allowing low zincate ion penetration from the anode to the cathode. The separator also needs to be stable in an alkaline electrolyte, resistant to oxidation and have good wettability.

#### 2.1.2.2 Shape change

Shape change, associated with the redistribution of active materials over the Zn electrode surface on cycling, is caused by preferential dissolution of solid Zn from the electrode edges during discharging, followed by concentrated redeposition at the electrode center with a more compact

form during charging [24, 43]. This problem results in an eventual decrease in the effective surface area and limited cycle life for alkaline Zn anode rechargeable batteries.

Similar to the ways for solving dendrite formation, methods developed to alleviate shape change for the Zn anode also focus on three main directions, i.e., electrode additives, electrolyte additives and suitable choice of separator, devoted to lowering the solubility of Zn discharged species in the electrolyte.

First of all, applying electrode additives is a common way to limit shape change. The function of these additives is fulfilled either by restricting the migration of Zn species from the vicinity of the Zn anode during discharge or through enhancement of the current distribution during charging. The heavily adopted electrode additives are metal hydroxides or oxides. An early study reported that Zn anodes made with  $\text{Ca(OH)}_2$  and  $\text{Bi}_2\text{O}_3$  were beneficial for inhibiting shape change during cycling [40]. The mechanism for  $\text{Ca(OH)}_2$  to depress shape change is generally attributed to the formation of insoluble Ca zincate, which minimizes the solubility of discharged zincate ions in the electrolyte and prevents the occurrence of subsequent shape change. Adding  $\text{Ca(OH)}_2$  at an optimized concentration to the Zn anode not only retards Zn redistribution by lowering Zn species solubility, but also significantly improves the Zn active material utilization [44, 45]. The effect of Ca zincate on suppressing Zn anode shape change is also dependent on the concentration of the KOH electrolyte. With decreased KOH concentration, the presence of  $\text{Ca(OH)}_2$  further decreases the solubility of the Zn species and increases cell cycle life [46, 47]. However, from the point of view of reducing self-discharge and passivation, insufficient KOH concentration may have an undesirable impact. Bi oxide is also regarded as a favorable electrode additive for shape change inhibition. Its contribution to prolonged cycle life of Zn anodes is also due to the so-called substrate effect mentioned in the last section. Additionally, shape change, which is related to non-uniform current distribution, can be minimized by adding  $\text{PbO}$ ,  $\text{In(OH)}_3$  and  $\text{Tl}_2\text{O}_3$  to the Zn electrode, since these metal oxides/hydroxides have the ability to increase anode polarizability and thus improve the current distribution [48, 49]. Furthermore, organic additives to Zn electrodes have also been studied for suppressing shape change. Among them, polytetrafluoroethylene (PTFE) dispersion is widely used in Zn electrodes as a binder, with merits of retaining Zn active materials, slowing shape change and improving mechanical properties due to its three dimensional structure [40]. Sharma et al. [50] investigated the effect of

another organic additive, triethanolamine (TEA), on the cycle life performance of Zn anodes. Their results displayed that the chelating agent TEA and zincate ions form a weak complex, which decreases the solubility of zincate ions and reduces the tendency for shape change.

Secondly, additives can be incorporated into the electrolyte to directly reduce the solubility of discharged Zn species in the modified electrolyte. One risk of taking this approach, however, is that it may lead to an increase in cell resistance with a corresponding decline in energy density. Adler et al. [51] prepared Zn-Ni rechargeable battery electrolytes by adding a supporting electrolyte of KF and  $K_2CO_3$  to a KOH solution. This modified electrolyte, with decreased KOH contribution, had a lower solubility for discharged zincate ions than the traditional pure KOH electrolyte. The rate of Zn active material redistribution was thus found to decline dramatically, along with an improvement in cycle life performance.

Thirdly, separators with rapid mass transfer characteristics can retard shape change by lessening the ion concentration gradient that exists in a cell system. From this perspective, microporous separators are superior to membrane separators due to their better performance regarding mass transfer [41]. Generally, a proper separator design can minimize shape change and dendrite formation simultaneously. For instance, the microporous PVA and PVC composite polymer separators mentioned previously [42] have the function of reducing both dendrite growth and shape change with an optimized pore structure.

#### 2.1.2.3 Passivation

Zinc anodes undergo passivation during discharge in parallel with the precipitation of ZnO, giving rise to the formation of a passivation layer on the surface of the electrodes. This problem is ascribed to the limited mass transfer of the soluble species ( $OH^-$  and  $Zn(OH)_4^{2-}$ ) to/from the dissolving Zn anode [52]. Decreased Zn electrode utilization (which depends on the capability of the electrode to remain active during discharge) and capacity loss are the undesirable consequences of passivation. Three different kinds of passivation processes for the porous Zn electrode were proposed by Sunu and Bennion [43], namely electrolyte depletion, pore plugging and physical passivation. Table 2-2 summarizes the three sub-mechanisms of passivation and suggested resolutions from their work.

Table 2-2 Passivation sub-mechanisms for a porous Zn anode (summarized according to [43])

Sub-mechanism	Cause	Effect	Possible solutions
Electrolyte depletion	Insufficient supply of reservoir solution (RS <sup>a</sup> ) and pore solution (PS <sup>b</sup> ) due to the limited mass transfer of OH <sup>-</sup> across the separator from the solution on the counter electrode side	Passivation occurs at the active Zn surface due to decreased ZnO solubility and increased rate of ZnO precipitation	I. Plentiful supply of RS II. Suitable selection of a separator
	Pore plugging	RS is sufficient, but PS is depleted due to the limited mass transfer of OH <sup>-</sup> across the reaction zone with smaller pores	Passivation occurs at the discharging Zn surface with depleted electrolyte
Physical passivation	RS and PS are both sufficient, but the Zn electrode surface has superfluous Zn(OH) <sub>4</sub> <sup>2-</sup> or depleted OH <sup>-</sup>	Passivation occurs due to the physical blocking of a precipitated ZnO film covered on the active Zn surface	I. Increase the active surface area of Zn electrode II. Enhance uniform current distribution

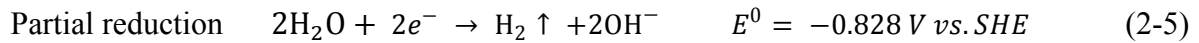
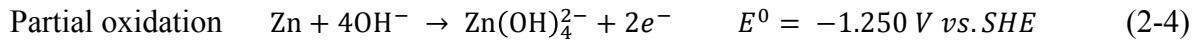
<sup>a</sup> Solution within the compartment on the Zn electrode side; <sup>b</sup> solution inside the porous electrode.

Incorporation of additives into the Zn electrode or electrolyte is a common way to inhibit different kinds of passivation. To avoid pore plugging/densification of the Zn anode used for a Zn-air secondary battery, Müller et al. [53] chose cellulose as the electrode additive because of its excellent hydrophilic and chemical stable properties. It has been shown that 10 wt% of cellulose can effectively optimize and retain the porous structure as well as the wettability of Zn anodes after cycling, serving as an internal channel for electrolyte transportation. The reported cycle life of the modified Zn anode was 5-10 times higher than that without cellulose addition. Furthermore, through addition of sodium dodecyl benzene sulfonate (SDBS) as a surfactant to the dilute KOH electrolyte, the passive film on the Zn anode surface was changed from dense and compact to a loose and porous structure due to the adsorption of SDBS. This modified morphology facilitated the diffusion of hydroxide ions from the electrolyte to the Zn electrode

surface and inhibited the accumulation of zincate ions on the surface, efficiently suppressing the passivation of the Zn anode [54].

#### 2.1.2.4 Self-discharge

For an alkaline Zn anode rechargeable battery, self-discharge refers to Zn corrosion along with hydrogen evolution during the charging period. In aqueous KOH alkaline electrolytes, the reactions during Zn electrode corrosion and hydrogen evolution can be expressed according to mixed-potential theory [55]:



These self-discharge processes have detrimental effects, not only on the cycle life of Zn anode batteries, but also on the ampere-hour output (capacity) due to the corrosion of active Zn materials. Several studies, therefore, have been undertaken to reduce the corrosion reactions invoked by hydrogen evolution. The methods employed include mainly the adoption of additives in the electrode/electrolyte and the use of proper separators.

Early attempts at restricting Zn corrosion with electrode/electrolyte additives were based on the principle of choosing metallic additives with high hydrogen overpotentials. Heavy metal additions, e.g., Hg and Pb (1.0-5.0 wt%), in either oxide or hydroxide form were confirmed to be good corrosion inhibitors [56]. However, the adverse impact of amalgamation on the cycling performance and cell capacity [57] hindered the application of Hg in Zn anode batteries. The inhibiting mechanism of Pb oxides in the Zn anode was suggested to be a physical barrier effect, i.e., the presence of Pb at active sites on the Zn surface restricted the transportation of Zn species from the electrode [58]. One drawback of Pb oxides, revealed by Shivkumar et al. [59, 60], was that the deposition of Pb during charging can either decrease the open circuit potential (OCP) or poison the counter electrode, both of which were unfavorable for battery performance. The authors also investigated the effect of other metal oxides on hydrogen evolution control, e.g., V<sub>2</sub>O<sub>3</sub> and ZnO as electrolyte additives and Sb<sub>2</sub>O<sub>3</sub> and TiO<sub>2</sub> as Zn electrode additives. Based on their results, ZnO was the most desirable additive since it can be safely used; it greatly reduces corrosion reaction and increases the cycle life. This also accounts for the prevailing application of ZnO in alkaline electrolytes for research studies of Zn anode batteries. One possible

explanation for the beneficial effect of ZnO can be found in the early study from Dirkse and Timmer [61]. They suggested that the dissolution of ZnO in an alkaline electrolyte leads to the formation of zincate ions ( $\text{ZnO} + \text{H}_2\text{O} + 2\text{OH}^- \rightarrow \text{Zn}(\text{OH})_4^{2-}$ ), which in turn can lower the activity of the water and decrease the hydrogen evolution reaction. The realization of decreasing self-discharge of the Zn anode can also be achieved by employing desirable separators. One result of particular interest from Dewi's group [62] shows that a novel cationic polysulfonium membrane, characterized by high ionic selectivity, can effectively prevent the self-discharge process caused by the permeation of Zn cations between the anode and the cathode. This membrane, composed of anion permselective materials, possessed high ionic conductivity for hydroxide anions, while thoroughly suppressing the penetration of Zn cations in the alkaline electrolyte. With this advantage, a cationic polysulfonium membrane is a promising separator that can be commercialized in Zn-air batteries as a replacement for traditional polypropylene membranes.

### 2.1.3 Summary

This section demonstrated the potential and advantages of applying Zn anode rechargeable batteries as energy storage devices to electrify automotive as well as stationary utilities. Significant emphasis was put on categorizing and assessing four common problems, i.e., dendritic growth, shape change, passivation and self-discharge, those restrict the cycle life of Zn anode rechargeable batteries. It should be noted that although each problem was discussed separately, none of them is isolated from one another; instead they are interconnected and co-exist during cycling. Therefore, approaches that are aimed to minimize one problem will also exert an influence on the others.

On the one hand, any of the proposed methods can be beneficial for suppressing different problems concurrently. Methods that can reduce the solubility of zincate ions can, in theory, restrict dendrite formation and shape change at the same time. For example, using electrolyte additives and electrode additives, such as  $\text{Ca}(\text{OH})_2$  and  $\text{Bi}_2\text{O}_3$  [36, 40], is useful for both dendrite and shape change inhibition. The addition of TEA to the Zn electrode was reported not only to decrease shape change, but also helped in resolving the passivation problem for Zn- $\text{MnO}_2$  batteries [50]. The incorporation of ferricyanide complex anions into the KOH electrolyte has shown promise for the suppression of both passivation and self-discharge [63]. For dendritic

growth and self-discharge, that take place simultaneously during charging, applying various ionic types of perfluorosurfactants can restrict both problems [64]. In addition, the combination of a microporous separator and a multi-layer separator can solve mixing problems, with the former reducing shape change and passivation, and the latter limiting dendrite propagation [65]. On the other hand, one solution to a problem may lead to the occurrence of the other problems. A typical example is regarding dendrite/shape change vs. passivation. As discussed above, using a large electrolyte reservoir with sufficient  $\text{OH}^-$  supply is good for preventing passivation [43]. However, this may also promote the solubility of zincate ions in the electrolyte and cause dendrite formation and shape change. In addition, when adding a zincate solubility-reducing agent to the electrolyte/electrode to depress dendritic growth and shape change, attention must be paid to control the additive concentration so as to avoid induced passivation [66, 67]. In other words, a suitable choice of additives with a proper passivation effect is required to obtain desirable battery performance between balanced cycle life and capacity (materials utilization).

As stressed before, the high solubility of Zn discharged products (zincate) in alkaline electrolytes gives rise to two major problems, dendrite formation and shape change, which are primarily responsible for the short cycle life of Zn anode rechargeable batteries. Significant work has been done to reduce zincate solubility in aqueous electrolytes, focusing on using proper electrolyte/electrode additives. However, these methods cannot completely eliminate the problems and may even bring about other adverse effects such as decreased electrolyte conductivity and reduced energy density. Therefore, alternative methods are still needed to achieve a breakthrough for improving cycle life performance. Replacement or modification of traditional aqueous electrolytes with novel electrolyte systems appears to be a key way to bridge the current research gap. RTILs (which will be addressed in the next section), with their excellent properties of low or no volatility, low flammability and wide electrochemical window, have received growing interest for application as advanced and safe electrolytes for rechargeable batteries.

## **2.2 Room temperature ionic liquids (RTILs) and their applications**

Nonaqueous ionic liquids (ILs), composed exclusively of ions (cations and anions), are salts with low melting temperatures around 100°C or below as an arbitrary temperature limit [68]. Specifically, ionic liquids that melt at or below room temperature are called RTILs. It is of interest in this work to consider the role of RTILs as electrolytes employed in battery systems. Comparison of RTILs with conventional aqueous electrolytes can clearly show the benefits of applying novel RTILs in batteries, as well as the advances in this research area. First of all, RTILs are nonaqueous, which is one of the major differences compared with aqueous electrolytes. The volatility disadvantage rooted in aqueous electrolytes is not a problem for RTILs, making them a safer alternative in batteries. Currently, RTILs have been broadly adopted as electrolytes in Li-ion batteries so as to alleviate their safety issues [69]. Secondly, being completely ionic is another special feature that distinguishes RTILs from aqueous electrolytes. Aqueous electrolytes originate from the dissolution of salts in a water solvent and consist of solvated ions, their charged or neutral combinations and solvent molecules. On the other hand, RTILs are salts melted (liquified) by providing heat to the system to overcome the salt lattice energy and are only composed of ions and their combinations, without any molecular solvent [70]. This ionic nature guarantees a wide electrochemical window for using RTILs in batteries, in conjunction with high electrode efficiency.

### **2.2.1 Structure and physicochemical properties of RTILs**

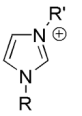
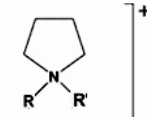
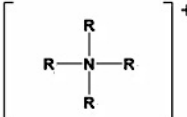
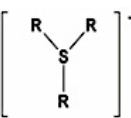
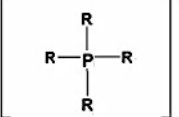
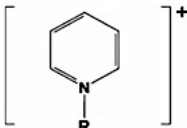
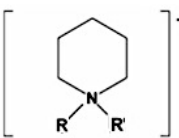
More than 200 RTILs had been reported by 2005 [68]. Different choices and combinations of cations and anions give rise to the diversity of RTILs. Consequently, a unique merit of RTILs is their tunable characteristic [71], making them favorable solvents and reaction media in many research disciplines. The nature of the ions determines the physical and chemical properties of RTILs.

#### **2.2.1.1 Structural features of RTILs**

RTILs are generally composed of large organic cations and organic/inorganic anions. On the basis of either cations or anions, RTILs can possess various structures. From the point of view of cations (Table 2-3), the most common ones include imidazolium (typically 1-butyl-3-methyl- or 1-ethyl-3-methyl-imidazolium), pyrrolidinium, ammonium, sulfonium, phosphonium, pyridinium and piperidinium.

Based on the anions, RTILs are usually divided into two groups (Table 2-4): the first is those with inorganic elements such as dicyanamides, halides and fluorine-based ions; the second is organic anions, such as bis(trifluoromethanesulfonyl)imide, 2,2,2-trifluoro-N-(trifluoromethanesulfonyl)acetamide and alkylsulfates. The RTILs chosen in Tables 2-3 and 2-4 are just representatives that have been prevalently studied. More detailed information about the types of ILs as well as RTILs can be found in review papers [68, 70] and comprehensive structure information for ILs is well summarized in reference [72].

Table 2-3 Typical cations for RTILs

Type of cations	Structure [68, 70]	Abbreviation
Imidazolium		$[RR'Im]^+$
Pyrrolidinium		$[RR'P]^+$
Ammonium		$[R_4N]^+$
Sulfonium		$[R_3S]^+$
Phosphonium		$[R_4P]^+$
Pyridinium		$[RPi]^+$
Piperidinium		$[RR'Pp]^+$

Note: R and R' denote different alkyl groups.

Table 2-4 Typical anions for RTILs

	Type of anions	Examples and structures [68, 70]	Symbol
Inorganic	Dicyanamide	$[\text{N}(\text{CN})_2]^-$	DCA <sup>-</sup>
	Halide	$[\text{Cl}]^-$	NA
	Fluorinated	$[\text{BF}_4]^-$ , $[\text{PF}_6]^-$ , $[\text{SbF}_6]^-$ , $[\text{HF}]_{2,3}\text{F}^-$	NA
Organic	Bis(trifluoromethanesulfonyl)imide	$[\text{N}(\text{CF}_3\text{SO}_2)_2]^-$	TFSI <sup>-</sup> or NTf2 <sup>-</sup>
	2,2,2-trifluoro-N-(trifluoromethanesulfonyl)acetamide	$[\text{CF}_3\text{SO}_2\text{-N-COCF}_3]^-$	TSAC <sup>-</sup>
	Alkylsulfates	$[\text{ROSO}_3]^-$	NA

At the beginning of this century, the concept of “task specifically functionalized ionic liquids” (TSILs) was proposed, with the purpose of further tailoring ILs with peculiar properties by modifying their structures for specific applications [73, 74]. Most efforts were concentrated on the incorporation of structural or functional groups into a branch attached to the cation, especially imidazolium cations (see Fig. 2-2). For instance, it was demonstrated that the addition of ether and alcohol functional groups on the alkyl side chain of imidazolium cations was beneficial for lowering the viscosity of the original RTIL, as well as increasing the solubility of inorganic salts [75]. Moreover, formulating conventional imidazole cations with a fluororous tail, which acts as a surfactant, can facilitate the emulsification of fluoroalkanes with RTIL phases and thus expand the application of RTILs as a novel solvent [76]. Therefore, TSILs provide new and vital insights into the design and synthesis of modern RTILs.

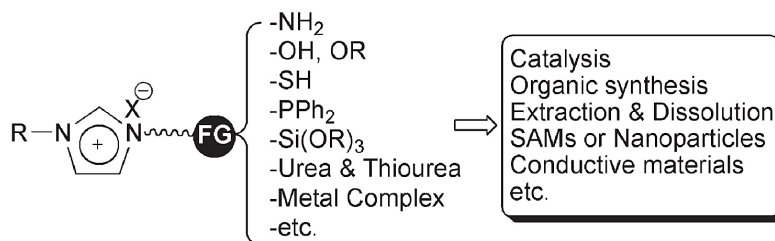


Fig. 2-2 Functional imidazolium salts for task-specific ionic liquids [74].

### 2.2.1.2 Physicochemical properties of RTILs

The basic properties of RTILs that have been widely acknowledged include their negligible vapor pressure, low flammability, relative high thermal stability (decomposition temperatures are generally above 300°C [71]), low melting temperature ( $T_m$  - most RTILs exhibit supercooling properties, i.e., the freezing temperature is lower than the melting temperature [70]) and wide electrochemical window (e.g., 4.0-5.5 V [77-79]). Other important physicochemical properties of particular concern are listed in the following paragraphs.

#### (1) Viscosity ( $\eta$ )

Unfortunately, RTILs suffer from an inherent drawback of high viscosity, emerging as the major hindrance for practical application. Typically, the viscosity of an RTIL is around 30-50 cP and can even reach several hundreds of cP, which is much higher than that of water (0.89 cP at room temperature) [80]. It has been concluded that strong electrostatic interactions, hydrogen bonding and van der Waals interactions of RTILs, are responsible for the high viscosity [81, 82]. For example, increasing the length of alkyl groups of organic cations enhances viscosities [83], due to the stronger van der Waals interactions encountered. The viscosity relies on the temperature. The relationship can be described by the modified form of the Vogel-Fulcher-Tammann (VFT) equation ( $\eta_0$ ,  $D$  and  $T_0$  are constants) [84-86]:

$$\eta = \eta_0 \exp\left(\frac{DT_0}{|T - T_0|}\right) \quad (2-6)$$

Clearly, the viscosity ( $\eta$ ) decreases with increasing temperature ( $T$ ). Researchers have proposed the application of RTIL-based solvents with the addition of small amounts of co-solvents, such as benzene and alcohol, which can produce a significant reduction in the viscosity of the RTIL [87]. Seddon et al. [88] systematically investigated the influence of different co-solvents on the viscosity of RTIL 1-butyl-3-methylimidazolium tetrafluoro-borate (BMI-BF<sub>4</sub>). They found an interesting phenomenon that the viscosity of mixtures depends predominantly on the mole fraction of the added co-solvents, instead of their identities (as seen in Fig. 2-3). Controlling the viscosity of RTILs to a low level is of particular importance, since the viscosity impacts both the diffusion coefficient and the conductivity.

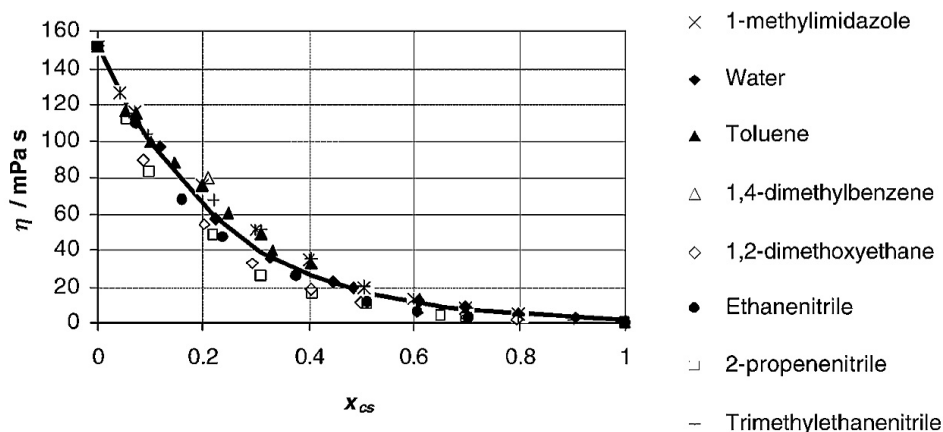


Fig. 2-3 Viscosity at 20°C of co-solvents and BMI-BF<sub>4</sub> mixtures vs. mole fraction of co-solvents [88].

### (2) Diffusion coefficient ( $D_0$ )

The diffusion coefficient is critical for evaluating the transport properties of RTILs which, in turn, affect the reaction kinetics of an electrochemical process. The diffusion coefficient ( $D_0$ ) is inversely proportional to the viscosity, reflected by the Stokes-Einstein equation [89]:

$$D_0 = \frac{k_B T}{c \pi \eta r} \quad (2-7)$$

$k_B$  is the Boltzmann constant,  $c$  is a constant (usually equal to 6) and  $r$  is the effective hydrodynamic radius. A typical value of the diffusion coefficient in RTILs is  $1 \times 10^{-7}$  cm<sup>2</sup>/s [90]. For chemical and electrochemical processes, the reaction kinetics (rate constants), especially those for diffusion-controlled reactions, in RTILs are lower than those in aqueous solutions [68]. This phenomenon is mainly due to the viscous nature of RTILs. The high viscosity results in a slow diffusion process (according to the Stokes-Einstein equation), which, in turn, diminishes mass transport in RTILs and lowers the reaction rates. On the other hand, such reduced processes also restrict the charge transfer process, which offers a way for obtaining smooth deposits during electrochemical reactions [91].

### (3) Conductivity ( $\lambda$ )

Due to free mobility of the ions, RTILs are considered to have potentially high conductivities, serving as favorable electrolyte alternatives to conventional organic solvents for electrochemical applications [92]. However, the conductivity is strongly limited by the viscosity for RTILs.

Similar to the diffusion coefficient, the conductivity is also inversely linked to the viscosity and governed by the Walden rule:

$$\Lambda\eta = \text{cons.} \quad (2-8)$$

Compared with an aqueous KOH solution (29.4 wt%) used as the electrolyte in alkaline batteries, with a conductivity of 540 mS/cm [8], RTILs have remarkably lower conductivities in the range of 0.1-30 mS/cm [79, 93]. The highest conductivity reported so far (up to 110 mS/cm [94]) is for RTILs with fluorohydrogenerated anions; however, the toxicity of fluorine ions is a safety concern for their applications.

#### (4) Solvation ability

One advantage of using RTILs as a solvent is their capability of dissolving a variety of organic and inorganic compounds [71]. RTILs are identified as polar solvents and the overall solvation ability is generally determined by their polarity [95]. However, studies have also pointed out that unlike molecular solvents, the solvent properties of ionic liquids cannot be simply ascribed to conventional parameters like polarity and dielectric constant, but more sophisticated modeling is needed to provide accurate explanations [96]. Solute-solvent interactions in RTILs are typified by the formation of ion pairs. The dissolution of tris(4-bromophenyl)amine (TBPA) in RTILs with imidazolium cations is ascribed to the strong ion pairing-like solvation effect between the TBPA<sup>+</sup> cation and the anion of the RTILs. In addition, reaction kinetics are related to the phenomenon of ion-pairs [92].

#### 2.2.1.3 Structure-physicochemical properties relationship

It is well known that all the physicochemical properties of RTILs are strongly dependent on the nature of the ions. Information regarding the ion-based properties can serve as a powerful guide for the future structural design of RTILs.

As one example, cations are addressed here. Imidazolium, being the key component in most traditional RTILs, has a low melting temperature and desirable electrochemical stability. When evaluating the role as electrolytes that RTILs play in electrochemical processes, RTILs with ammonium cations are also good alternatives with wider EW than those with imidazolium cations. The improved EW is due to the better cathodic stability of ammonium [97, 98].

Pyrrolidinium is the cation that has been investigated to a great degree for RTILs in recent years. RTILs composed of pyrrolidinium cations and TFSI<sup>-</sup> anions not only have comparable EW to RTILs with ammonium cations, but are superior to their competitors in view of viscosity and conductivity [99].

A second example involves cation counterparts. The selection of anions, either inorganic or organic, contributes to the diversity of physicochemical properties of RTILs. It has been shown that the solubility of RTILs with water is mainly determined by their anions [88]. For instance, RTILs with [PF<sub>6</sub>]<sup>-</sup> and TFSI<sup>-</sup> anions are insoluble with water and thus commonly referred as hydrophobic ILs; while those with halides and DCA<sup>-</sup> anions are water-soluble and are called hydrophilic ILs. In terms of specific RTILs, fluorohydrogenate RTILs are well known for their high conductivity [100] that cannot be approached by any other RTIL systems. RTILs with alkylsulfates anions are usually cheap, easy to prepare and free from halide contamination [101]. They are also good alternatives to RTILs that contain fluorine atoms when toxicity issues are a concern [68]. Recently, with the desire for high stability against moisture absorption and low solubility of water, RTILs with TFSI<sup>-</sup> anions have found their way in applications, especially in electrochemical deposition (ECD) [77, 78]. Furthermore, instead of assessing the physicochemical properties of cations and anions separately, combining the advantages of both beneficial properties from anions and cations can produce favorable properties for RTILs. A telling example is quaternary phosphonium dicyanamide RTIL. The DCA<sup>-</sup> anion provides the RTIL with low viscosity, while the phosphonium cation guarantees good thermal and chemical stability, compensating for the low thermal stability of the DCA<sup>-</sup> anion [6].

### **2.2.2 Application of RTILs in electrodeposition and energy storage devices**

Intensive studies on RTILs in recent years have explored their applications in many areas. Two main directions include the ECD field and energy storage devices; the progress for both is discussed in the following.

With respect to ECD, aprotic RTILs (without dissociable H<sup>+</sup> and unable to donate hydrogen) have been adopted as popular electrolytes. The first merit of aprotic RTILs, compared with conventional aqueous electrolytes, is their intrinsic ability to avoid hydrogen evolution and improve the current efficiency, which qualifies them as fascinating electrolytes for electrodeposition of various metals. ECD of metallic Sn [91], Mn [99] and Cu [102] in RTIL

BMP-TFSI is reported to successfully inhibit hydrogen evolution and achieve current efficiency as high as 100%. Aprotic RTILs also provide an extra benefit of modifying the deposit morphology during ECD. These imide-type RTILs are increasingly applied in ECD of metals and alloys [103]. Zhu et al. [3] carried out ECD of metallic Ni in BMP-TFSI and obtained Ni deposits with fine grain size (10-15 nm). Serizawa et al. [1] further investigated ECD of Ag, as well as its mechanism, from RTILs with TFSI<sup>-</sup> anions. They proposed that the morphology of electrodeposited Ag was controlled by the adsorption of TFSI<sup>-</sup> anions on the electrode, which can depress crystal growth and facilitate the generation of dense faceted granular Ag deposits. Apart from TFSI<sup>-</sup> anions, RTILs based on other anions like DCA<sup>-</sup> and PF<sub>6</sub><sup>-</sup> have also received interest for improving deposit morphology. Leong et al. [7] claimed that the morphology of deposited Sn from EMI-DCA is dependent on the deposition potential. A favorable morphology for hollow hexagonal tubes was formed at relative low reduction potential, while a sponge morphology and dendrite growth were observed with increasing potential. Using 1-butyl-3-methyl imidazolium hexafluorophosphate (BMI-PF<sub>6</sub>) as the electrolyte, a homogeneous film of electrodeposited Ru was achieved [104]. It is notable that RTILs with imidazolium and pyrrolidinium cations and TFSI<sup>-</sup> and DCA<sup>-</sup> anions are the most heavily studied electrolytes for electrochemical processes.

The application of RTILs has also been extended to a diversity of energy storage devices, including batteries, electrochemical capacitors and fuel cells. Aprotic RTILs are still the favorite choices, with protic ILs (PILs, produced through proton transfer from a Brønsted acid and a Brønsted base) receiving increasing attention in recent years.

#### (1) RTILs used for batteries

A large portion of the current literature involving RTILs for batteries is focused on Li-based batteries (e.g., [105-111]). The remaining studies cover other battery technologies such as Zn-based [112], Na-based [113] and Si-based batteries [114]. In particular, for Li-based batteries, the first among all attributes of applying RTILs as electrolytes or electrolyte components is that they are safer alternatives compared with flammable and volatile organic liquids. An electrolyte composed of propylene carbonate and BMP-TFSI (50:50 wt%) for Li-ion batteries was shown to possess higher thermal stability than a system with no BMP-TFSI, allowing the achievement of high cycling stability as well as high capacity [115]. Additionally, widely used polymer

electrolytes (PEs) for Li-based batteries have intrinsically poor ionic conductivity ( $<0.1$  mS/cm). The adoption of RTILs in PEs is beneficial for improving electrolyte conductivity. For example, propylene carbonate containing a PIL pyrrolidinium nitrate exhibits a conductivity as high as 14 mS/cm at 20°C [116], which is a significant improvement in electrolyte performance for conventional Li-based batteries. RTIL electrolytes also show the potential capability of forming a stable solid electrolyte interface (SEI) layer on the electrode surface and are, therefore, beneficial for improving electrochemical performance for Li-ion batteries [5].

## (2) RTILs used for electrochemical capacitors

Due to their large EW (can exceed 5 V) and non-volatile characteristic, RTILs have competed with traditional organic electrolytes (with EW around 2-3 V) and aqueous solutions (with EW around 1 V) for application in electrochemical capacitors to achieve high specific energy. A study using RTILs with imidazolium/pyrrolidinium cations and TFSI anions as electrolytes for thin film planar supercapacitors showed high EWs ( $>3$  V) and good wettability compared with carbon electrodes [117], which is good for charge storage. Compared with commonly used organic electrolytes, the adoption of RTILs as electrolyte components also shows promise for expanding the operational temperature for supercapacitors. For instance, an electrolyte containing a PIL pyrrolidinium nitrate can potentially allow the supercapacitor to operate at a low temperature of -40°C with a desirable conductivity of 9 mS/cm [118]. The minimum operational temperature of commercial products in the solvent propylene carbonate is above -25°C and is limited by the reduced electrolyte conductivity and diffusion of ions [119]. RTILs are advantageous for modifying the electrode for supercapacitors as well. Hantel et al. [120] demonstrated that the use of RTIL 1-ethyl-3-methyl-imidazolium tetrafluoroborate (EMI-BF<sub>4</sub>) with an organic solvent acetonitrile is beneficial for enhancing the electrochemical activation reaction of electrodes, as well as the achievable specific capacitance for supercapacitors.

## (3) RTILs used for fuel cells

Application of PILs in fuel cells, especially in polymer electrolyte membrane fuel cells (PEMFC) has emerged as a hot topic in the last few years. For current proton-conducting membranes utilized in fuel cell technology, water is essential for providing the polymer membranes with high proton conductivity. One major motivation of using PILs in fuel cells is to break their

operational temperature limit that is restricted by the boiling point of water [121]. Several kinds of PILs, including 1-butyl-3-methylimidazolium trifluoromethanesulfonate, 1-ethylimidazolium trifluoromethanesulfonate [122] and trimethylammonium phosphate [123], have been investigated as potential membrane components for fuel cells to increase their operating temperatures above 150°C. These PILs act as intrinsic proton conductors under anhydrous conditions and possess good thermal and electrochemical stability at the same time.

### **2.2.3 Summary**

RTILs are increasingly recognized as potential electrolytes/electrolyte components for application in various energy storage devices and electrodeposition. The physicochemical properties of RTILs, such as low vapour pressure, wide electrochemical window and good thermal stability, play a significant role in achieving desirable performance, including high specific energy and long cycle life specifically for battery applications. RTILs with imidazolium and pyrrolidinium cations, together with TFSI<sup>-</sup>, PF<sub>6</sub><sup>-</sup> and DCA<sup>-</sup> anions, are among the most promising candidates for use in batteries. PILs, which act as proton transfer carriers, exhibit good conductivity and are favorable in both electrochemical capacitors and fuel cells. It is also worth noting that the development of TSILs can expand the applicability of RTILs to meet various requirements in their practical applications.

## **2.3 Novel electrolyte systems for Zn anode rechargeable batteries**

As stated above, RTILs offer various physicochemical properties as potential electrolytes for energy storage devices. In order to guarantee high energy output, electrochemical application of RTILs in batteries depends significantly on their transport properties, mainly ionic conductivity. In spite of the fact that RTILs can potentially offset a number of shortcomings, including dendrite formation at the anode and drying-out of the electrolyte due to water evaporation, high viscosities and moderate conductivities essentially limit widespread adoption of RTILs in their neat forms as electrolytes to batteries, specifically Zn anode rechargeable batteries. Novel electrolyte systems containing RTILs need to be explored and developed to facilitate the complete utilization of the merits of RTILs.

### **2.3.1 Functionalized RTILs systems**

Functionalized RTILs (or TSILs) are currently attractive systems since they provide researchers a way to explore novel electrolytes to suit specific requirements in batteries. As introduced in

Section 2.2.1.1, the physicochemical properties of functionalized RTILs are adjustable by incorporating different functional groups into the cations/anions (mostly cations).

With respect to battery applications, sulfone and ether are two functional groups that have been extensively introduced to RTILs with imidazolium or ammonium cations. The sulfone group has been shown to have good solvation ability for electrolyte salts and shows good compatibility with cathode materials used for Li-based batteries [124]. The function of the ether group is manifold, largely due to its oxygen unit. Firstly, ether oxygen facilitates a decrease in RTIL viscosity [125], which is mostly preferred for achieving the practical application of RTILs. Secondly, the ether group helps hinder crystallization below room temperature [126], which is good for improving the operational temperature of batteries. Thirdly, the ether group increases polarity and salt solubility [127]. In particular, for application in Zn-air batteries, Kar et al. [128] synthesized novel RTILs with oligo-ether side chains, aimed at solubilizing Zn ions and promoting the reversibility of Zn electrochemistry. Other special functionalized RTILs are those defined as electroactive RTILs with a redox shuttle. They are designed for preventing overcharge of the battery, where excess charge is used to drive the redox shuttle and not overcharge of the cell material. One example is from Forgie's group [129], in which they applied a ferrocene-functionalized imidazolium electroactive ionic liquid to a Li-ion battery, with ferrocene as the redox shuttle to prevent battery overcharge.

The investigation of functionalized RTILs as battery electrolytes is still in its preliminary stage, with more effort needed to facilitate their practical application. In addition, an electrolyte composed of either RTILs or functionalized RTILs alone appear unlikely to meet the complex requirements for battery applications, since the low conductivity issue still remains unsolved.

### **2.3.2 Mixed electrolyte systems**

Mixing RTILs with other solvents, especially molecular co-solvents, has been found to cause a noticeable decrease in viscosity and increase in conductivity [130]. Desirable additives to RTILs are those that not only improve the transport properties of the electrolytes, but also do not impair the advantages of RTILs, including the low flammability and wide electrochemical window. Xiang et al. [131] investigated a binary electrolyte system composed of IL N-butyl-methyl piperidinium bis(trifluoromethanesulfonyl)imide, with the addition of sulfone (tetramethylene sulfone, TMS). Their results showed that this mixed electrolyte maintained excellent

electrochemical stability and non-flammability and exhibited improved ionic conductivity. Recently, organic solvents, such as acetonitrile [132] and DMSO [133], and inorganic solvents like water [134] were studied as electrolyte additives to RTILs as well, with the purpose of improving the physicochemical and electrochemical performance of the mixed electrolytes.

By considering the achievement of high electrolyte conductivity as a priority, aqueous based electrolytes with incorporation of RTILs as additives have great potential for application in Zn anode rechargeable batteries. On the one hand, using aqueous solution guarantees desirable electrolyte conductivity. On the other hand, which is critically important, the addition of an RTIL is good for modifying Zn deposit morphology and provides a way to solve the Zn dendrite problem. For instance, Ma et al. [112] explored a novel electrolyte system for Zn/polyaniline rechargeable batteries. This new electrolyte system mixed acidic aqueous solutions with RTIL 1-ethyl-3-methylimidazolium ethyl sulfate (EMI-ES), in which the ratio of water to EMI-ES was 92:8 by volume. The formation of Zn dendrites was restrained during charging of the batteries according to their study. All these results give new insights into exploring novel battery electrolytes for Zn anode rechargeable batteries.

### **2.3.3 Summary**

The achievement of Zn anode rechargeable batteries with high electrochemical performance and long cycle life exerts demanding requirements on the development of electrolyte systems. Current research progress in this field demonstrates that neither traditional aqueous solutions nor modern RTILs alone can fulfill the requirements for a workable electrolyte. Novel electrolyte systems, with the idea of harnessing the benefits from both RTILs and other solvents/aqueous solutions, are essential to be established to fill the research gap. The following Chapters 3-6 present our efforts and achievements in exploring novel electrolytes containing RTILs for application to Zn anode rechargeable batteries.

## Chapter 3 Preliminary characterization of selected RTILs: Study of Zn redox behavior

### 3.1 Overview

With the purpose of revealing the feasibility of using RTILs as electrolytes for Zn anode rechargeable batteries, this chapter presents the fundamental knowledge obtained regarding Zn redox behavior in four RTILs, together with the physicochemical characterization of RTILs. The selection of RTILs is restricted to heavily studied ones utilized in electrodeposition and Li-based batteries, i.e., BMP-TFSI, MPP-TFSI, EMI-TFSI and BMP-DCA. These RTILs are composed of two types of cations, pyrrolidinium and imidazolium, and two types of anions, TFSI<sup>-</sup> and DCA<sup>-</sup>.

Thermal properties, i.e., melting temperatures, and electrochemical windows of the four selected RTILs are first examined. Emphasis is then given to investigating the electrochemistry of Zn in these RTILs, including Zn redox reversibility, kinetic properties, reaction mechanisms and cyclability. An understanding of the dependence of Zn redox behavior on the types of cations and anions of the studied RTILs is established, shedding light on further screening of desirable RTILs candidates for Zn anode rechargeable batteries.

### 3.2 Experimental methods

Four RTILs, i.e., BMP-TFSI (C<sub>11</sub>H<sub>20</sub>F<sub>6</sub>N<sub>2</sub>O<sub>4</sub>S<sub>2</sub>, 99.5 wt%, with <0.05 wt% water, <0.001 wt% Cl<sup>-</sup> and 0.001 wt% Br<sup>-</sup>), MPP-TFSI (C<sub>12</sub>H<sub>22</sub>F<sub>6</sub>N<sub>2</sub>O<sub>4</sub>S<sub>2</sub>, 99.9 wt%, with <0.002 wt% water, <0.0001 wt% Cl<sup>-</sup> and 0.0001 wt% Br<sup>-</sup>), EMI-TFSI (C<sub>8</sub>H<sub>11</sub>F<sub>6</sub>N<sub>3</sub>O<sub>4</sub>S<sub>2</sub>, 99.5 wt%, with <0.05 wt% water, <0.001 wt% Cl<sup>-</sup> and 0.001 wt% Br<sup>-</sup>) and BMP-DCA (C<sub>11</sub>H<sub>20</sub>N<sub>4</sub>, >98 wt%, with 0.7 wt% water, 0.3 wt% Cl<sup>-</sup> and 0.01 wt% Na), as well as Zn bis(trifluoromethanesulfonyl)imide (Zn-TFSI, 99 wt%), were purchased from Solvionic. Zn-TFSI was dissolved in each RTIL by stirring overnight to produce a 0.1 mol/L Zn<sup>2+</sup> solution. Reagents were used as received, without extra purification. Before testing, in order to remove trapped air and water residue, the RTILs were vacuum dried at 60 to 80°C for at least one hour.

#### 3.2.1 DSC measurements

Differential scanning calorimetry (DSC) was performed on a TA Instrument Q10 with a liquid nitrogen cooling system. The calorimeter was purged with nitrogen during measurements. RTIL samples were first frozen to -100°C and then heated to 50°C at a rate of 5°C/min. The

crystallization temperature  $T_c$  and the melting temperature  $T_m$  were taken as the extrapolated onset temperatures, determined by the intersections of the slopes of the exothermic crystallization peak and the endothermic melting peak with their corresponding baselines, respectively.

### 3.2.2 Electrochemical measurements

All electrochemical experiments (cyclic voltammetry (CV), potentiodynamic polarization and chronoamperometry (CA)) were accomplished with a Zahner IM6 electrochemical workstation (controlled by Thales 4.15 software), in conjunction with a BASi (Bioanalytical Systems, Inc.) C-3 cell stand (EF-1085 BASi), which supports a 3-electrode cell configuration and has a Faraday cage to minimize electrical interference. CV experiments were undertaken at 500 mV/s to explore the electrochemical windows for blank RTILs. Scan rates of 10 mV/s, 20 mV/s, 50 mV/s and 100 mV/s were utilized for studying Zn redox reactions in each RTIL. The potential scan range was -1.5 to 0.8/1.0 V vs. Fc/Fc<sup>+</sup> (ferrocene/ferrocenium ions) for RTILs with TFSI<sup>-</sup> anions and -1.55 to -0.35 V vs. Fc/Fc<sup>+</sup> for BMP-DCA. Potentiodynamic polarization experiments were performed within the same potential windows at a scan rate of 1.0 mV/s. Chronoamperometry experiments were applied to obtain the diffusion coefficient of the Zn species in each RTIL during the reduction process. These experiments were accomplished by stepping the potential of the working electrode from an initial value, where no reaction occurs, to a sufficiently negative potential where the reduction of Zn species is a diffusion-controlled process.

The electrochemical experiments adopted a 3-electrode cell configuration. A Pt electrode (1.6 mm diameter, MF-2013 BASi) and a micro-Pt electrode (10  $\mu$ m diameter, MF-2005 BASi) were used as the working electrode (WE). A Pt wire (0.5 mm diameter, MW-1032 BASi) was used as the counter electrode (CE). The reference electrode (RE) was assembled with an Ag/AgCl wire inserted in a glass tube filled with BMP-DCA solution containing 50:50 mol% Fc/Fc<sup>+</sup> as the internal potential standard. The inner solution of the reference electrode was separated from the studied solution by a porous Vycor tip (MF-2042 BASi). During testing, the solution was continuously purged with nitrogen gas to prevent reactions that may be introduced by oxygen and water adsorption.

### 3.2.3 SEM observation

The morphology of Zn deposits remaining on the electrode surface after CV cycling (last cycle ends at the reduction scan) was analyzed with a Hitachi S-3500N scanning electron microscope (SEM) operated at 15 kV.

## 3.3 Results and discussion

### 3.3.1 Thermal properties for each blank RTIL

Fig. 3-1 shows typical DSC results for each as received RTIL. Similar to most RTILs, all the studied ones show supercooling properties, i.e., the freezing temperature is lower than the actual melting temperature [70]. For BMP-TFSI and MPP-TFSI, previously reported multiple melting and crystallization behavior [78] was observed. The small peaks denoted as  $T_1$  and  $T_2$  correspond to the formation of mesophases at a relatively high temperature before crystallization took place. The low crystallization (around  $-40$  to  $-60^\circ\text{C}$ ) and melting temperatures (less than  $-10^\circ\text{C}$ , except for MPP-TFSI) for these RTILs are especially beneficial for batteries used for road/marine transportation in cold weather conditions (e.g., Canada).

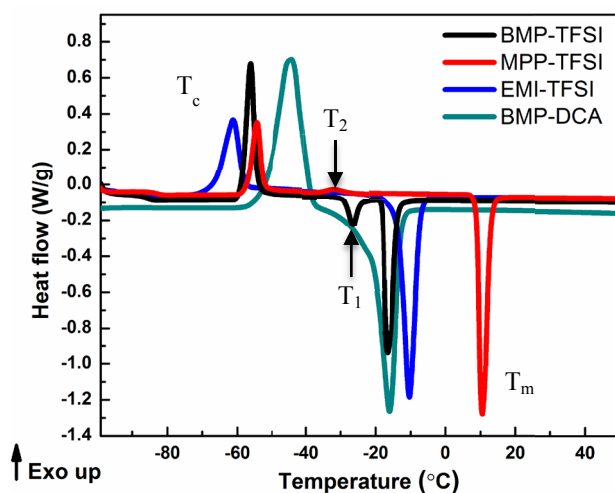


Fig. 3-1 DSC traces for the four blank RTILs.

### 3.3.2 Electrochemical window for each blank RTIL

Fig. 3-2 displays the CV results for the four blank RTILs. In order to determine the electrochemical windows, anodic potential limits as well as cathodic potential limits, were derived from the CV curves for each RTIL (Table 3-1).

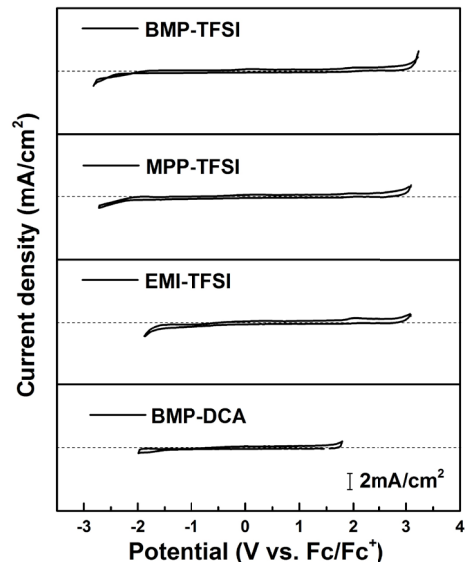


Fig. 3-2 CV results for the four blank RTILs (at a scan rate of 500 mV/s).

Compared with aqueous electrolytes ( $EW < 1 \text{ V}$  [135]), ionic liquids are much more electrochemically stable, characterized by wider EWs: BMP-TFSI (5.7 V) > MPP-TFSI (5.5 V) > EMI-TFSI (4.7 V) > BMP-DCA (3.2 V). The wide EW for RTILs is not only beneficial for potentially high electrode efficiency, but also guarantees a relative robust system when considering the deleterious effect on the cathodic limit of RTILs induced by water absorption.

Table 3-1 Cathodic/anodic limit potentials for studied RTILs

RTIL	Cathodic potential limit (V)	Anodic potential limit (V)
BMP-TFSI	-2.6	3.1
MPP-TFSI	-2.5	3.0
EMI-TFSI	-1.7	3.0
BMP-DCA	-1.6	1.6

### 3.3.3 Electrochemistry of Zn in studied RTILs

Following the physicochemical examination of the four blank RTILs, this section presents the results for a systematic investigation of Zn electrochemistry in each RTIL. Three aspects discussed include Zn redox reversibility, Zn kinetics and cyclability.

### 3.3.3.1 Zn redox reversibility

Fig. 3-3 shows CV results for Zn redox (second cycle) in each RTIL. When comparing Fig 3-3 and Fig. 3-2, it is clear that within the potential range where Zn redox takes place, no reactions are observed in the original blank RTILs. CV provides a means of predicting Zn reversibility in each RTIL, which is an essential electrode property for rechargeable batteries. Based on the CV results, Table 3-2 summarizes the peak potential separation ( $\Delta E_p$ ), the ratio of cathode and anode peak current densities ( $j_{pc}/j_{pa}$ ) and the potential shift and current density change as the scan rate is varied for Zn redox in each RTIL. BMP-DCA has the smallest  $\Delta E_p$  value (0.42 V), followed by EMI-TFSI (0.74 V). The  $\Delta E_p$  values for Zn redox in BMP-TFSI and MPP-TFSI are larger than 0.9 V. The lower viscosities (provided by the manufacturer) for EMI-TFSI (36 cp at 25°C) and BMP-DCA (45 cp at 20°C) relative to BMP-TFSI (84 cp at 25°C) and MPP-TFSI (103 cp at 25°C) can account for the smaller peak potential separation, i.e., the lower overpotential for Zn redox reactions. The peak positions for Zn redox in all four RTILs varies with scan rate. In general, as the scan rate increases, the cathodic and anodic potentials shift to more negative and positive positions, respectively. In other words, an increase in overpotential is needed to initiate the electrode reactions (i.e., increased activation energy) with increasing scan rate, which is commonly observed for quasi-reversible reactions. If the CV results at scan rates of 100 mV/s and 20 mV/s are compared, both the cathodic and anodic peak positions for Zn redox are relatively stable in BMP-DCA and EMI-TFSI. Specifically for BMP-DCA, the peak potential shifts are less than 0.04 V. On the other hand, the peak potentials vary markedly (more than 0.1 V) for BMP-TFSI and MPP-TFSI. The peak current density ratios for Zn redox in both BMP-TFSI and MPP-TFSI are closer to one than those for EMI-TFSI and BMP-DCA. For RTILs with TFSI<sup>-</sup> anions, the anodic and cathodic processes may be quite different or less reversible, which contributes to differences in the shape and peak current ratio when compared with the RTIL with DCA<sup>-</sup> anion, i.e., BMP-DCA. The latter shows better reversibility. The discrepancy between RTILs with imidazolium cations and pyrrolidinium cations may be due to different viscosities (which affect conductivity and Zn species diffusion) and/or solubilities of Zn in these RTILs. EMI-TFSI has a high conductivity or ion mobility, which may contribute to the narrow peaks relative to the broad ones for BMP-TFSI and MPP-TFSI. In addition, for an ideal reversible reaction, the anodic and cathodic ratios of the peak current densities at 20 mV/s and 100 mV/s should be 0.447, which is the ratio of the square root of the scan rates. From Table 3-2, it is clear

that Zn redox in RTILs with pyrrolidinium cations and TFSI<sup>-</sup> anions, particularly MPP-TFSI, shows this type of behavior.

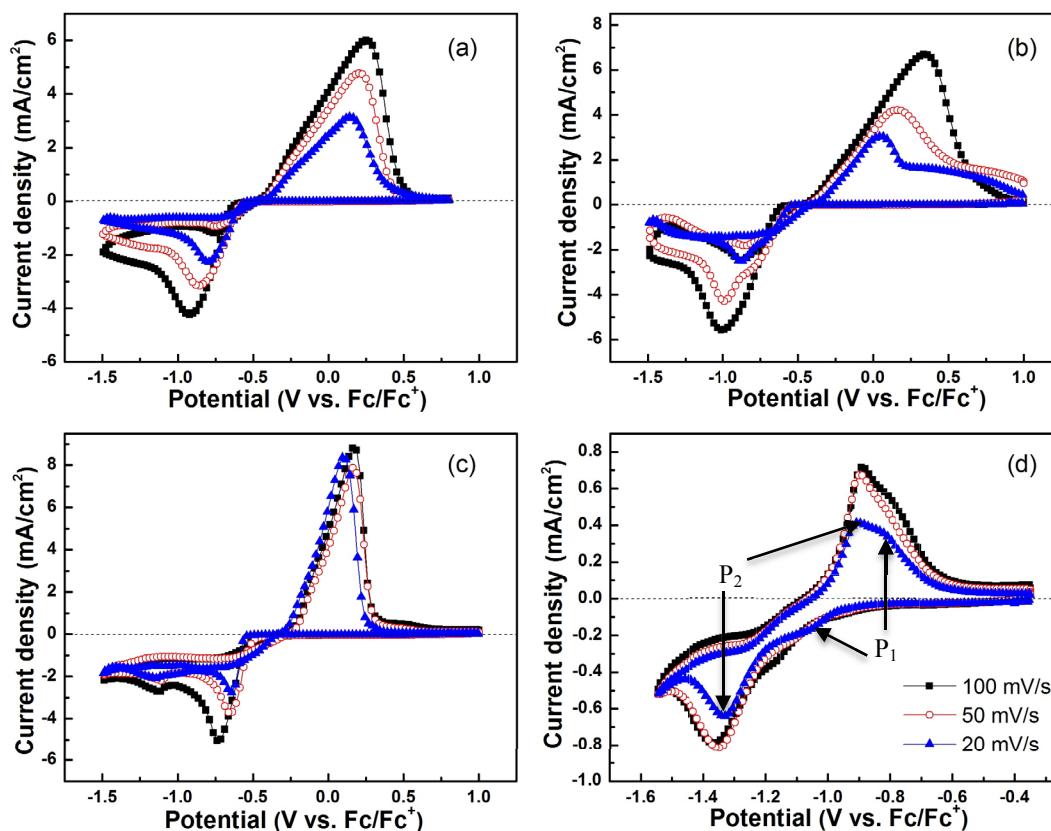


Fig. 3-3 CV results for 0.1 M Zn<sup>2+</sup> in (a) BMP-TFSI, (b) MPP-TFSI, (c) EMI-TFSI and (d) BMP-DCA at different scan rates (20 mV/s, 50 mV/s and 100 mV/s).

A broadened Zn oxidation peak is visible for MPP-TFSI, especially at a scan rate of 20 mV/s (Fig. 3-3 b). This is likely primarily related to the high viscosity of MPP-TFSI, as well as the relatively low solubility of Zn ions in MPP-TFSI. As the CV scan reverses from the positive potential to the negative potential, Zn deposits are initially formed on the electrode surface. During the reverse scan, these Zn deposits are oxidized when the critical potential is reached. Since the solubility of Zn ions is low in MPP-TFSI and the viscosity of MPP-TFSI is high, at slow scan rates most of the oxidized Zn ions accumulate in the vicinity of the electrode surface with less being dissolved in solution and/or transported from the electrode surface. As a result, the Zn ion concentration at the electrode surface builds up, which then slows down the subsequent oxidation of Zn deposits.

Table 3-2 Characterization of Zn redox in four RTILs

	BMP-TFSI	MPP-TFSI	EMI-TFSI	BMP-DCA
$\Delta E_p(20)^a$ (V)	0.93	0.91	0.74	0.42
$\delta E_{pc(100-20)}^b$ (V)	0.13	0.14	0.089	0.037
$\delta E_{pa(100-20)}^c$ (V)	0.11	0.30	0.045	0.015
$j_{pc}/j_{pa(20)}^d$	0.72	0.83	0.33	1.6
$j_{pc(20)}/j_{pc(100)}^e$	0.54	0.45	0.54	0.81
$j_{pa(20)}/j_{pa(100)}^f$	0.52	0.45	0.98	0.57

<sup>a</sup> Peak potential separation at 20 mV/s ( $\Delta E_p$  for BMP-DCA was calculated as the peak potential separation between the two potentials that correspond to the highest reduction and oxidation current densities, i.e., the P<sub>2</sub> couple as marked in Fig. 3-3 and 3-4).

<sup>b, c</sup> Cathodic and anodic peak potential shifts for scan rates of 100 mV/s and 20 mV/s, respectively (expressed as absolute values).

<sup>d</sup> Peak current density ratio at 20 mV/s.

<sup>e, f</sup> Cathodic peak current density ratios and anodic peak current density ratios for 20 mV/s and 100 mV/s, respectively.

The CV results demonstrate that for all four RTILs, Zn redox reactions are quasi-reversible. In terms of potential-dependent characteristics (peak potential separation and peak potential shift with scan rate), the Zn redox reaction exhibits superior reversibility in EMI-TFSI and BMP-DCA compared with BMP-TFSI and MPP-TFSI due to the smaller overpotential required. However, considering the peak current density ratio at a given scan rate and the variation in peak current density with scan rate, the Zn redox reaction in MPP-TFSI and BMP-TFSI shows better reversibility than in either EMI-TFSI or BMP-DCA.

The three redox cycles for the Zn redox reactions at 100 mV/s (Fig. 3-4) reveal Zn nucleation on the Pt working electrode from each RTIL. Similar Zn reduction behavior with an obvious nucleation loop can be found in RTILs with TFSI<sup>-</sup> anions (Fig. 3-4 a-c). For the forward scan (reduction direction), the potential at which Zn ions begin to nucleate on the Pt surface is more negative during the first scan cycle than during the second cycle (subsequent cycles are similar to the second one). This is due to the fact that after the first cycle, the formation of Zn nuclei on the Pt surface can facilitate subsequent Zn nucleation/growth, which, in turn, decreases the activation energy for Zn nucleation. This is reflected in the decreased overpotential needed to

drive the reduction process. A similar result was also reported for Sn electrochemical deposition from 1-ethyl-3-methylimidazolium dicyanamide [7].

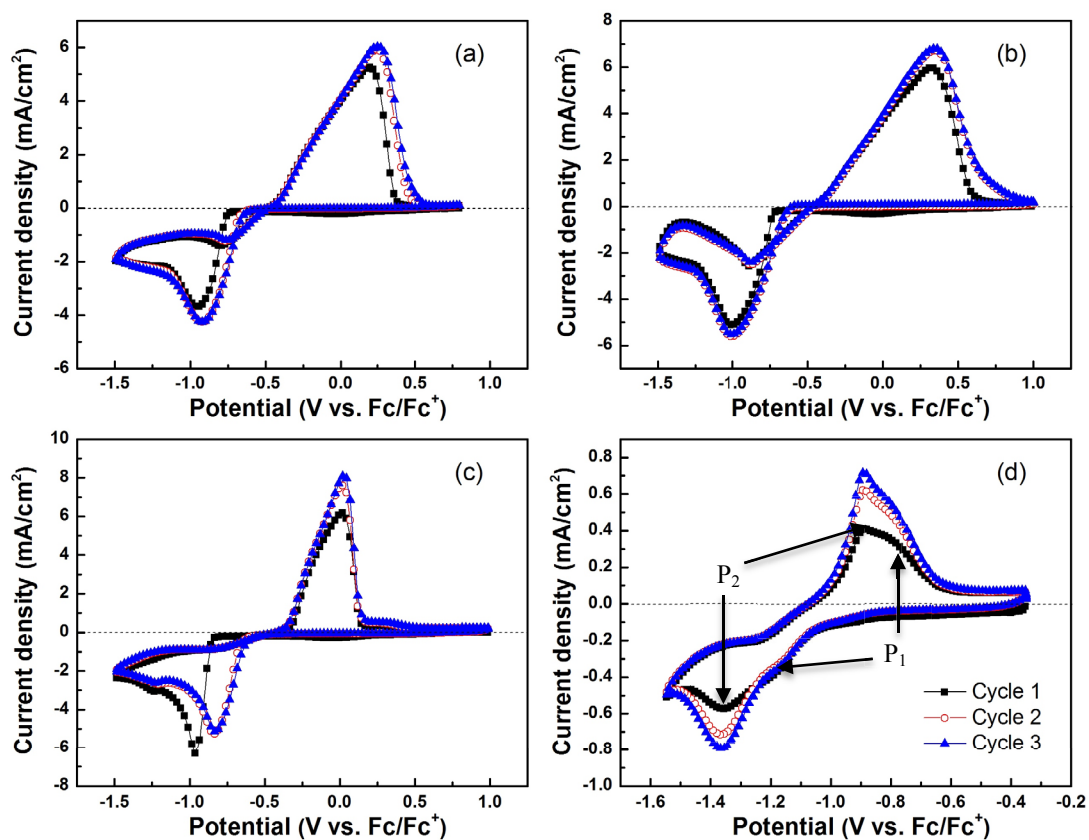


Fig. 3-4 CV results (3 cycles at 100 mV/s) for 0.1 M Zn<sup>2+</sup> in (a) BMP-TFSI, (b) MPP-TFSI, (c) EMI-TFSI and (d) BMP-DCA.

With the same pyrrolidinium cation, however, Zn redox behavior in BMP-DCA is much different than RTILs with TFSI<sup>-</sup> anions. First of all, no Zn nucleation loop is observed, suggesting that Zn nucleation is inhibited during the reduction process in BMP-DCA. A different result was reported by Deng et. Al [136], where a Zn nucleation loop was found during electrochemical deposition from a BMP-DCA electrolyte. This discrepancy may be related to the working electrode, as glassy carbon was used in their study and Pt was used in this study. In addition, instead of a single Zn redox couple observed for RTILs with TFSI<sup>-</sup> anions, two distinguishable Zn redox couples (denoted as P<sub>1</sub> and P<sub>2</sub> in both Fig. 3-3 d and Fig. 3-4 d) are observed for BMP-DCA. This indicates a different form of the Zn species and a different Zn redox reaction mechanism for BMP-DCA relative to RTILs with TFSI<sup>-</sup> anions. Furthermore, the Zn redox current density for BMP-DCA is approximately 4 to 10 times lower than that for RTILs

with TFSI<sup>-</sup> anions. The current density difference is reduced for lower scan rates. Further explanation regarding the Zn redox reaction mechanism and current density variation are provided along with the polarization results in the following section.

### 3.3.3.2 Zn redox kinetics

Fig. 3-5 shows polarization curves (scan rate of 1 mV/s) for the Zn species in each RTIL. For RTILs with TFSI<sup>-</sup> anions, there appears to be only one redox reaction within the scan range (Fig. 3-5 a-c). On the other hand, two redox reactions, indicated by two peaks are observed for BMP-DCA (Fig. 3-5 d). The two peaks, in fact, correlate with P<sub>1</sub> and P<sub>2</sub> in the CV curves in Figs. 3-3 d and 3-4 d. Tafel equations (3-1) and (3-2) are commonly used to derive the kinetic parameters for electrode reactions.

$$\text{At high cathodic overpotential: } \log i = \log i_0 - \alpha n F \eta / (2.3 RT) \quad (3-1)$$

$$\text{At high anodic overpotential: } \log i = \log i_0 + (1-\alpha) n F \eta / (2.3 RT) \quad (3-2)$$

where  $i_0$  is the exchange current,  $\alpha$  is the charge transfer coefficient ( $0 < \alpha < 1$ ),  $n$  is the number of electrons involved in the electrode reaction,  $F$  is the Faraday constant (96,485 C/mol of electrons),  $R$  is the universal gas constant (8.314 J/mol·K),  $T$  is the absolute temperature (K) and  $\eta$  is the overpotential.

The relationship between  $\log i$  and overpotential  $\eta$  was fit by linear regression using Originpro 8.4 software. The range of  $|\eta|$  for linear fitting was constrained within the range of 40 mV to 110 mV, so as to guarantee that the contribution from the back reaction is less than 4% and the current is less than 30% of the limiting current from mass transfer effects. According to Equations (3-1) and (3-2), the values for  $\alpha$  and  $n$  can be obtained from the slopes of the fitted cathodic and anodic lines. The exchange current density is the value derived from the intercepts of the fitted lines.

Fig. 3-5 a-c show similar oxidation current peaks. For EMI-TFSI and BMP-TFSI, a dramatic drop in current density is followed by an oxidation peak, suggesting that Zn deposits are readily oxidized. The current density remains relatively high after the oxidation current peak for MPP-TFSI, indicating incomplete oxidation, which is consistent with the corresponding CV

observations. In Fig. 3-5 d, at potentials more negative than  $\sim -1.2$  V, an abrupt increase in current density is observed, which is likely related to the decomposition of BMP-DCA.

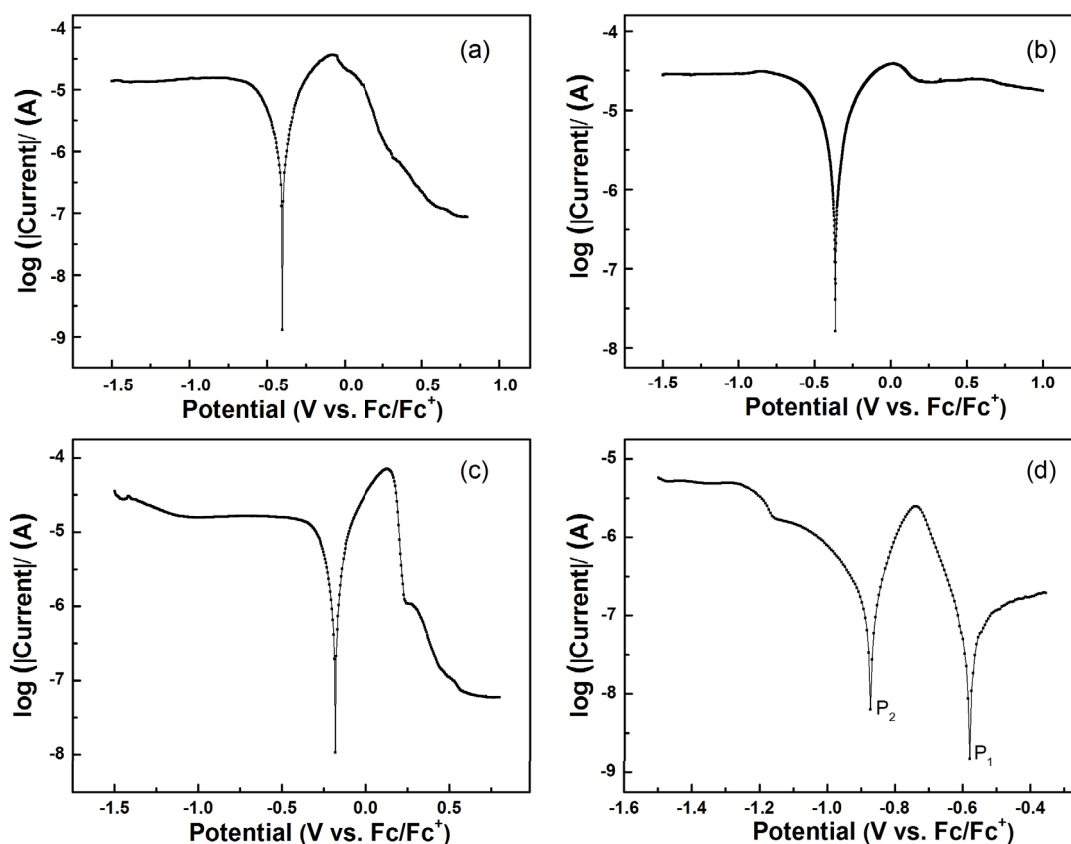


Fig. 3-5 Polarization curves obtained at a scan rate of 1 mV/s for Zn species in RTILs: (a) BMP-TFSI, (b) MPP-TFSI, (c) EMI-TFSI and (d) BMP-DCA.

Table 3-3 compares the kinetic parameters for the Zn species in the four RTILs. The kinetic properties rely on both the cations and anions, with the anions dominating. With respect to the exchange current density, among RTILs with TFSI<sup>-</sup> anions, the Zn species has the highest reaction rate in the RTIL with imidazolium cations. This is in agreement with the CV results, where the peak current density for Zn redox in EMI-TFSI is the highest (Fig. 3-4 c). The Zn redox reaction mechanism is mainly influenced by the anion, which determines the form of dissolved Zn species and the corresponding reaction procedure. From the Tafel analysis, the derived electron number,  $n$ , involved in the electrode reactions provides insight into the forms of Zn species in the different RTILs, as well as the electrode reaction mechanisms. In RTILs with

TFSI<sup>-</sup> anions,  $n$  is close to 2, suggesting the presence of Zn<sup>2+</sup> ions. The Zn redox reaction most likely follows a single step, two-electron process:

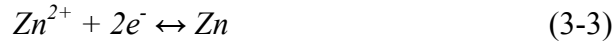
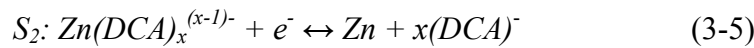
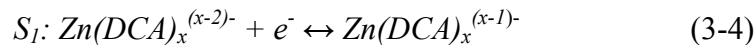


Table 3-3 Kinetic parameters for Zn redox reactions in four RTILs

	$D_0^a$ ( $\times 10^{-7}$ cm <sup>2</sup> /s)	Kinetic parameters		
		$j_0^b$ (mA/cm <sup>2</sup> )	$\alpha$	$n$
BMP-TFSI	4.3	$6.7 \times 10^{-3}$	0.49	2.0
MPP-TFSI	6.2	$4.1 \times 10^{-3}$	0.44	1.9
EMI-TFSI	4.4	$9.9 \times 10^{-3}$	0.43	1.9
BMP-DCA	0.036	$P_1: 2.3 \times 10^{-3}$	0.74	1.1
		$P_2: 6.6 \times 10^{-3}$	0.38	0.92

<sup>a</sup> Diffusion coefficient; <sup>b</sup> Exchange current density,  $j_0 = i_0/A$  ( $A$  is the area of working electrode).

In BMP-DCA, the value of  $n$  for each redox reaction is close to 1, indicating a single-electron, two-step electrode reaction. Considering the strong complexing ability of the DCA<sup>-</sup> anion with metal ions [136], after dissolving Zn-TFSI salt into BMP-DCA, Zn<sup>2+</sup> ions can easily form complex ions with the DCA<sup>-</sup> anion. The following electrode reactions for the Zn species are proposed ( $S_1$  and  $S_2$  correspond to the peaks  $P_1$  and  $P_2$  in Fig. 3-5, respectively):



The value of  $x$  is suggested as 3 according to a typical titration experiment conducted by Deng et al. [136]. The proposed Zn redox reaction mechanism can be used to explain the current density behavior in BMP-DCA observed from the CV results in Fig. 3-3 d. At high scan rates (50 mV/s and 100 mV/s), the insufficient response time hindered the occurrence of step  $S_1$ , indicated by the suppressed redox couple  $P_1$ , leading to the low current density. At a low scan rate of 1 mV/s, the two-step reactions ( $S_1$  and  $S_2$ ) in BMP-DCA can occur and the total electron transfer number is equal to 2, yielding a comparable exchange current density to that derived from RTILs with

TFSI<sup>-</sup> anions. The exchange current densities for the Zn species in each RTIL are of the same order of magnitude, i.e., 10<sup>-3</sup> mA/cm<sup>2</sup>.

Fig. 3-6 displays the CA results for the Zn species in all four electrolytes. To avoid the capacitive current induced by double-layer charging, only the *i-t* data during the last 70% of the step time were taken into consideration. For a planar electrode, the Cottrell equation [137] is commonly used to depict the relationship between current and time obtained from a CA experiment. The diffusion coefficient of the electroactive species is derived from the slope of current *i* vs. *t*<sup>-1/2</sup>, as shown in equation (3-6).

$$i = nFACD_0^{1/2}/(\pi^{1/2}t^{1/2}) \quad (3-6)$$

Here *n* is the stoichiometric number of electrons involved in the reaction, *F* is the Faraday constant (96,485 C/mol of electrons), *A* is the electrode area (cm<sup>2</sup>), *C* is the concentration of electroactive species (mol/cm<sup>3</sup>) and *D*<sub>0</sub> is the diffusion coefficient for the electroactive species (cm<sup>2</sup>/s).

Table 3-3 lists the diffusion coefficient for the Zn species in each RTIL. It is clear that the diffusion coefficients for the Zn species in all RTILs with TFSI<sup>-</sup> anions are about the same order of magnitude and Zn<sup>2+</sup> ions are proposed to be the electroactive species. On the other hand, the diffusion coefficient for the Zn species is two orders of magnitude lower in BMP-DCA. This result can be explained by considering the Stokes-Einstein equation shown in equation (2-7): *D*<sub>0</sub> = *κT*/*cπ**ηr* (where *κ* is the Boltzmann constant, *T* is the absolute temperature, *η* is the viscosity, *c* is a constant and *r* is the effective hydrodynamic radius). Even though the viscosity of BMP-DCA is lower than the viscosity of the RTIL composed of pyrrolidinium cations and TFSI<sup>-</sup> anions, it is the large size of the complex ions, Zn(DCA)<sub>*x*</sub><sup>(*x*-2)<sup>-</sup></sup> and Zn(DCA)<sub>*x*</sub><sup>(*x*-1)<sup>-</sup></sup>, formed in BMP-DCA that leads to the smaller *D*<sub>0</sub>. In other words, the large Zn complex ions in BMP-DCA move sluggishly. The CA results support the mechanisms proposed for the Zn electrode reactions in different RTILs based on the polarization experiments.

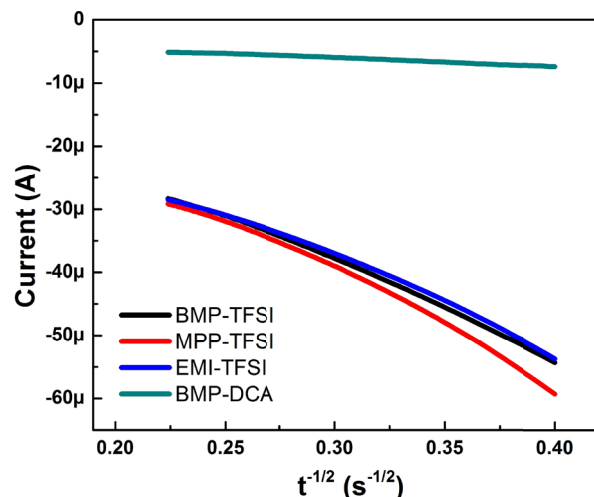


Fig. 3-6 Relationship of current vs.  $t^{-1/2}$  for chronoamperometry experiments for Zn species reduced in the four studied RTIL.

Among the tested RTILs, based on the kinetic properties, the Zn redox reaction has comparable exchange current densities (i.e., reaction rates) at slow scan rates. Both the CV and polarization results demonstrate that in EMI-TFSI, the Zn redox reaction can achieve a slightly higher current density of  $9.9 \times 10^{-3} \text{ mA/cm}^2$  than the rest of the RTILs. A large diffusion coefficient for the electroactive species means a small concentration overpotential was established during the electrochemical process, which is preferred in terms of achieving a potentially high energy density for batteries. Therefore, in considering the diffusion rate for the Zn species in the RTILs, the TFSI<sup>-</sup> anion is more desirable than the DCA<sup>-</sup> anion. On the other hand, the CV results show that the Zn redox reaction has the lowest peak potential separation ( $\Delta E_p$ ) in BMP-DCA among the RTILs studied, which could be beneficial for a battery system in terms of energy density. It is speculated that RTILs composed of imidazolium cations and DCA<sup>-</sup> anions may be promising electrolyte candidates in view of the reversibility and current densities for Zn redox reactions.

### 3.3.3.3 Zn redox cyclability and deposit morphology

The cyclability for Zn redox in an RTIL gives insight regarding the cycle life of a battery with a Zn electrode. CV cycling experiments (100 cycles) for Zn species in RTIL solutions were conducted to simulate the repeated charge/discharge process. Three kinds of typical behavior (obtained from Fig. 3-7) for Zn redox cycling were observed:

- (1) In BMP-TFSI and MPP-TFSI, the cyclability for Zn redox is almost lost after several tens of cycles, as indicated by the disappearance of the oxidation peak and the expanded reduction peak.
- (2) In EMI-TFSI, the current density for Zn redox decreases after cycling. After 100 cycles, the current density reaches zero, demonstrating a termination of Zn redox after cycling.
- (3) In BMP-DCA, with increasing cycling number, the current densities for both Zn reduction and oxidation increase. This means that Zn redox in this RTIL may have good cyclability.

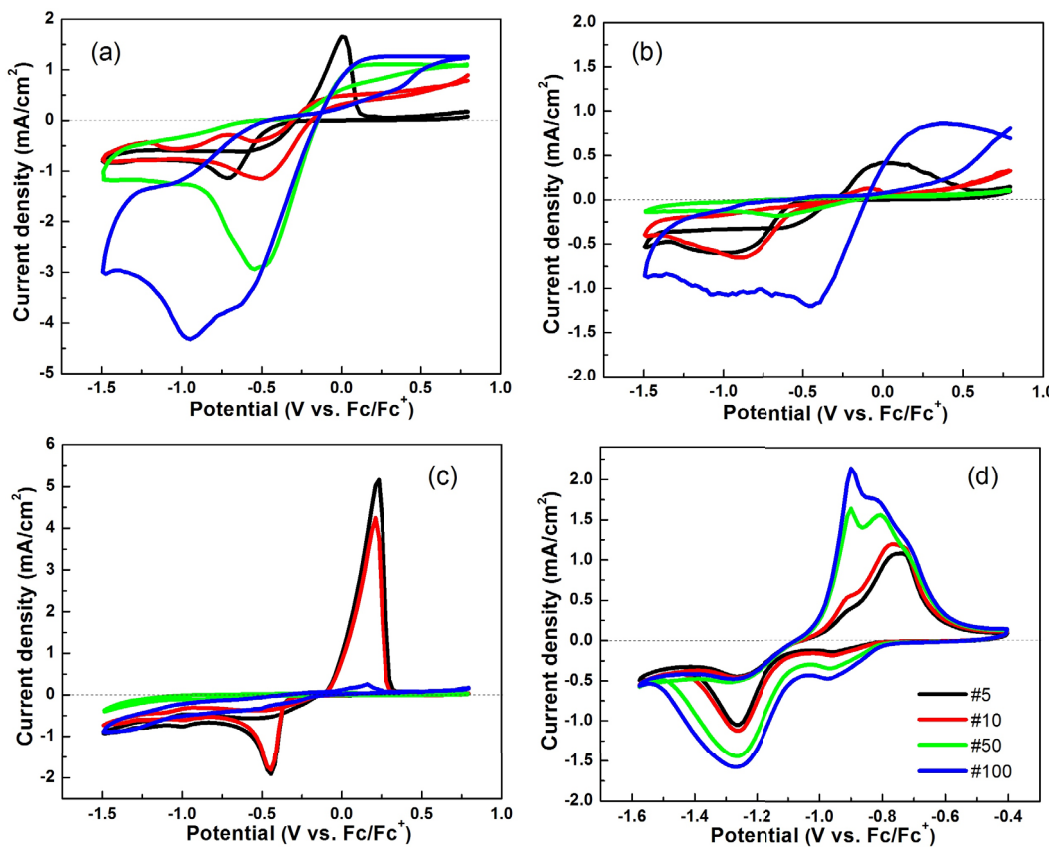


Fig. 3-7 CV cycling at 10mV/s for 100 cycles (# refers to cycle number): (a) BMP-TFSI, (b) MPP-TFSI, (c) EMI-TFSI and (d) BMP-DCA.

The morphology of Zn deposits obtained during CV cycling in the RTILs (Fig. 3-8) provides insight for the various Zn redox behaviors. For BMP-TFSI and MPP-TFSI, Zn clusters were the prevalent morphology for deposited Zn, indicating enhanced Zn deposition but suppressed oxidation, which sheds light on the expanded Zn reduction peak and disappearing oxidation curve in the CV results (Fig. 3-7 a-b). Gradual agglomeration of the Zn rods was observed in EMI-TFSI with increasing cycle number, which decreases the contact area between Zn active

material and the electrolyte and accounts for the suppressed electrochemical reaction. In BMP-DCA, on the other hand, finely dispersed rods composed of Zn granular deposits possess high surface area, providing and maintaining active sites for the continuous occurrence of electrochemical reactions. Consequently, good cyclability for Zn redox was found in BMP-DCA.

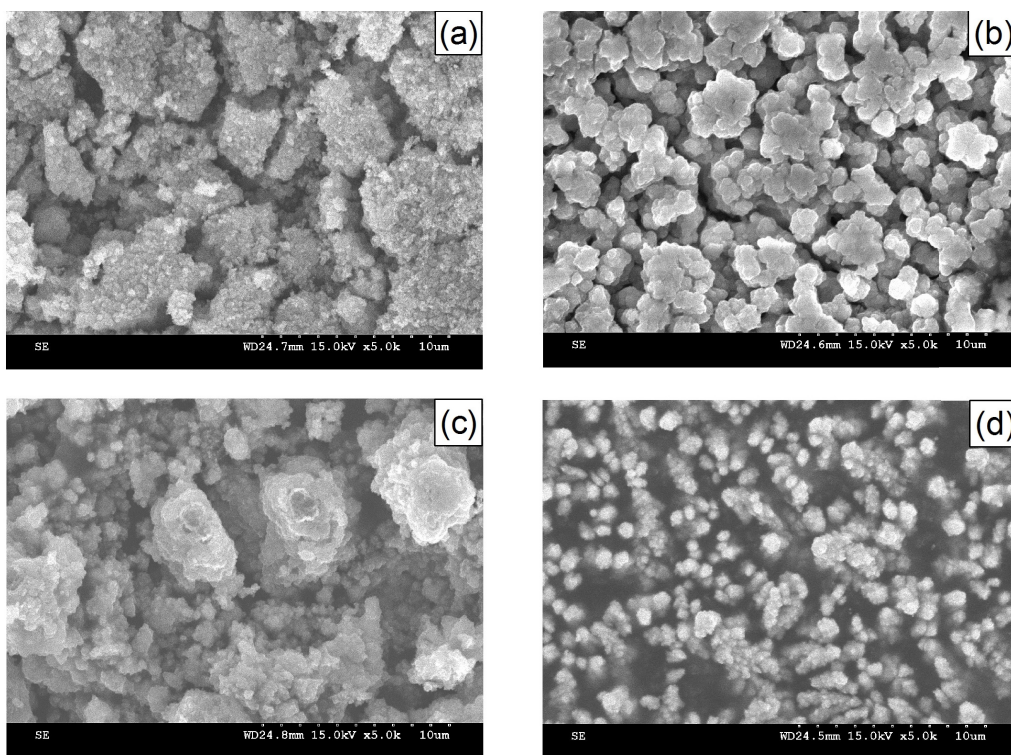


Fig. 3-8 SEM secondary electron (SE) images of Zn deposits after CV cycling from RTILs: (a) BMP-TFSI, (b) MPP-TFSI, (c) EMI-TFSI and (d) BMP-DCA.

### 3.4 Summary

In this Chapter, the advantages of four different RTILs (BMP-TFSI, MPP-TFSI, EMI-TFSI and BMP-DCA) applied as battery electrolytes were firstly demonstrated. The intrinsically lower crystallization and melting temperatures for RTILs are beneficial for batteries to achieve desirable low temperature efficiency, especially under cold weather conditions. In addition, the wider electrochemical windows, compared with aqueous solutions, for RTILs are preferred based on electrode efficiency. Furthermore, Zn redox reactions in the RTILs were systematically investigated. It was found that both the cations and anions of the RTILs exert effects on the Zn redox reactions, while the kinetic behavior of the Zn species is mainly controlled by the type of anions.

(1) With regard to Zn redox reversibility, the CV results show that in terms of peak potential separation and peak potential shift with scan rate, Zn redox exhibits superior reversibility in EMI-TFSI and BMP-DCA compared with BMP-TFSI and MPP-TFSI. However, in terms of peak current density ratio and its variation with scan rate, Zn redox in MPP-TFSI and BMP-TFSI shows better reversibility than in EMI-TFSI and BMP-DCA.

(2) With regard to Zn redox kinetics, the exchange current density for Zn species was found to be the highest in the RTIL with imidazolium cations (EMI-TFSI). The Zn species dissolve in the four RTILs with different forms according to the anions, which not only influence the reaction mechanisms, but also affect the diffusion coefficient of the electroactive species. In RTILs with TFSI<sup>-</sup> anions, Zn<sup>2+</sup> ions are present with the electrode reaction occurring in a single-step, two-electron transfer process. In the RTIL with DCA<sup>-</sup> anions (BMP-DCA), however, a complex ion between Zn ions and DCA<sup>-</sup> forms, turning the electrode reaction into a two-step, single-electron process. The diffusion coefficient for Zn<sup>2+</sup> ions is two orders of magnitude higher than that for the complex ion ( $Zn(DCA)_x^{(x-2)-}$ ).

(3) With regard to Zn redox cyclability, the RTIL with DCA<sup>-</sup> anion, i.e., BMP-DCA, appears as a desirable electrolyte. Finely dispensed rods composed of Zn granular deposits are dominant in BMP-DCA after cycling, which maintains a high surface area and accounts for the good Zn redox cyclability. On the contrary, the increasing agglomeration of Zn clusters in RTILs with TFSI<sup>-</sup> anions upon cycling leads to diminished cyclability. The current results also give insight to further screening of potential RTILs candidates, such as EMI-DCA.

## Chapter 4 Electrolytes composed of water added RTILs with TFSI<sup>-</sup> anions

### 4.1 Overview

In Chapter 3, RTILs with pyrrolidinium or imidazolium cations and TFSI<sup>-</sup> anions were demonstrated as potential electrolyte candidates for Zn anode rechargeable batteries. However, limited by the low mobility of ions caused by high viscosity, the conductivities of RTILs, especially those with a so called “hydrophobic” anion TFSI<sup>-</sup>, are still not suitable compared with conventional aqueous electrolytes to meet the needs for energy storage applications. Therefore, in this Chapter, water is introduced into three RTILs with TFSI<sup>-</sup> anions, BMP-TFSI, MPrP-TFSI (due to its lower viscosity, MPrP-TFSI is studied as a replacement for MPP-TFSI) and EMI-TFSI, with the purpose of increasing the conductivity of these RTIL-based electrolytes.

Water interaction with ions of these RTILs is explored, shedding light on the effect of water addition on the electrolyte conductivity. Correlation of the interaction between water and each RTIL with Zn redox behavior (kinetics and reversibility) is investigated as well, with the focus on discovering the optimum water amount to be added. Further, Zn deposits obtained from the RTILs without and with controlled amounts of water are compared, in order to reveal the influence of water addition on Zn deposit morphology.

### 4.2 Experimental methods

BMP-TFSI (99.5 wt%, with <0.05 wt% H<sub>2</sub>O, <0.001 wt% Cl<sup>-</sup> and <0.001 wt% Br<sup>-</sup>) and Zn-TFSI (99 wt%) were purchased from Solvionic. MPrP-TFSI (C<sub>10</sub>H<sub>18</sub>F<sub>6</sub>N<sub>2</sub>O<sub>4</sub>S<sub>2</sub>, >99 wt%, with <0.01 wt% H<sub>2</sub>O and <0.01 wt% halides) and EMI-TFSI (99.9 wt%, with <0.01 wt% H<sub>2</sub>O and <0.01 wt% halides) were purchased from IoLiTec. The reagents were used as received, without additional purification. The RTIL and water mixtures were prepared by adding deionized (DI) water (18.2 MΩ•cm, 0-5.0 wt%) to each RTIL that was pretreated by vacuum drying at 100°C overnight. Due to the hydrophobicity of these RTILs, a two-phase system was formed. The first set of mixtures (I) was initially shaken manually to spread out large water droplets into finely dispersed droplets in each RTIL, then underwent ultrasonic agitation for 1.0-1.5 hrs and was finally allowed to sit overnight. It is notable that a cloudy solution/suspension was observed when the water amount was above 1.0 wt%. Therefore, in order to minimize sampling variation, all samples for DSC and FTIR measurements were taken from the middle part of the prepared mixtures in the vials. Another batch of mixtures (II) composed of RTILs with 0.5, 1.0, 2.0, and

2.5 wt% water additions was prepared separately following the same procedure. Zn-TFSI was dissolved in each of these mixtures (II) by stirring overnight to produce a 0.1 mol/L  $\text{Zn}^{2+}$  solution for subsequent electrochemical measurements.

#### **4.2.1 Conductivity Measurements**

Conductivity measurements were accomplished using an Omega CDB-387 bench-top microprocessor-based conductivity/resistivity/TDS meter. Two electrode probes were available with cell constants  $K= 0.1/\text{cm}$ ,  $1.0/\text{cm}$  and  $10.0/\text{cm}$  for measurement over ranges of  $0.01\text{-}100\ \mu\text{S}/\text{cm}$ ,  $100\ \mu\text{S}/\text{cm}\text{-}100\ \text{mS}/\text{cm}$  and  $100\text{-}2000\ \text{mS}/\text{cm}$ , respectively. For ionic liquid samples with conductivities of about a few  $\text{mS}/\text{cm}$ , a glass dip type probe with cell constant  $K= 1.0/\text{cm}$  was chosen.

To conduct the measurements, a 2.0 mL standard solution ( $4.5\ \text{mS}/\text{cm}$ ) was firstly loaded into a 4.0 mL shell vial kept at  $25^\circ\text{C}$  in a water bath. The probe was calibrated with the standard solution. After calibration, the probe was fully rinsed with acetone and ethanol and hot air dried to avoid any contamination. 2.0 mL of sample solution was then loaded into the shell vial half immersed in the water bath and then the probe was inserted. Before the sample temperature was stable at  $25^\circ\text{C}$ , the probe was lifted up and lowered down slightly to ensure the temperature of the sample liquid was uniform. When the temperature was stable at  $25^\circ\text{C}$ , the probe was kept stationary and then a conductivity reading was taken after 30 s. Note that cleaning after each test is of importance to ensure an accurate measurement.

#### **4.2.2 FTIR Measurements**

FTIR measurements were carried out on a Nicolet 8700 spectrophotometer with a DTGS (deuterated triglycine sulfate) detector. An attenuated total reflectance (ATR) attachment with a diamond crystal was used to obtain IR spectra. The wavelength resolution was  $4.0/\text{cm}$ . A small volume of the sample ( $\sim 2.0\ \mu\text{l}$ ) was needed to cover the surface of the diamond crystal. During measurements, an alumina lid was utilized to isolate samples from the atmosphere, so as to minimize the influence of moisture from air.

#### **4.2.3 DSC Measurements**

Differential scanning calorimetry (DSC) measurements were performed on a TA Instruments Q10 with a liquid nitrogen cooling system. The calorimeter was purged with nitrogen during the

measurements. Sample masses were in the range of 15-20 mg. All DSC scans were performed at a heating rate of 5.0°C/min. Samples were first quenched to -100 to -80°C and then heated to 200°C. The melting temperature  $T_m$  was taken as the extrapolated onset temperature that was determined by the intersection of the slope of the endothermic melting peak and its baseline.

#### 4.2.4 Electrochemical Measurements

Cyclic voltammetry, chronoamperometry and potentiodynamic polarization were performed with a Zahner IM6 electrochemical workstation (controlled by Thales 4.15 software), in conjunction with a BASi system (Bioanalytical Systems, Inc.). A C-3 cell stand (EF-1085 BASi), which supports a 3-electrode cell configuration, with a Faraday cage was used to minimize electrical interference. CV experiments were undertaken at a scan rate of 100 mV/s. The potential scan range was within the range of -3.55 to 3.0 V vs. Fc/Fc<sup>+</sup> to examine the electrochemical window for each RTIL without or with water, while -1.7 to 0.8 V vs. Fc/Fc<sup>+</sup> was the scan range for studying Zn redox reactions. CA experiments were accomplished by stepping the potential of the working electrode from an open circuit potential to a sufficiently negative potential where the reduction of the Zn species was a diffusion-controlled process. Potentiodynamic polarization experiments were performed at a scan rate of 1.0 mV/s. The electrochemical experiments adopted a 3-electrode cell configuration. A Pt electrode (1.6 mm diameter, MF-2013 BASi) was used as the WE and a Pt wire (0.5 mm diameter, MW-1032 BASi) was used as the CE. The RE was assembled with a Pt wire inserted in a glass tube filled with BMP-TFSI solution containing 50:50 mol% Fc/Fc<sup>+</sup> as the internal potential standard. The inner solution of the reference electrode was separated from the studied electrolyte by a porous Vycor tip (MF-2042 BASi). During test, the electrolyte was first purged with nitrogen gas for 10 min and then blanketed with nitrogen gas during testing.

#### 4.2.5 First-principles modeling

Gas-phase density functional theory (DFT) calculations were performed on cluster models composed of BMP<sup>+</sup>, TFSI<sup>-</sup>, H<sub>2</sub>O and Zn<sup>2+</sup> species using the hybrid B3LYP exchange-correlation functionals and the 6-311+G(2d,2p) basis set as implemented in Gaussian09 [138]. Full-geometry optimization and frequency calculations were also performed at this level of theory. All results were confirmed to have no imaginary frequency. All binding energies reported were based on zero-point (ZP) corrected energies of the optimized structures. Binding energies were

computed as the difference in ZP-corrected energies before and after cluster formation. Following this convention, a positive binding energy denotes that binding is stable.

#### 4.2.6 Electrodeposition and SEM

Zn coatings were electrodeposited from each RTIL, without or with a controlled amount of water, on Pt coated Si substrates at a constant potential (peak cathodic potential according to the CV curves for Zn redox) for 1 hr. A 3-electrode cell configuration was also applied, with the same RE used for the electrochemical measurements and a Zn plate as the CE placed vertically within 20 mm from the WE. After deposition, the WE was thoroughly rinsed with acetone, ethanol and dried in air. The morphology of the deposits was analyzed with a Hitachi S-4700 SEM operated at 15 kV.

### 4.3 Results and discussion

#### 4.3.1 Conductivity dependence of studied RTILs with water addition

Fig. 4-1 shows the conductivity variation of each RTIL as a function of water concentration. For all three curves, the conductivity reached the peak value by adding water within the range of 2.0-2.5 wt%. With water additions exceeding 2.5 wt%, the conductivity data was not stable and reliable, due to the solubility limit of water in the RTILs.

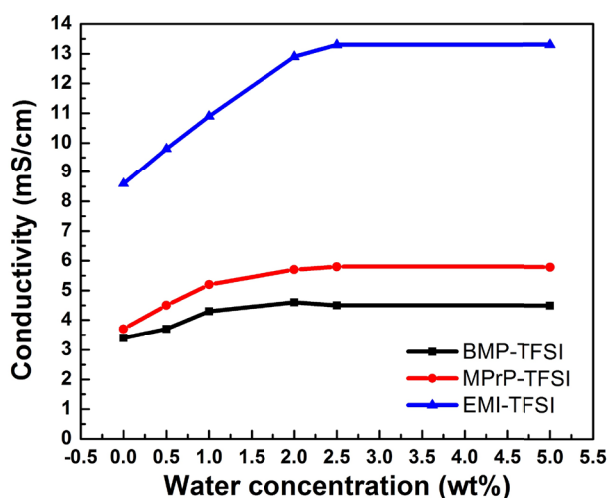


Fig. 4-1 Conductivity of studied RTILs with different amounts of water.

The highest conductivities of the RTILs with added water were within 4.5-14 mS/cm and still one to two orders of magnitude lower compared with the conductivity of 29.4 wt% KOH aqueous electrolyte (540 mS/cm [8]). Nevertheless, the RTIL electrolytes have conductivities

comparable to or higher than those of electrolytes using lithium salts as solutes for state-of-the-art Li-based batteries (2.0-12 mS/cm) [139].

FTIR and DSC tests were further applied to reveal the interaction of water with the RTILs. As shown in Fig. 4-2, for the three RTILs with the same TFSI<sup>-</sup> anion, two distinct bands (located at ~3630/cm and ~3560/cm, respectively) in the FTIR spectra are present, exhibiting increased absorbance with increasing water concentration. The two bands are attributed to the asymmetric  $\nu_3$  and symmetric  $\nu_1$  stretching modes of water bound to the TFSI<sup>-</sup> anion.

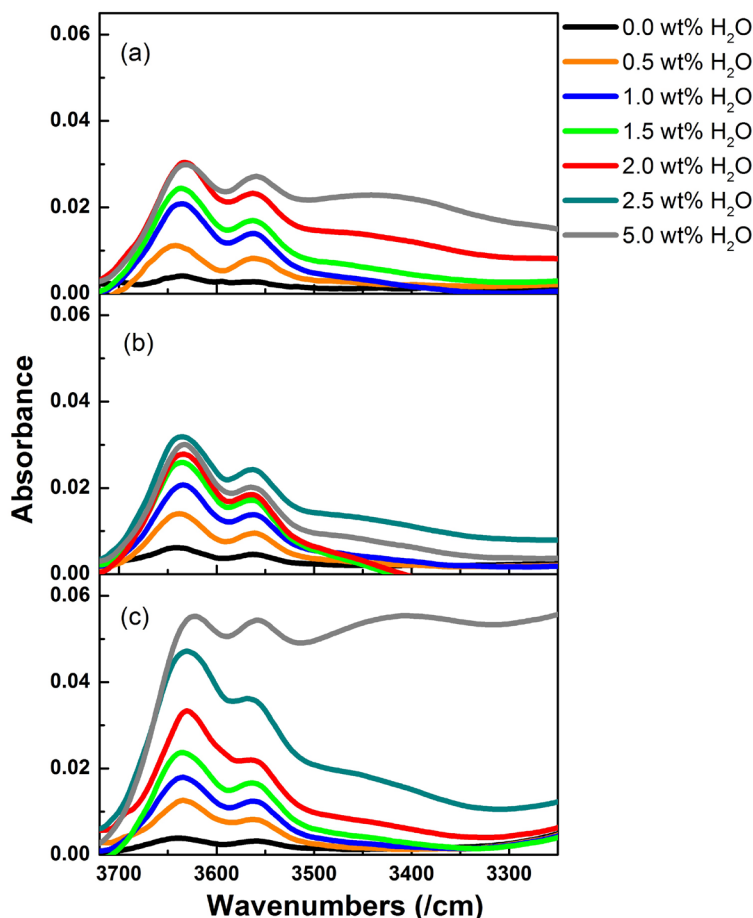


Fig. 4-2 FTIR spectra for each RTIL with different amounts of water additions: (a) BMP-TFSI, (b) MPrP-TFSI and (c) EMI-TFSI.

The wave number difference at maximum absorbance for these two bands is around 70-80/cm. As reported in [140, 141], this indicates that one water molecule interacts with two TFSI<sup>-</sup> anions by H-bonding. In addition, for the spectrum detected at high water concentrations, a broader band was found, suggesting the presence of free water aggregates.

DSC results displayed in Fig. 4-3 are consistent with the FTIR results. The black curves represent the phase transformations during the melting process for each RTIL. M and M' denote the melting peaks, where M corresponds to melting of the bulk RTIL. M' for both BMP-TFSI and EMI-TFSI represents melting of a metastable liquid crystal.

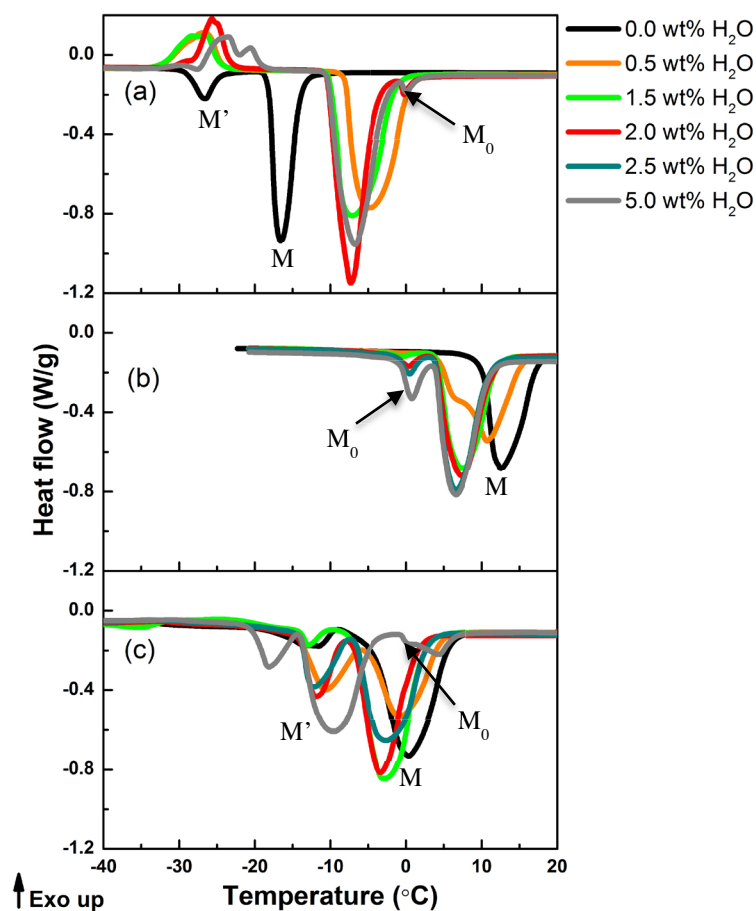


Fig. 4-3 DSC traces for each RTIL with different amounts of water additions: (a) BMP-TFSI, (b) MPrP-TFSI and (c) EMI-TFSI (M, M' and M<sub>0</sub> denote melting peaks).

After adding water, the melting peaks for the bulk RTILs shift toward or remain at 0°C; this is attributed to a bound water effect. With water amounts exceeding 2.0-2.5 wt%, extra melting peaks (M<sub>0</sub>) with melting temperatures near 0°C are detected. These peaks are apparently related to the melting of free water, which is not linked to the RTILs. Therefore, in all the RTILs studied, water exists as either bound water or both bound and free water, depending on the water concentration. The portion of the bound water with smaller water-ion interactions (H-bonding) interferes with the strong ion-ion interaction of the RTILs in each water added RTIL, resulting in

the decreased viscosity and increased conductivity. The effect of water addition on the electrochemical behavior for Zn redox, focusing on the kinetic properties, is further explored and presented in the following section.

#### **4.3.2 Kinetic properties and reversibility for Zn redox reactions**

The EW for each RTIL with different concentrations of water was first examined prior to the Zn redox behavior investigation. As displayed in Fig. 4-4, increased water addition leads to a decrease in the EW. A balance between the reduction in EW and the improvement in conductivity, as well as an unaffected Zn redox reaction in the shortened EW, must be maintained. It was found that if the maximum amount of water was controlled to 2.0 wt% in BMP-TFSI and 2.5 wt% in MPrP-TFSI and EMI-TFSI, the Zn redox reactions were unaffected (Fig. 4-5). Moreover, adding water to the three RTILs kinetically facilitated the Zn redox reaction. An increase of 3-6 times in the exchange current density ( $j_0$ ) for the Zn redox reaction and an increase of 2-3.5 times in the diffusion coefficient ( $D_0$ ) for the Zn species were observed for all three RTILs, as shown in Fig. 4-6 and Table 4-1. This suggests that enhanced mass transfer and reaction rate were achieved by adding water to each RTIL. The increased exchange current density led to a smaller surface overpotential ( $\eta_s$ ) required to activate the redox reaction. Likely, the enhanced diffusion coefficient of the Zn species led to a lower concentration overpotential ( $\eta_T$ ). In addition, the improved conductivity with water addition minimized the ohmic drop in the electrolyte. As a result, the total overpotential  $\eta$  (where  $\eta = \eta_s + \eta_T + \text{ohmic drop}$ ) for driving the Zn redox reaction, as indicated by peak potential separation  $\Delta E_p$  between the Zn reduction and Zn oxidation reactions (shown in Table 4-1), was reduced to around 0.5 V for the three RTILs added with water.

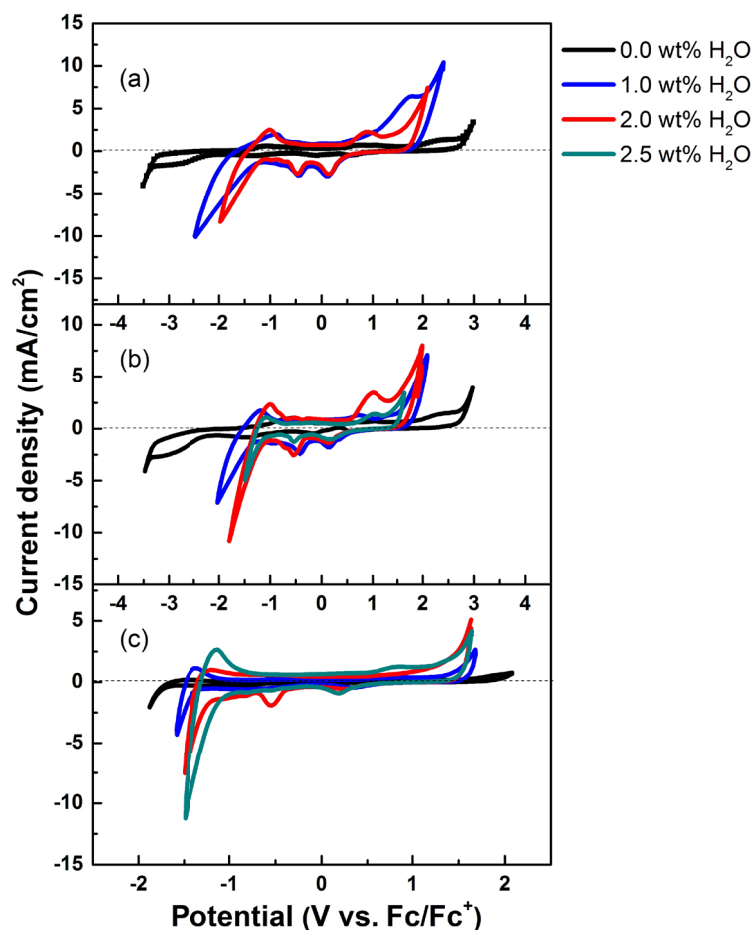


Fig. 4-4 CV results for the electrochemical window in: (a) BMP-TFSI, (b) MPrP-TFSI and (c) EMI-TFSI.

DFT calculations on cluster models composed of  $\text{BMP}^+$ ,  $\text{TFSI}^-$ ,  $\text{H}_2\text{O}$  and  $\text{Zn}^{2+}$  species served as an effective way to understand the interactions among the ions and gave insights into the mechanism(s) for the improved Zn redox kinetics with water addition. Table 4-2 shows the binding energies for the various gas-phase reactions that were investigated. The reactions are labeled “a” to “m” in the first column and the optimized geometries of the products for these reactions are shown in Fig. 4-7 a-l. The bond lengths are given in Angstroms ( $\text{\AA}$ ), and the Mulliken charges (atoms with hydrogen summed) are italicized and start with a ‘+’ or ‘-’ sign. The binding energies of reaction schemes a-i were calculated to give a baseline for understanding the effect of water molecules on the Zn-TFSI species, which are covered in reactions j-m. The interactions among the ions present in the electrolyte are classified into three groups. Firstly, there are water molecules interacting with  $\text{Zn}^{2+}$  ions (reactions a-d). The binding energy of  $\text{H}_2\text{O}$  to  $\text{Zn}^{2+}$ , in the absence of other species, is somewhere between 4.38 and 2.30 eV depending on

the level of hydration of the central Zn cation. The results are similar to those obtained by Pavlov et al. [142]. The binding for the first two water molecules is stronger than the subsequent ones. As seen in Fig. 4-7 a-d, the central Zn charge decreases with water addition, indicating that electron density is transferred from H<sub>2</sub>O to the central Zn as water bonds. Secondly, there are water molecules interacting with ionic liquid species (reactions e-f). Fig. 4-7 e-f shows that the partially negative oxygen atom of water is facing BMP<sup>+</sup>, while the partially positive hydrogen atoms of water are facing TFSI<sup>-</sup>. Their binding energies are the weakest and should be classified as ion-dipole interaction rather than chemical bonding. Thirdly, there are TFSI<sup>-</sup> anions interacting with other ions in the absence of water molecules (reactions g-i). As expected, the interaction of Zn<sup>2+</sup> with TFSI<sup>-</sup> is the strongest because of Zn's large 2<sup>+</sup> charge. This is followed by the interaction strength of Zn(TFSI)<sup>+</sup> with TFSI<sup>-</sup>. The relative weakness of the BMP<sup>+</sup>-TFSI<sup>-</sup> interaction (reaction g) can be attributed to the distribution of the cationic charge over a large surface.

Reactions j-l in Table 4-2 show that the interaction of water with Zn(TFSI)<sub>2</sub> is more energetically favored than that with BMP<sup>+</sup> (reaction e) or TFSI<sup>-</sup> (reaction f). This indicates that water will preferentially bind to Zn<sup>2+</sup> when added to a mixture of Zn(TFSI)<sub>2</sub> in BMP-TFSI. Furthermore, from Fig. 4-7 i-k, it can be seen that the distance between Zn and the TFSI O-atoms increases with water addition. This suggests that water weakens the ionic interaction between Zn<sup>2+</sup> and TFSI<sup>-</sup>. Due to computational limitations, only three water molecules could be added in the Zn(TFSI)<sub>2</sub> model. However, by comparing reaction m to reaction i, it is demonstrated that adding two molecules of water weakens the Zn(TFSI)<sup>+</sup>···TFSI<sup>-</sup> binding energy considerably from 6.96 to 4.71 eV. This could facilitate the dissolution of Zn<sup>2+</sup> in BMP-TFSI, which in turn can increase the concentration of Zn<sup>2+</sup> involved in the redox reaction and improve the overall Zn redox reaction rates.

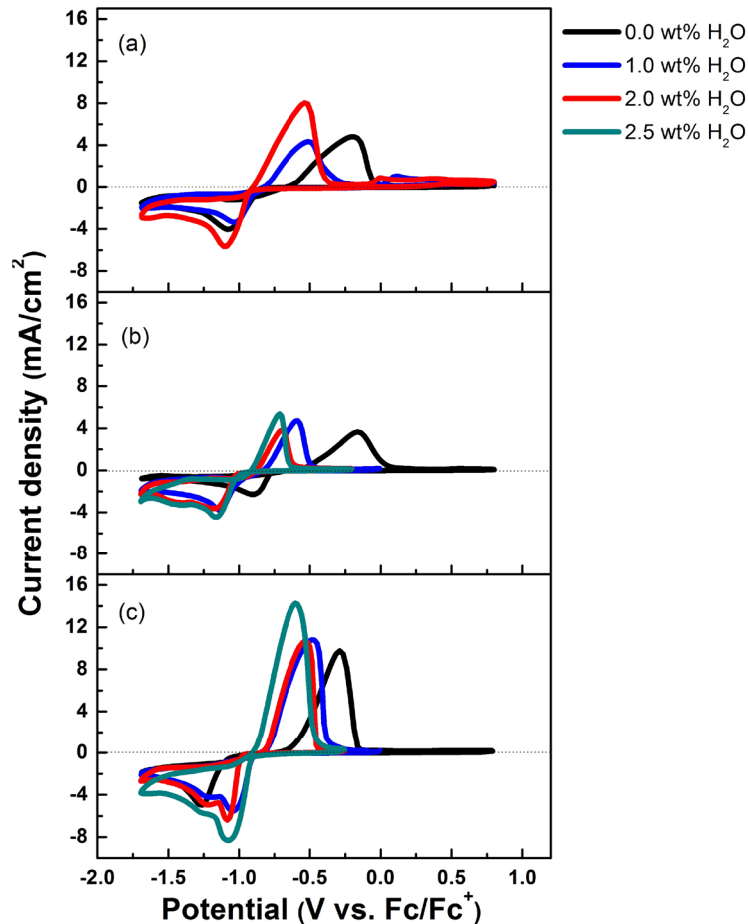


Fig. 4-5 CV results for Zn redox in: (a) BMP-TFSI, (b) MPrP-TFSI and (c) EMI-TFSI.

The incorporation of water, however, had a negative influence on the reversibility of Zn redox in the three RTILs. As shown in Table 4-3, the  $Q_a/Q_c$  ratio ( $Q_a$  is the charge integrated for Zn oxidation;  $Q_c$  is the charge integrated for Zn reduction) was adopted to evaluate reversibility. The closer  $Q_a/Q_c$  is to 1 (where the charge for reducing  $Zn^{2+}$  is equal to that for oxidizing Zn), the more reversible is Zn redox. The  $Q_a/Q_c$  is significantly less than 1 after adding water in the RTILs, especially for BMP-TFSI and MPrP-TFSI, which indicates poorer Zn reversibility. With regard to secondary battery applications, the present study suggests that electrolytes using water diluted RTILs can be beneficial for improving the energy and power density due to the enhanced Zn kinetic properties, but would harm the battery service life as reflected by the worse Zn reversibility.

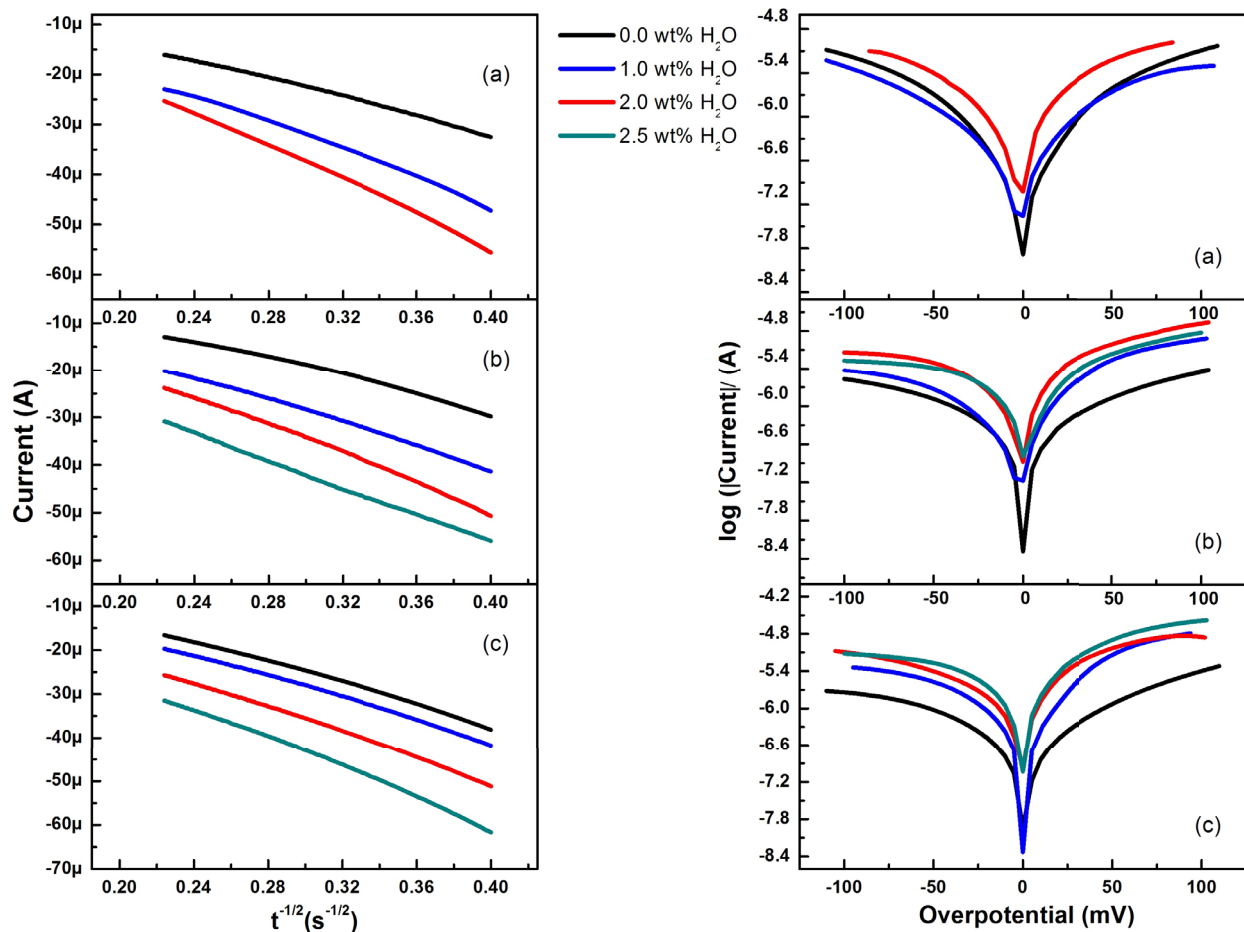


Fig. 4-6 Current vs. time curves (left) and Tafel plots (right) for Zn redox in each RTIL with water additions: (a) BMP-TFSI, (b) MPrP-TFSI and (c) EMI-TFSI.

Table 4-1 Kinetic properties for Zn redox in three RTILs with TFSI<sup>-</sup> anions

		Water concentration	0.0	1.0	2.0	2.5
		(wt%)				
$\Delta E_p$ (V)	BMP-TFSI		0.90	0.52	0.57	/
	MPrP-TFSI		0.75	0.58	0.48	0.46
	EMI-TFSI		0.97	0.56	0.55	0.48
$D_0$ ( $\times 10^{-7}$ cm <sup>2</sup> /s)	BMP-TFSI		2.2	3.8	7.6	/
	MPrP-TFSI		1.8	3.0	4.6	4.3
	EMI-TFSI		2.9	3.1	4.2	5.8
$j_0$ (mA/cm <sup>2</sup> )	BMP-TFSI		0.018	0.017	0.056	/
	MPrP-TFSI		0.018	0.026	0.049	0.040
	EMI-TFSI		0.021	0.055	0.079	0.13

Table 4-2 Gas-phase binding energies between  $\text{BMP}^+$ ,  $\text{TFSI}^-$  and  $\text{Zn}^{2+}$  and  $\text{H}_2\text{O}$  species determined by B3LYP/6-311G(df,p) DFT calculations

Scheme	Reactants		Product	Binding Energy, eV
a	$\text{Zn}^{2+} + \text{H}_2\text{O}$	$\rightarrow$	$\text{Zn}(\text{H}_2\text{O})^{2+}$	4.38
b	$\text{Zn}(\text{H}_2\text{O})^{2+} + \text{H}_2\text{O}$	$\rightarrow$	$\text{Zn}(\text{H}_2\text{O})_2^{2+}$	3.72
c	$\text{Zn}^{2+} + 6 \text{H}_2\text{O}$	$\rightarrow$	$\text{Zn}(\text{H}_2\text{O})_6^{2+}$	13.84 (2.30/ $\text{H}_2\text{O}$ molecule)
d	$\text{Zn}^{2+} + 6 \text{H}_2\text{O}$	$\rightarrow$	$\text{Zn}(\text{H}_2\text{O})_6^{2+}$ , PCM <sup>a</sup>	21.61 (3.60/ $\text{H}_2\text{O}$ molecule)
e	$\text{BMP}^+ + \text{H}_2\text{O}$	$\rightarrow$	$\text{BMP}^+ \cdot \text{H}_2\text{O}$	0.20
f	$\text{TFSI}^- + \text{H}_2\text{O}$	$\rightarrow$	$\text{TFSI}^- \cdot \text{H}_2\text{O}$	0.33
g	$\text{BMP}^+ + \text{TFSI}^-$	$\rightarrow$	$\text{BMP}^+ \cdot \text{TFSI}^-$	2.92
h	$\text{Zn}^{2+} + \text{TFSI}^-$	$\rightarrow$	$\text{Zn}(\text{TFSI})^+$	15.94
i	$\text{Zn}(\text{TFSI})^+ + \text{TFSI}^-$	$\rightarrow$	$\text{Zn}(\text{TFSI})_2$	6.96
j	$\text{Zn}(\text{TFSI})_2 + \text{H}_2\text{O}$	$\rightarrow$	$\text{Zn}(\text{TFSI})_2(\text{H}_2\text{O})$	0.46
k	$\text{Zn}(\text{TFSI})_2(\text{H}_2\text{O}) + \text{H}_2\text{O}$	$\rightarrow$	$\text{Zn}(\text{TFSI})_2(\text{H}_2\text{O})_2$	0.43
l	$\text{Zn}(\text{TFSI})_2(\text{H}_2\text{O})_2 + \text{H}_2\text{O}$	$\rightarrow$	$\text{Zn}(\text{TFSI})_2(\text{H}_2\text{O})_2 \cdots \text{OH}_2$	0.36
m	$\text{Zn}(\text{TFSI})(\text{H}_2\text{O})_2^+ + \text{TFSI}^-$	$\rightarrow$	$\text{Zn}(\text{TFSI})_2(\text{H}_2\text{O})_2$	4.71

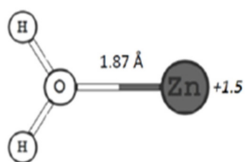
<sup>a</sup> Polarizable continuum model is used to approximate the effect of additional layers of water molecules surrounding the  $\text{Zn}(\text{H}_2\text{O})_6^{2+}$  cluster.

Table 4-3 Charge integrated for Zn redox in three RTILs with  $\text{TFSI}^-$  anions before and after water addition

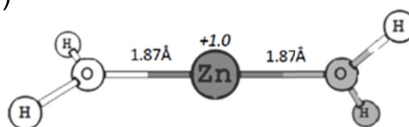
RTILs	0.0 wt% water			2.0-2.5 wt% water		
	$Q_c$	$Q_a$	$Q_a/Q_c$	$Q_c$	$Q_a$	$Q_a/Q_c$
BMP-TFSI	452	386	0.85	970	355	0.37
MPrP-TFSI	482	443	0.92	887	263	0.30
EMI-TFSI	540	545	1.01	1100	738	0.67

Note:  $Q_c$  and  $Q_a$  are calculated according to the CV curves shown in Fig. 4-5.

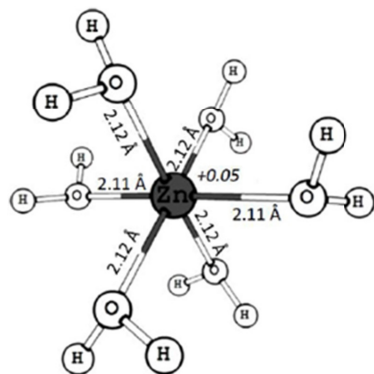
(a)



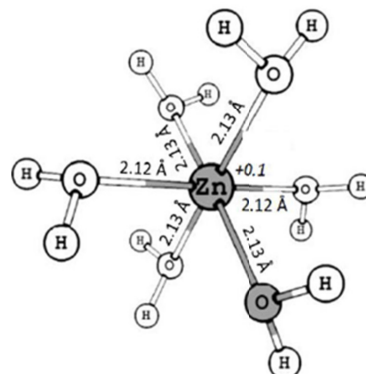
(b)



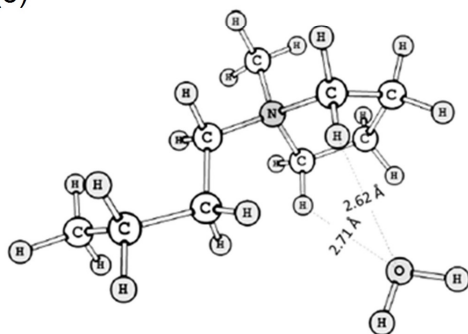
(c)



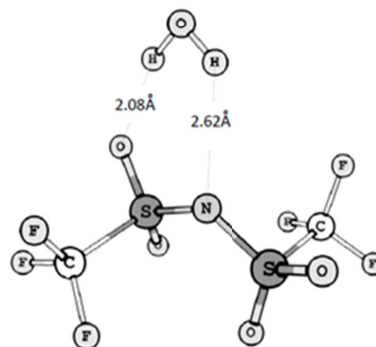
(d)



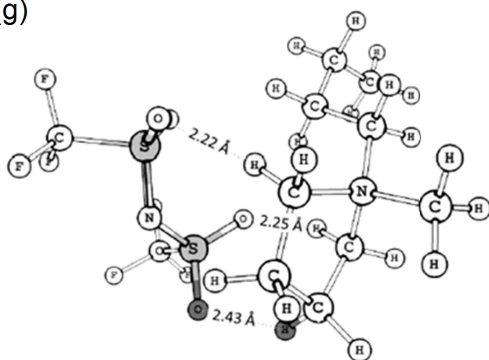
(e)



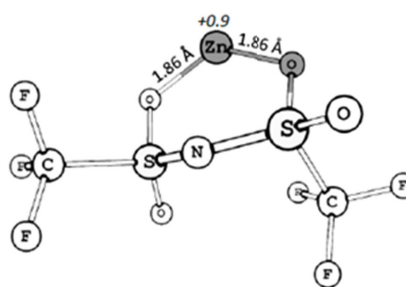
(f)



(g)



(h)



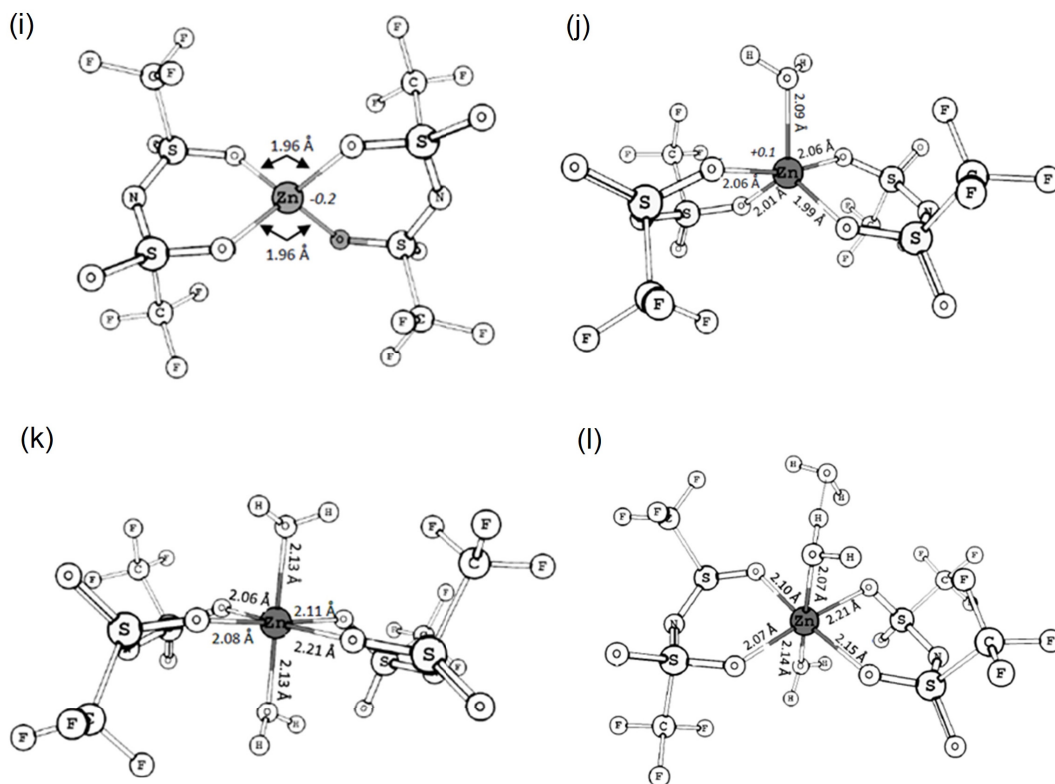


Fig. 4-7 B3LYP/6-311+G(2d,2p) optimized geometric structures for: (a)  $\text{Zn}(\text{H}_2\text{O})_2^{2+}$ , (b)  $\text{Zn}(\text{H}_2\text{O})_2^{2+}$ , (c)  $\text{Zn}(\text{H}_2\text{O})_6^{2+}$  and (d)  $\text{Zn}(\text{H}_2\text{O})_6^{2+}$  with the Polarizable Continuum Model used to approximate the effect of additional layers of water molecules; (e)  $\text{BMP}^+-\text{H}_2\text{O}$ , (f)  $\text{TFSI}^--\text{H}_2\text{O}$ , (g)  $\text{BMP}^+-\text{TFSI}^-$ , (h)  $\text{Zn}(\text{TFSI})^+$ , (i)  $\text{Zn}(\text{TFSI})_2$ , (j)  $\text{Zn}(\text{TFSI})_2(\text{H}_2\text{O})$ , (k)  $\text{Zn}(\text{TFSI})_2(\text{H}_2\text{O})_2$  and (l)  $\text{Zn}(\text{TFSI})_2(\text{H}_2\text{O})_2 \cdots \text{OH}_2$ .

### 4.3.3 Zn deposit morphology in studied RTILs without or with water addition

RTILs possess the capability of modifying metal deposits and it is of importance to study the influence of water addition on the morphology of Zn electrodeposited from the three RTILs. Fig. 4-8 a-c exhibits the morphology of Zn deposited from each RTIL with no water addition. It is noteworthy that no Zn dendrites were present. In BMP-TFSI and MPrP-TFSI, Zn deposits have similar morphology, i.e., clustered needle-like, nanometer size Zn, with the size of the Zn deposits slightly finer in BMP-TFSI than in MPrP-TFSI. The  $\text{BMP}^+$  cation has been reported to adsorb on the surface of the growing nuclei, leading to fine grain size/nanocrystalline deposits [4, 143]. It is speculated that the  $\text{MPrP}^+$  cation also possesses the same adsorption function, while the longer alkyl chain in  $\text{BMP}^+$  relative to  $\text{MPrP}^+$  (butyl group vs. propyl group) turns out to be more effective in terms of inhibiting Zn growth during electrodeposition. Unlike BMP-TFSI and MPrP-TFSI, faceted and well-crystallized Zn deposits with a coarser size (micrometer range)

were formed from EMI-TFSI. It is clear that altering the cation can significantly change the morphology of Zn deposits and the interaction of cations with the substrate may account for the change. A similar study [144], dealing with the electrodeposition of nanocrystalline Al in BMP-TFSI and microcrystalline Al in EMI-TFSI on a Au substrate, demonstrated that IL solvation layers formed at the substrate/IL interface affected the electrodeposition process and the size of Al deposits. The BMP<sup>+</sup> cation was about 4 times more strongly adsorbed on the Au substrate than the EMI<sup>+</sup> cation, which hindered underpotential deposition of Al and slowed down nuclei growth.

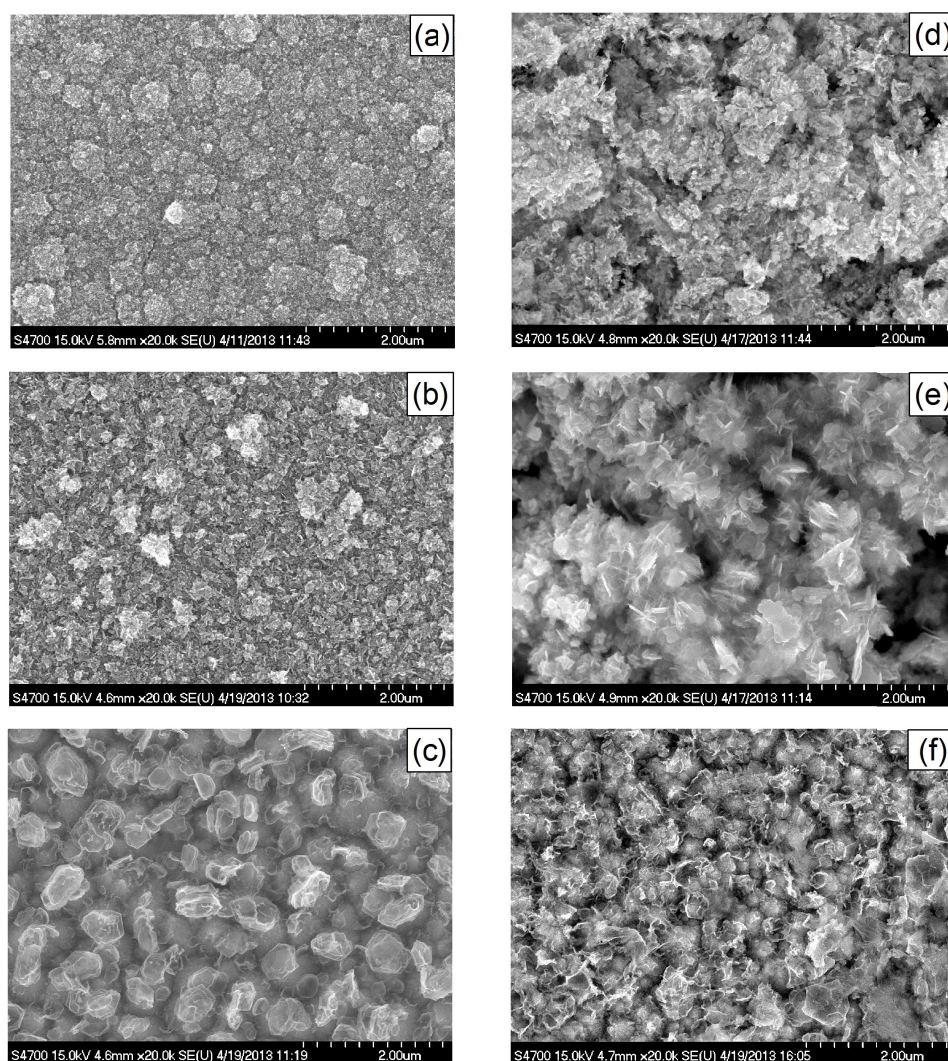


Fig. 4-8 SEM SE images of Zn deposits prepared by potentiostatic deposition from: (a) BMP-TFSI, (b) MPrP-TFSI, (c) EMI-TFSI, (d) BMP-TFSI with 2.0 wt% H<sub>2</sub>O, (e) MPrP-TFSI with 2.0 wt% H<sub>2</sub>O and (f) EMI-TFSI with 2.5 wt% H<sub>2</sub>O.

The morphology of Zn deposits in water added RTILs is displayed in Fig. 4-8 d-f. The water amounts were 2.0 wt% in BMP-TFSI and MPrP-TFSI and 2.5 wt% in EMI-TFSI, i.e., the electrolyte systems where the best kinetic properties for Zn redox were achieved. Larger scale Zn deposits were observed in both BMP-TFSI and MPrP-TFSI after adding water. This is most likely because of the increased mass transfer rate for the Zn species in the water added ILs, which facilitated deposit growth. Moreover, Zn deposits were not as compact as those in the two RTILs with no water addition and easily delaminated from the substrate. This result indicates that a reduced amount of the Zn material would be involved in subsequent electrochemical reactions, leading to decreased charge upon cycling. On the other hand, in EMI-TFSI with 2.5 wt% H<sub>2</sub>O, Zn deposits changed from faceted to granular in shape without a significant change in size and good adhesion of Zn deposits to the substrate was maintained. Therefore, Zn electrodeposited from the RTIL with imidazolium cations appeared to be less affected by water additions than Zn obtained from RTILs with pyrrolidinium cations. These results also explain the better Zn redox reversibility observed in EMI-TFSI than that in BMP-TFSI and MPrP-TFSI after adding water.

#### 4.4 Summary

Water in different concentrations (0-5.0 wt%) was added as a diluent to three RTILs with TFSI anions, i.e., BMP-TFSI, MPrP-TFSI and EMI-TFSI, with the purpose of increasing their conductivity. The influence of water addition on conductivity, Zn redox kinetics, reversibility and Zn deposit morphology, together with the corresponding mechanisms was studied and discussed.

(1) Increased conductivity upon water addition (4.5-14 mS/cm): FTIR and DSC results suggest the presence of water-ion interactions through H-bonding after adding water to the RTILs. The water-ion interaction perturbed the ion-ion association of the RTILs and facilitated the dissociation of cation-anion pairs, leading to decreased viscosity and increased conductivity.

(2) Improved Zn redox kinetics upon water addition: DFT cluster calculations for the BMP-TFSI system showed that interactions of water with the Zn<sup>2+</sup> species are stronger than those with BMP<sup>+</sup> and TFSI. These results indicated that water addition can weaken Zn-TFSI bonds and enhance the dissolution of Zn<sup>2+</sup> in RTILs, which in turn increased the concentration of Zn<sup>2+</sup>

involved in the redox reaction and improved the overall Zn redox reaction rate and diffusion rates.

(3) Deteriorated Zn redox reversibility and altered deposit morphology upon water addition: water modified the size and adhesion properties of dendrite-free Zn deposits in the three RTILs. Particularly in RTILs with pyrrolidinium cations, significant growth of Zn deposits and poorer adhesion associated with looser Zn morphology was observed, which also accounted for the poorer Zn redox reversibility exhibited in the diluted solutions. This indicated that increased mass transport of Zn species with water addition is beneficial for kinetic performance, but could be detrimental in terms of Zn deposit properties and Zn redox reversibility.

## **Chapter 5 Electrolytes composed of water and dimethyl sulfoxide added RTILs with DCA<sup>-</sup> anions**

### **5.1 Overview**

As indicated from Chapter 3, in addition to the RTILs with TFSI<sup>-</sup> anions, EMI-DCA is predicted to be a promising electrolyte candidate for Zn anode rechargeable batteries. Firstly, the Zn redox reaction exhibits a high current density in RTILs with EMI<sup>+</sup> cations and desirable Zn redox reversibility and cyclability is observed in RTILs with DCA<sup>-</sup> anions, suggesting that desirable Zn redox behavior could be achieved in EMI-DCA. Secondly, the hydrophilic EMI-DCA possesses superior conductivity (~25 mS/cm), which is even higher than those for the hydrophobic RTILs with TFSI<sup>-</sup> anions modified with water as a diluent. Therefore, the purpose of this Chapter is to explore an electrolyte system based on EMI-DCA that is potentially applicable for Zn anode rechargeable batteries. Water and dimethyl sulfoxide (DMSO) are added to modify EMI-DCA, with the purpose of optimizing the electrochemical system for the benefit of Zn redox behavior. Compared with water, DMSO has a slightly higher viscosity but a lower vapor pressure [145], so as a diluent for RTILs it may be able to increase their conductivity while maintaining low volatility. As a polar solvent, DMSO also facilitates the solvation of Zn ions [146]. All these features make DMSO a potentially good additive in RTILs for Zn anode battery applications.

In this Chapter, the effects of water and/or DMSO addition on the kinetics, reversibility and cyclability of Zn redox behavior in EMI-DCA are explored, as part of the investigation on the electrode reaction mechanisms upon diluent addition. The morphology of Zn deposits obtained from EMI-DCA with diluents is studied as well. Finally, an electrolyte system composed of both water and DMSO diluents with optimized Zn redox performance is proposed.

### **5.2 Experimental methods**

EMI-DCA (C<sub>8</sub>H<sub>11</sub>N<sub>5</sub>, >98 wt%, with <0.2 wt% H<sub>2</sub>O and <1.5 wt% halides) was purchased from IoLiTec and Zn-TFSI (99 wt%) was purchased from Solvionic. The chemicals were used as received without further treatment. Electrolytes were prepared by first vacuum drying EMI-DCA at ~90°C overnight and then diluting it with DI water (18.2 MΩ•cm) and/or DMSO (100 wt%, Fisher Scientific). Zn-TFSI was dissolved in each electrolyte by stirring overnight to produce a 0.1 mol/L Zn<sup>2+</sup> solution for electrochemical measurements.

### 5.2.1 Conductivity measurements

Conductivity measurements were the same as that stated in Chapter 4. Six groups of electrolytes were tested: 1) E: EMI-DCA; 2) W<sub>1</sub>: EMI-DCA + 10 wt% H<sub>2</sub>O (mole ratio: 1:1.1); 3) W<sub>2</sub>: EMI-DCA + 40 wt% H<sub>2</sub>O (mole ratio: 1:6.6); 4) D: EMI-DCA + 50 wt% DMSO (mole ratio: 1:2.3); 5) D/W<sub>1</sub>: EMI-DCA + 5 wt% H<sub>2</sub>O + 48 wt% DMSO (mole ratio: 1:1.1:2.3) and 6) D/W<sub>2</sub>: EMI-DCA + 25 wt% H<sub>2</sub>O + 38 wt% DMSO (mole ratio: 1:6.6:2.3). Mole ratio is used for describing the electrolyte composition in the following text.

### 5.2.2 Electrochemical measurements

A Zahner IM6 electrochemical workstation (controlled by Thales 4.15 software) and a BASi system (Bioanalytical Systems, Inc.) were applied to perform electrochemical tests. CV scans at 50 mV/s were undertaken within the range of -1.7 to -0.4 V and -1.85 to 2.0 V vs. Fc/Fc<sup>+</sup> for studying Zn redox reactions and the electrochemical window of each electrolyte, respectively. Two hundred cycles were also applied in CV tests at 10 mV/s to explore Zn redox cyclability. Chronoamperometry experiments were accomplished by stepping the potential of the working electrode from open circuit potential to -1.5 to -1.7 V vs. Fc/Fc<sup>+</sup>, where the reduction of the Zn species is a diffusion-controlled process. Potentiodynamic polarization experiments were performed at 1.0 mV/s. All electrochemical experiments used a 3-electrode cell configuration, consisting of a Pt (1.6 mm diameter, MF-2013 BASi) WE, a Pt wire (0.5 mm diameter, MW-1032 BASi) CE and an RE, which was assembled with a Pt wire inserted in a glass tube filled with EMI-DCA containing 50:50 mol% Fc/Fc<sup>+</sup> as the internal potential standard with the addition of water at the same concentration as that of studied electrolytes. The inner solution of the RE was separated from the studied electrolyte by a porous Vycor tip (MF-2042 BASi). During test, the electrolyte was first purged with nitrogen gas for 10 min and then blanketed with nitrogen gas during testing.

### 5.2.3 SEM and XRD observations

A 3-electrode cell configuration was applied to study the Zn deposit morphology, with the same RE used for the electrochemical measurements, a Pt coated Si substrate as the WE and a Zn plate as the CE placed vertically within 20 mm from the WE. First, the morphology and composition of deposits after a 200 cycle CV test were investigated, shedding some light on the products of electrode reactions. After CV cycling, the substrate was thoroughly rinsed with acetone and

ethanol and then dried in air. Second, in order to reveal the effect of diluents on Zn deposit morphology obtained from EMI-DCA, Zn coatings were electrodeposited at a constant potential (the peak cathodic potential based on the CV curves for Zn redox reactions) on Pt coated Si substrates for 1 hr. The morphology of the deposits was analyzed with a Hitachi S-4700 SEM operated at 15 kV. Low voltage (0.8-1.0 kV) secondary electron imaging was also applied to distinguish Zn from the oxidation product ZnO, which may be present in deposited films after cycling. The phases present in the deposited films after cycling were confirmed through X-ray diffraction (XRD) analysis, using a Bruker D8 X-ray diffractometer. The diffractometer was operated in thin film mode with the incident beam at a glancing angle of  $0.5^\circ$  to the sample surface, in order to minimize the XRD signal from the substrate.

### 5.3 Results and discussion

#### 5.3.1 Conductivities of water and/or DMSO added EMI-DCA electrolytes

As seen in Fig. 5-1, the electrolyte conductivity for EMI-DCA with water and/or DMSO additions is improved. A mole ratio of EMI-DCA to water of 1:6.6 and EMI-DCA to DMSO of 1:2.3 correspond to the highest measured electrolyte conductivities of  $\sim 70$  mS/cm and  $\sim 30$  mS/cm, respectively. EMI-DCA with water at a mole ratio of 1:1.1 has a conductivity of  $\sim 50$  mS/cm (twice the EMI-DCA value). It is apparent that adding water is more effective than adding DMSO to EMI-DCA in terms of improving the electrolyte conductivity.

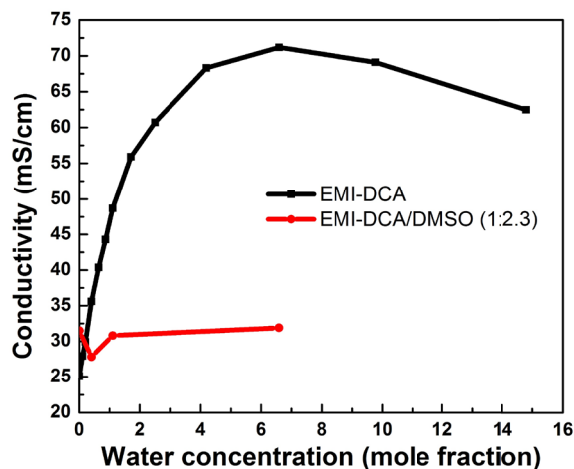
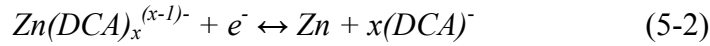


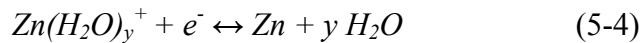
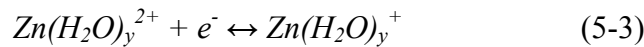
Fig. 5-1 Conductivity of EMI-DCA with addition of water and/or DMSO.

### 5.3.2 Mechanisms for Zn redox reactions in EMI-DCA with water and DMSO

Typical CV curves for Zn redox in the studied electrolytes are compared in Fig. 5-2. For the electrolytes with no water (Fig. 5-2 a and d), two reduction peaks are notable in the CV curves, indicating that Zn ions are reduced to Zn in two steps via receiving one electron per step. This is attributed to the complexing ability of DCA<sup>-</sup> anions towards Zn ions to form complex ions, Zn(DCA)<sub>x</sub><sup>(x-2)-</sup>. Potentials for the first and second reduction step range from -1.3 to -1.35 V and -1.5 to -1.55 V, respectively. The corresponding electrode reactions during reduction are proposed as follows:



The same reaction mechanism has been discussed in Chapter 3 for Zn redox in BMP-DCA, an ionic liquid with the same anion. In electrolytes with water added (Fig. 5-2 b-c and e-f), Zn ions are likely to coordinate with either H<sub>2</sub>O or DCA<sup>-</sup> anions to form both Zn(H<sub>2</sub>O)<sub>y</sub><sup>2+</sup> and Zn(DCA)<sub>x</sub><sup>(x-2)-</sup> complex ions. Compared with Zn(DCA)<sub>x</sub><sup>(x-2)-</sup>, Zn(H<sub>2</sub>O)<sub>y</sub><sup>2+</sup> ions are smaller in size and diffuse more easily. As seen in Table 5-1, the diffusion coefficient for the Zn species increases with water concentration, reflecting the increased ratio of Zn(H<sub>2</sub>O)<sub>y</sub><sup>2+</sup> to Zn(DCA)<sub>x</sub><sup>(x-2)-</sup> ions. It is also notable that in EMI-DCA + H<sub>2</sub>O (1:6.6) and EMI-DCA + H<sub>2</sub>O + DMSO (1:6.6:2.3), the diffusion coefficients are one order of magnitude higher than the other electrolytes. This implies that Zn(H<sub>2</sub>O)<sub>y</sub><sup>2+</sup> ions are present in a high concentration in the complex ions and compete with Zn(DCA)<sub>x</sub><sup>(x-2)-</sup> ions for involvement in the reduction reactions. Consequently, in addition to reactions (5-1) and (5-2), reactions (5-3) and (5-4) can also take place and even prevail as the positive Zn(H<sub>2</sub>O)<sub>y</sub><sup>2+</sup> ions are more readily attracted to the electrode surface with excess electrons than Zn(DCA)<sub>x</sub><sup>(x-2)-</sup> ions with negative charge:



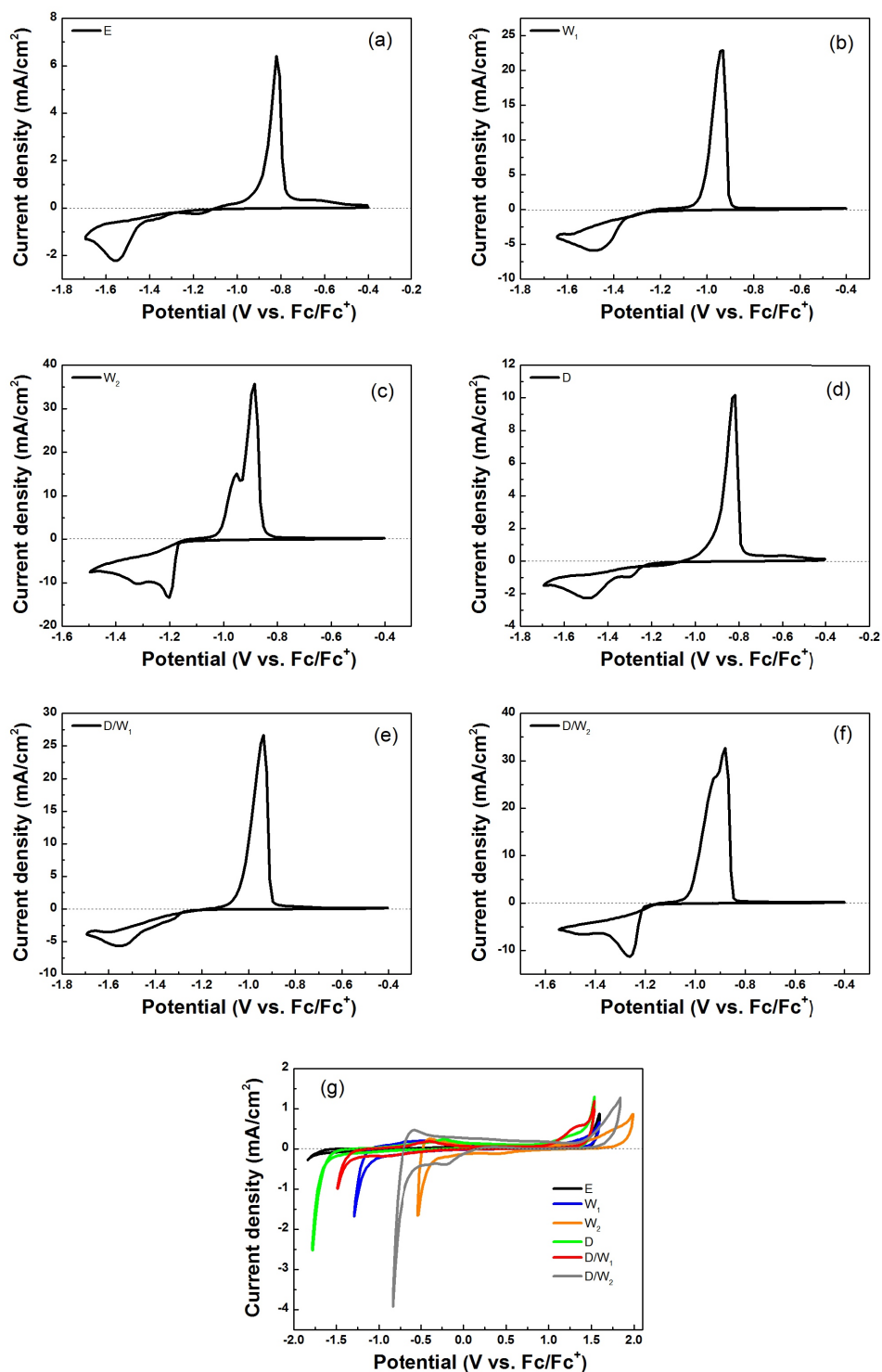


Fig. 5-2 CV plots at 50 mV/s for Zn redox in EMI-DCA based electrolytes: (a) E: EMI-DCA, (b) W<sub>1</sub>: EMI-DCA + H<sub>2</sub>O (1:1.1), (c) W<sub>2</sub>: EMI-DCA + H<sub>2</sub>O (1:6.6), (d) D: EMI-DCA + DMSO (1:2.3), (e) D/W<sub>1</sub>: EMI-DCA + H<sub>2</sub>O + DMSO (1:1.1:2.3), (f) D/W<sub>2</sub>: EMI-DCA + H<sub>2</sub>O + DMSO (1:6.6:2.3) and (g) electrochemical window for each electrolyte in the absence of Zn ions.

As can be seen in Fig. 5-2 c and f, the resultant peak potentials for Zn reduction in EMI-DCA + H<sub>2</sub>O (1:6.6) and EMI-DCA + H<sub>2</sub>O + DMSO (1:6.6:2.3) shift to more positive positions, i.e., -1.2 to -1.25 V and -1.35 to -1.45 V, compared with the potentials in EMI-DCA without or with DMSO addition only (Fig. 5-2 a and d). For electrolytes EMI-DCA + H<sub>2</sub>O (1:1.1) and EMI-DCA + H<sub>2</sub>O + DMSO (1:1.1:2.3), with relatively small amounts of water, Zn(DCA)<sub>x</sub><sup>(x-2)-</sup> remains as the dominant complexing ion involved into the electrode reactions, with the peak reduction potentials being similar to those observed for EMI-DCA without or with DMSO addition only. It is worth noting that a higher overpotential is required for Zn deposition in ionic liquids compared with traditional zincate aqueous electrolytes. In the latter case, Zn reduction is coupled with hydrogen evolution [147]. The adsorbed hydrogen atoms react with the Zn species, yielding a low overpotential for Zn deposition [148].

Table 5-1 Electrochemical behavior of Zn redox in EMI-DCA based electrolytes

Electrolyte	$\Delta E_p$ (V)	$D_0$ ( $\times 10^{-6}$ cm <sup>2</sup> /s)	$j_0$ (mA/cm <sup>2</sup> )	$Q_a/Q_c$ at CV cycle 2	$Q_a/Q_c$ at CV cycle 200
E	0.73	0.10	0.0016	0.84	0.85
W <sub>1</sub>	0.58	0.90	0.014	0.62	0.11
W <sub>2</sub>	0.36	6.00	0.12	0.59	0.07
D	0.67	0.30	0.0089	0.89	0.80
D/W <sub>1</sub>	0.57	0.80	0.032	0.91	0.89
D/W <sub>2</sub>	0.41	8.80	0.13	0.84	0.15

E: EMI-DCA; W<sub>1</sub>: EMI-DCA + H<sub>2</sub>O (1:1.1); W<sub>2</sub>: EMI-DCA + H<sub>2</sub>O (1:6.6); D: EMI-DCA + DMSO (1:2.3); D/W<sub>1</sub>: EMI-DCA + H<sub>2</sub>O + DMSO (1:1.1:2.3); D/W<sub>2</sub>: EMI-DCA + H<sub>2</sub>O + DMSO (1:6.6:2.3).

As shown in Table 5-1, water plays a leading role in improving the Zn redox kinetics, including increasing the diffusion rate and the exchange current density, as well as decreasing the overpotential (peak potential separation). With regard to Zn redox reversibility, as evaluated by the  $Q_a/Q_c$  ratio, Zn redox exhibits superior reversibility in EMI-DCA with DMSO. Adding water only to EMI-DCA impairs Zn redox reversibility, while the addition of both water and DMSO maintains good reversibility. By examining the EW of each electrolyte (Fig. 5-2 g), it is found that adding DMSO has a negligible effect on the EW of EMI-DCA, but the EW can be severely reduced with the addition of water. The decomposition of water molecules may account for the

sharp increase in cathodic current density observed in Fig. 5-2 g at -1.3 V and -0.5 V in EMI-DCA + H<sub>2</sub>O (1:1.1) and EMI-DCA + H<sub>2</sub>O (1:6.6), respectively. DMSO seems to have the ability of stabilizing H<sub>2</sub>O molecules (probably through H-bonding), resulting in a slightly wider EW for EMI-DCA added with both water and DMSO than that with water as the only additive.

The cyclability of Zn redox was further examined and the evolution of the CV scans with cycle number is shown in Fig. 5-3. As expected, in electrolytes EMI-DCA, EMI-DCA + DMSO (1:2.3) and EMI-DCA + H<sub>2</sub>O + DMSO (1:1.1:2.3) (Fig. 5-3 a, d and e), Zn redox maintains good reversibility after 200 cycles as reflected by the high ratio of  $Q_a/Q_c$  (>0.8, Table 5-1) and shows negligible shift in potential, exhibiting desirable cyclability. On the other hand, Zn redox gradually loses its reversibility with cycle number and shows poor cyclability in the other three electrolytes with water addition. Particularly in EMI-DCA with water in a high concentration (Fig. 5-3 c and f), with cycling, the peak reduction potential shifts from about -1.2 to -1.25 V to more negative positions around -1.35 to -1.4 V. This is most likely because of decreasing amounts of  $Zn(H_2O)_y^{2+}$  ions being involved in the electrode reactions due to the decomposition of water molecules during cycling. It is also notable that the oxidation peaks in Fig. 5-3 b, c and f gradually disappear with cycling. Water decomposition produces OH<sup>-</sup> ions, which could further react with Zn<sup>2+</sup> ions and lead to the formation of ZnO. Therefore, the reduction peaks observed in Fig. 5-3 b, c and f could be due to the formation of ZnO, which hinders the reduction of Zn<sup>2+</sup> ions and leads to diminishing Zn oxidation peaks observed during the reverse scan. In order to confirm this hypothesis, the morphology of the deposits that remained on the substrate surface after cycling was examined and is presented in Fig. 5-4. From electrolytes EMI-DCA, EMI-DCA + DMSO (1:2.3) and EMI-DCA + H<sub>2</sub>O + DMSO (1:1.1:2.3) (Fig. 5-4 a, d and e), nanoscale Zn deposits (approximately hundreds of nanometers thick) are present on the substrate after the last CV cycle was concluded on the oxidation side. This kind of morphology demonstrates that Zn deposits which form during the reduction process are mostly oxidized/dissolved back into the electrolyte during the reverse scan. This is an indication of good reversibility and cyclability for Zn redox as predicted from the CV results. On the contrary, after 200 CV cycles, thicker deposits (on the micron scale) remain on the substrate from electrolytes EMI-DCA + H<sub>2</sub>O (1:1.1), EMI-DCA + H<sub>2</sub>O (1:6.6) and EMI-DCA + H<sub>2</sub>O + DMSO (1:6.6:2.3), indicating the poor reversibility for Zn redox reactions.

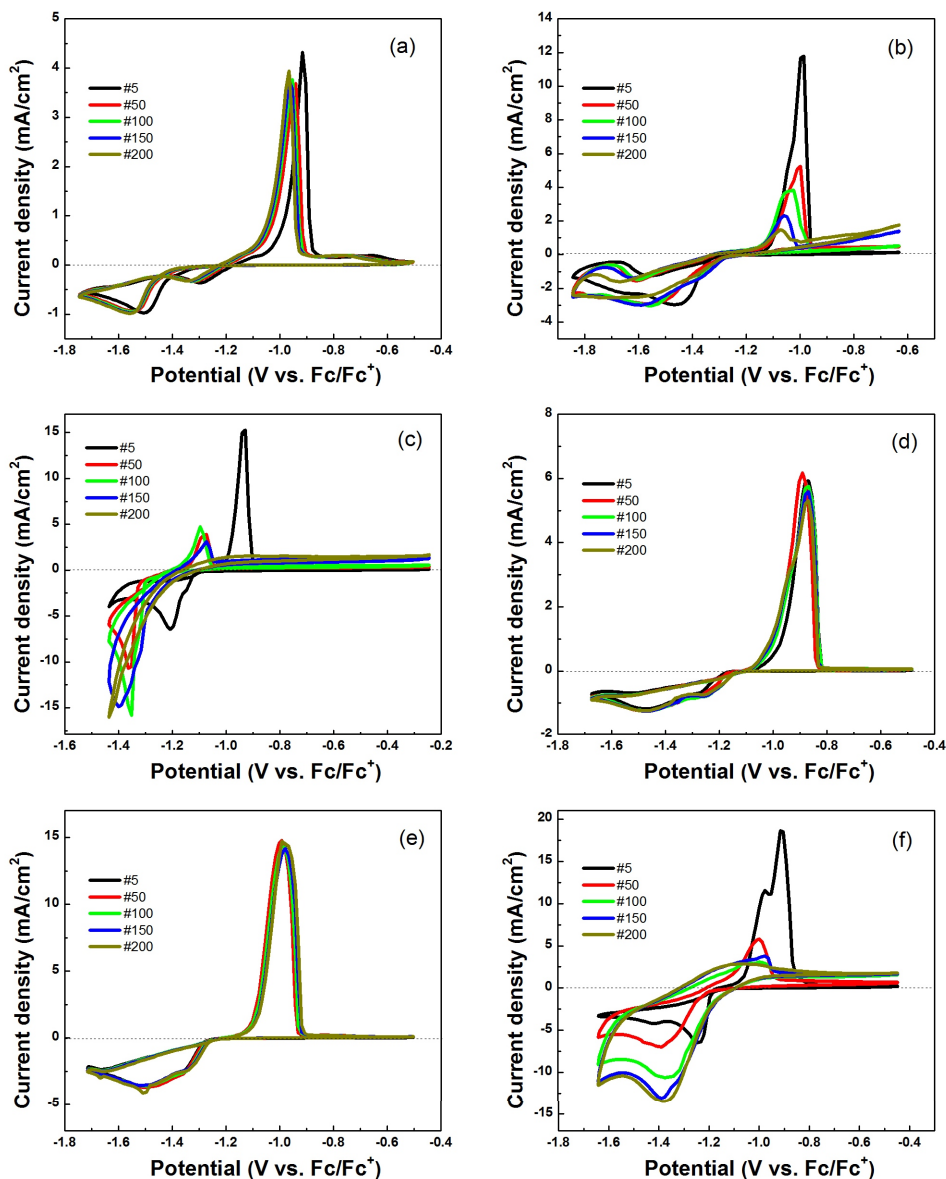


Fig. 5-3 Cyclability of Zn redox in EMI-DCA based electrolytes at 10 mV/s: (a) E: EMI-DCA, (b) W<sub>1</sub>: EMI-DCA + H<sub>2</sub>O (1:1.1), (c) W<sub>2</sub>: EMI-DCA + H<sub>2</sub>O (1:6.6), (d) D: EMI-DCA + DMSO (1:2.3), (e) D/W<sub>1</sub>: EMI-DCA + H<sub>2</sub>O + DMSO (1:1.1:2.3) and (f) D/W<sub>2</sub>: EMI-DCA + H<sub>2</sub>O + DMSO (1:6.6:2.3). (“#” denotes the cycle number.)

As seen in Fig. 5-4 b, c and f, observed deposits demonstrate porosity, suggesting the presence of ZnO. SEM images for these samples were taken at low accelerating voltages (0.8 kV) to reveal the contrast difference between Zn (brighter regions) and ZnO (darker regions); the images are shown as insets in Fig. 5-4 b, c and f. The SE yield for Zn increases significantly at lower voltages, while the SE yield for ZnO varies little with changing voltage, which produces the

contrast. The detailed contrast mechanism for distinguishing between ZnO and Zn is discussed in [149].

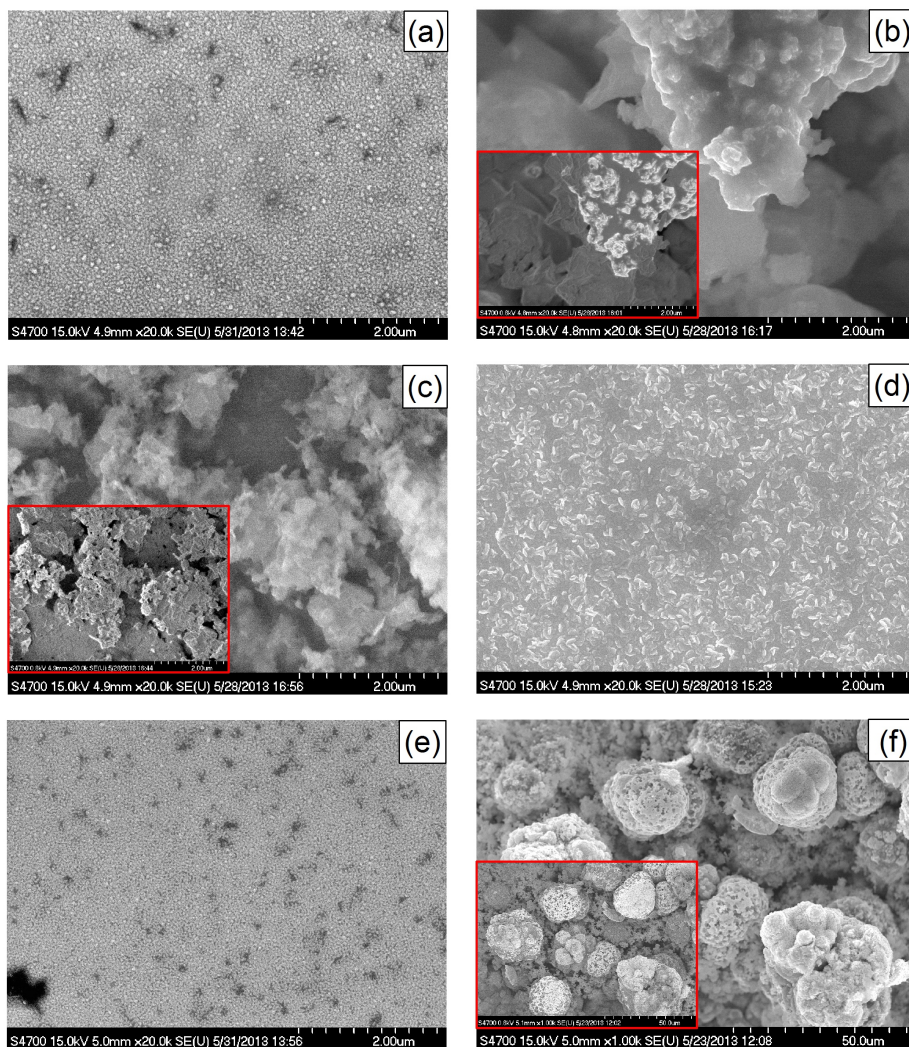


Fig. 5-4 SEM SE images of deposits on the substrate surface after cycling for 200 cycles in EMI-DCA based electrolytes: (a) E: EMI-DCA, (b)  $W_1$ : EMI-DCA +  $H_2O$  (1:1.1), (c)  $W_2$ : EMI-DCA +  $H_2O$  (1:6.6), (d) D: EMI-DCA + DMSO (1:2.3), (e)  $D/W_1$ : EMI-DCA +  $H_2O$  + DMSO (1:1.1:2.3) and (f)  $D/W_2$ : EMI-DCA +  $H_2O$  + DMSO (1:6.6:2.3). Inset images in b, c and f are taken at the same location with a lower accelerating voltage of 0.8 kV; darker regions are ZnO and lighter contrast regions are Zn.

A representative XRD pattern for one of the samples, i.e., EMI-DCA +  $H_2O$  (1:1.1), is shown in Fig. 5-5; the other samples had similar patterns. Both Zn and ZnO are clearly identified in the thin film, which confirms the SEM observation. Therefore, the formation of ZnO in EMI-DCA +

H<sub>2</sub>O (1:1.1), EMI-DCA + H<sub>2</sub>O (1:6.6) and EMI-DCA + H<sub>2</sub>O + DMSO (1:6.6:2.3) during CV cycling is confirmed through both SEM imaging and XRD structural analysis.

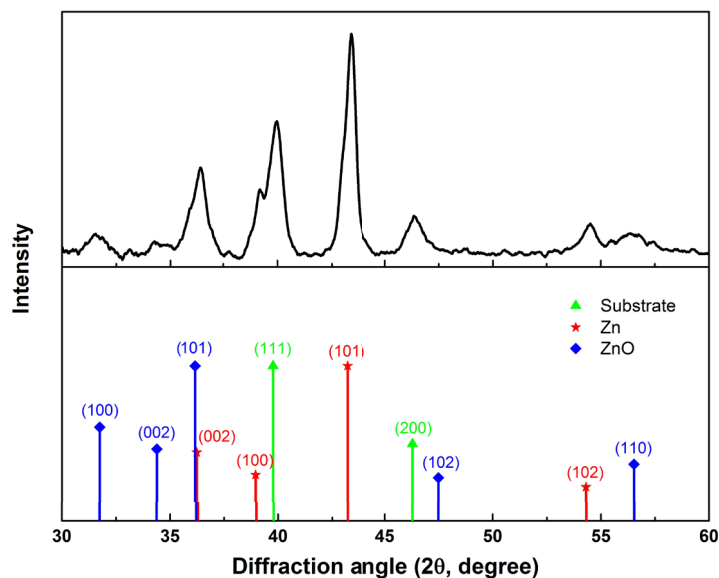


Fig. 5-5 XRD pattern for the deposit after 200 cycles in electrolyte W<sub>1</sub>: EMI-DCA + H<sub>2</sub>O (1:1.1).

### 5.3.3 Zn deposit morphology in EMI-DCA with water and/or DMSO addition

This section further reveals the influence of water and/or DMSO on the Zn deposit morphology obtained from EMI-DCA. Non-dendritic Zn deposits are obtained for all electrolytes based on EMI-DCA, although the Zn morphology varies with electrolyte composition. Uniform and compact Zn films with plate-like morphology are obtained from EMI-DCA with no water and a small amount of water addition (EMI-DCA + H<sub>2</sub>O (1:1.1)), as evident in Fig. 5-6 a-b. In EMI-DCA containing DMSO (EMI-DCA + DMSO (1:2.3) and EMI-DCA + H<sub>2</sub>O + DMSO (1:1.1:2.3)), plate-like Zn deposits grow in different orientations, so that the Zn films appear to be more porous (Fig. 5-6 d-e). This effect is desirable for battery electrode applications, since power density is related to electrode surface area. In EMI-DCA diluted with large amounts of water (Fig. 5-6 c and f), the Zn morphology is quite different. Non-uniform and less compact Zn deposits, composed of flower-like Zn nodules surrounded by dispersed Zn particles, are observed for EMI-DCA + H<sub>2</sub>O (1:6.6) (Fig. 5-6 c). Faceted Zn particles are the dominant morphology for deposits from EMI-DCA + H<sub>2</sub>O + DMSO (1:6.6:2.3), as seen in Fig. 5-6 f. These results indicate that nucleation and growth of Zn is greatly influenced by the electrolyte composition. Water and/or DMSO additions to EMI-DCA likely modify the Zn morphology by changing the

diffusion rate of Zn ions and the RTIL/substrate interface. In EMI-DCA, the Zn deposits are all in the micron size range; this is also the case for EMI-TFSI. Deposit size is, therefore, mainly determined by the type of RTIL cations, while the morphology and the growth orientation of deposits are closely related to the RTIL anions.

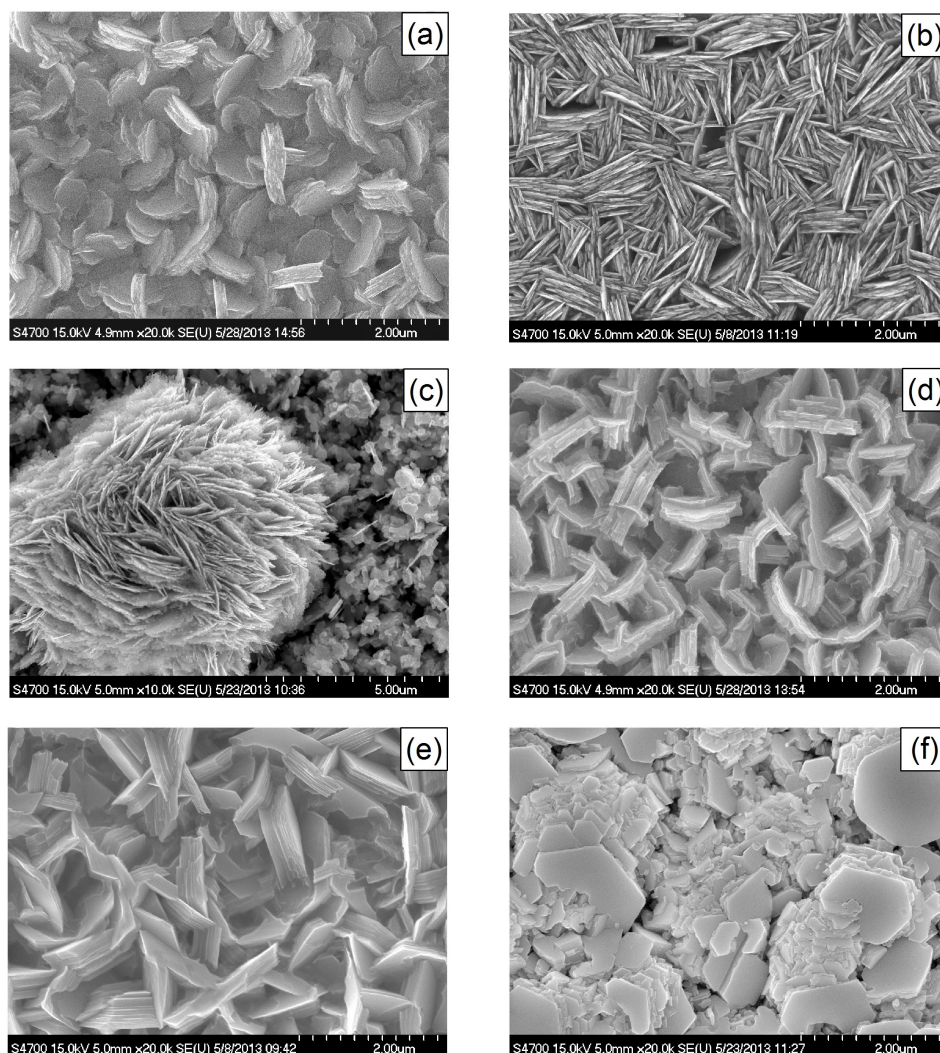


Fig. 5-6 SEM SE images of Zn electrodeposited from EMI-DCA based electrolytes: (a) E: EMI-DCA, (b)  $W_1$ : EMI-DCA +  $H_2O$  (1:1.1), (c)  $W_2$ : EMI-DCA +  $H_2O$  (1:6.6), (d) D: EMI-DCA + DMSO (1:2.3), (e)  $D/W_1$ : EMI-DCA +  $H_2O$  + DMSO (1:1.1:2.3) and (f)  $D/W_2$ : EMI-DCA +  $H_2O$  + DMSO (1:6.6:2.3).

For Zn anode rechargeable battery applications, any potential electrolyte should exhibit high conductivity and, equally important, balanced electrochemical behavior for Zn redox reactions. Adding water as a diluent to EMI-DCA is effective in enhancing both the electrolyte

conductivity and Zn redox kinetics, with a trade-off of decreased Zn redox reversibility and cyclability. Based on the current study, the drawbacks brought on by water addition can be compensated for somewhat by adding DMSO as a supplementary diluent. The addition of mixed diluents, e.g., water and DMSO, at the correct composition to EMI-DCA (EMI-DCA + H<sub>2</sub>O + DMSO (1:1.1:2.3)) generates a desirable electrolyte system. There is potential to fabricate batteries with high energy density and good cycle life, as indicated by the achievement of high kinetics and desirable reversibility and cyclability for Zn redox.

#### **5.4 Summary**

In this Chapter, electrolyte systems composed of EMI-DCA with the addition of diluent(s), water and/or DMSO, were explored. The main findings are listed below.

(1) Water enhances the conductivity of EMI-DCA greatly, while DMSO addition has no obvious contribution to conductivity improvement. The highest conductivity achieved was ~70 mS/cm when adding water to EMI-DCA at a EMI-DCA:water mole ratio of 1:1.1.

(2) Adding both water and DMSO to EMI-DCA leads to a synergistic effect that improves the electrochemical performance of the Zn redox reaction, in terms of reversibility and kinetics, that is not achievable with water or DMSO alone. For mixed diluent systems, a large amount of water addition alters the electrode reaction mechanism and impairs both Zn redox reversibility and cyclability. These drawbacks can be compensated for somewhat by adding DMSO as a supplementary diluent.

(3) An electrolyte with EMI-DCA + H<sub>2</sub>O + DMSO in a mole ratio of 1:1.1:2.3 is favorable in terms of guaranteeing improved kinetics, reversibility and cyclability for Zn redox. Desirable Zn deposit morphology, i.e., porous plate-like Zn, is obtained with this electrolyte as well.

## **Chapter 6 Electrolytes based on KOH aqueous solution with addition of RTILs with EMI<sup>+</sup> cations**

### **6.1 Overview**

Chapters 3-5 demonstrated the advantages and potential of applying RTILs as replacements for aqueous electrolytes for Zn anode rechargeable batteries, especially with the addition of diluents (water and/or DMSO). In particular, the studied RTILs with TFSI<sup>-</sup> anions and EMI-DCA showed the capability of modifying Zn deposit morphology. Nevertheless, compared with traditional aqueous electrolytes, Zn redox reactions exhibit sluggish kinetics in RTIL-based electrolytes (about two orders of magnitude lower). As for aqueous-based electrolytes for Zn anode rechargeable batteries, one major challenge is to avoid Zn dendrite formation during recharging. As such, it may be advantageous to combine the benefit of Zn morphology control using RTILs with the benefit of high Zn redox kinetics in alkaline aqueous electrolytes by using RTILs as additives to alkaline aqueous electrolytes.

This Chapter presents the efforts to modify alkaline electrolytes composed of 9.0 M KOH + 5.0 wt% ZnO with RTILs so as to solve the Zn dendrite problem. Two RTILs, i.e., EMI-TFSI and EMI-DCA with the same EMI<sup>+</sup> cation, are selected as additives. It is well known that the electrolyte composition and deposition conditions are critical factors in controlling the morphology of Zn deposits. Three aspects covered in this Chapter include: 1) a comparison between EMI-TFSI and EMI-DCA additions in terms of suppressing Zn dendrite formation in alkaline electrolytes; 2) the variation in Zn deposit morphology with RTIL concentration and the applied current density and 3) the mechanisms for Zn morphology control in RTIL added alkaline electrolytes. The results of this study may provide insights into developing novel electrolyte systems for Zn anode rechargeable batteries.

### **6.2 Experimental methods**

Potassium hydroxide (KOH, pellets, 85 wt%) and Zn oxide (ZnO, certified A.C.S.) were purchased from Alfa Aesar and Fisher Scientific, respectively. EMI-TFSI (99.9 wt%, with <0.01 wt% H<sub>2</sub>O and <0.01 wt% halides) and EMI-DCA (>98 wt%, with <0.2 wt% H<sub>2</sub>O and <1.5 wt% halides) were purchased from IoLiTec. The chemicals were used as received without further

treatment. The studied electrolytes were composed of 9.0 M KOH + 5.0 wt% ZnO without or with the addition of EMI-TFSI or EMI-DCA (0.01-1.0 wt%).

### **6.2.1 Electrochemical measurements**

A Zahner IM6 electrochemical workstation (controlled by Thales 4.15 software) and a BASi system (Bioanalytical Systems, Inc.) were utilized to perform electrochemical tests and electrodeposition. CV tests (scan rate of 50 mV/s) were performed for examining Zn redox reactions in the studied electrolytes. Chronoamperometry experiments were accomplished by stepping the potential of the working electrode from open circuit potential to -0.25 to -0.3 V vs. Zn, where the reduction of the Zn species is a diffusion-controlled process. Potentiodynamic polarization experiments were performed at 1.0 mV/s. A 3-electrode cell configuration, consisting of a Pt (1.6 mm diameter, MF-2013 BASi) WE, a Zn plate CE and a Zn plate RE were adopted for CV tests. During test, the electrolyte was first purged with nitrogen gas for 10 min and then blanketed with nitrogen gas during testing.

In order to investigate the interface between the studied electrolytes and Pt coated Si substrates during Zn electrodeposition, electrochemical impedance spectroscopy (EIS) measurements were conducted at a deposition current density of about 80 mA/cm<sup>2</sup> in 9.0 M KOH + 5.0 wt% ZnO, without and with the addition of 0.5 wt% EMI-DCA, by sweeping the frequency from 40 kHz to 1.0 Hz at an amplitude of 1.0 mA.

### **6.2.2 Electrodeposition and SEM**

Zinc coatings were electrodeposited on Pt coated Si substrates from 9.0 M KOH + 5.0 wt% ZnO without or with the addition of EMI-TFSI or EMI-DCA. Electrodeposition was conducted at either a constant deposition potential of -0.15 V vs. Zn or constant deposition current densities of 20-100 mA/cm<sup>2</sup>. The same CE and RE were used in electrodeposition as that in the CV tests. The morphology of the deposits was analyzed with a Hitachi S-3500N SEM operated at 20 kV.

## **6.3 Results and discussion**

### **6.3.1 Comparison of EMI-TFSI and EMI-DCA as additives in alkaline electrolytes**

The first issue of concern when adding RTILs to an alkaline aqueous electrolyte is solubility. Compared with EMI-TFSI, which is hydrophobic in nature, hydrophilic EMI-DCA is more soluble in aqueous electrolytes. The solubility limit for EMI-DCA in an electrolyte containing

9.0 M KOH + 5.0 wt% ZnO is about 1.0 wt% and the mixed electrolyte turns from colorless to light yellow (the color of EMI-DCA) once the concentration exceeds 1.0-2.0 wt% EMI-DCA. Only about 0.1 wt% EMI-TFSI can be completely dissolved into an electrolyte composed of 9.0 M KOH + 5.0 wt% ZnO; insoluble EMI-TFSI droplets are visible at higher concentrations.

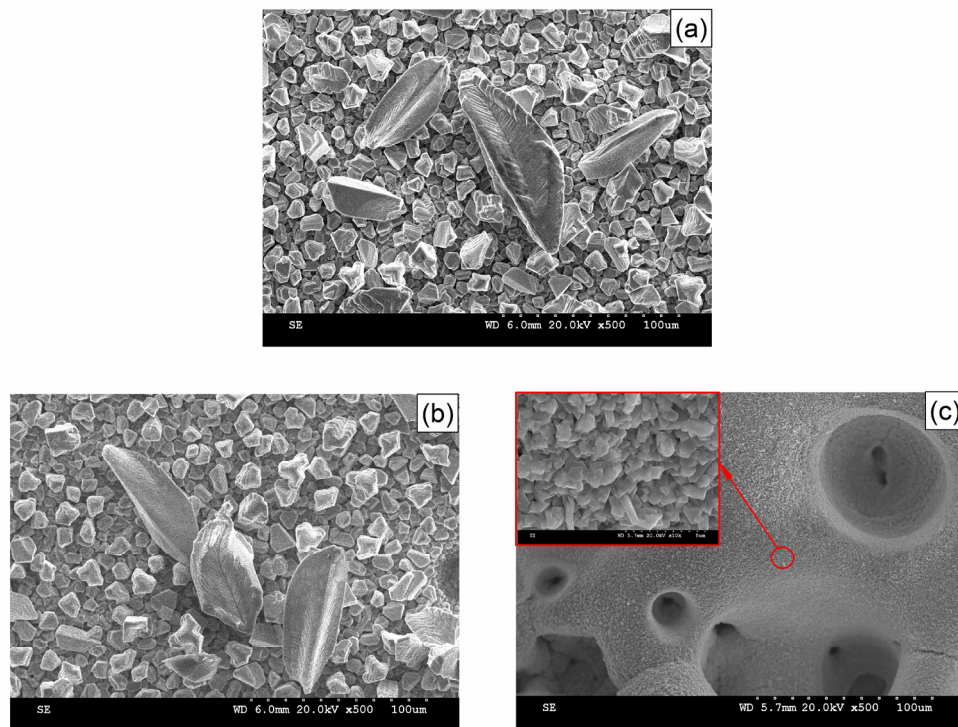


Fig. 6-1 SEM SE images of Zn electrodeposited on Pt coated Si substrates at a constant potential (-0.15 V vs. Zn wire) from: (a) 9.0 M KOH + 5.0 wt% ZnO, (b) 9.0 M KOH + 5.0 wt% ZnO + 0.1 wt% EMI-TFSI and (c) 9.0 M KOH + 5.0 wt% ZnO + 1.0 wt% EMI-DCA.

Zinc dendrites (Fig. 6-1 a) are clearly observed in deposits from the 9.0 M KOH + 5.0 wt% ZnO electrolyte with no additives, under constant potential deposition conditions (-0.15 V vs. Zn). The addition of 0.1 wt% EMI-TFSI does not depress the formation of Zn dendrites (Fig. 6-1 b). On the other hand, 1.0 wt% addition of EMI-DCA significantly changes the deposit morphology (Fig. 6-1 c). Granular Zn deposits predominate and no dendrites were found in the deposit. EMI-DCA is clearly more effective at suppressing Zn dendrite formation than EMI-TFSI. The next section is, therefore, focused on EMI-DCA as the additive to 9.0 M KOH + 5.0 wt% ZnO electrolytes.

### 6.3.2 Zn morphology as a function of EMI-DCA concentration and current density

The morphology of Zn electrodeposited under constant current density conditions ( $20 \text{ mA/cm}^2$ ) from an electrolyte containing  $9.0 \text{ M KOH} + 5.0 \text{ wt\% ZnO}$  with different concentrations (0.01, 0.1 and 1 wt%) of EMI-DCA is shown in Fig. 6-2. Zinc deposits obtained from the  $9.0 \text{ M KOH} + 5.0 \text{ wt\% ZnO}$  electrolyte, with no EMI-DCA added, are composed of fibrous clusters dispersed on a continuous Zn layer as seen in Fig. 6-2 a. It is clear that no Zn dendrites are present, unlike the deposits obtained at a constant potential of  $-0.15 \text{ V vs. Zn}$  (Fig. 6-1 a). The potential profile during electrodeposition may provide an explanation for the morphology variation. From Fig. 6-3, it can be seen that at an applied current density of  $20 \text{ mA/cm}^2$ , the corresponding Zn deposition potential in  $9.0 \text{ M KOH} + 5.0 \text{ wt\% ZnO}$  is far lower than  $-0.15 \text{ V}$ , i.e., approximately  $-0.035 \text{ V}$  or less. Under these conditions, Zn deposition is not under diffusion control and dendrite initiation is not favored. For Zn deposition from the  $9.0 \text{ M KOH} + 5.0 \text{ wt\% ZnO}$  electrolyte, with 0.01 and 0.1 wt% EMI-DCA additions, the deposition potential is similar to that with no EMI-DCA. Compared with the Zn morphology displayed in Fig. 6-2 a, there is no significant change in Zn deposit morphology after adding 0.01 and 0.1 wt% EMI-DCA, respectively (Fig. 6-2 b-c). Only the surface density of the fibrous clusters increases with increasing amount of EMI-DCA added, which may be ascribed to the slight increase in deposition potential. It is noteworthy to mention that deposits characterized by these fibrous clusters show poor adhesion properties. With the addition of 1.0 wt% EMI-DCA, the Zn deposit is much finer, changing from a fibrous structure to a granular texture that is adherent to the substrate (Fig. 6-2 d). As shown in Fig. 6-3, the deposition potential is around  $-0.1 \text{ V vs. Zn}$  in the  $9.0 \text{ M KOH} + 5.0 \text{ wt\% ZnO} + 1.0 \text{ wt\% EMI-DCA}$  electrolyte. As expected, the Zn morphology in Fig. 6-2 d is similar to that deposited at a constant potential of  $-0.15 \text{ V vs. Zn}$  observed in Fig. 6-1 c. It is, therefore, apparent that a critical amount of EMI-DCA, i.e., more than 0.1 wt%, is required to modify Zn deposit morphology obtained from a  $9.0 \text{ M KOH} + 5.0 \text{ wt\% ZnO}$  electrolyte.

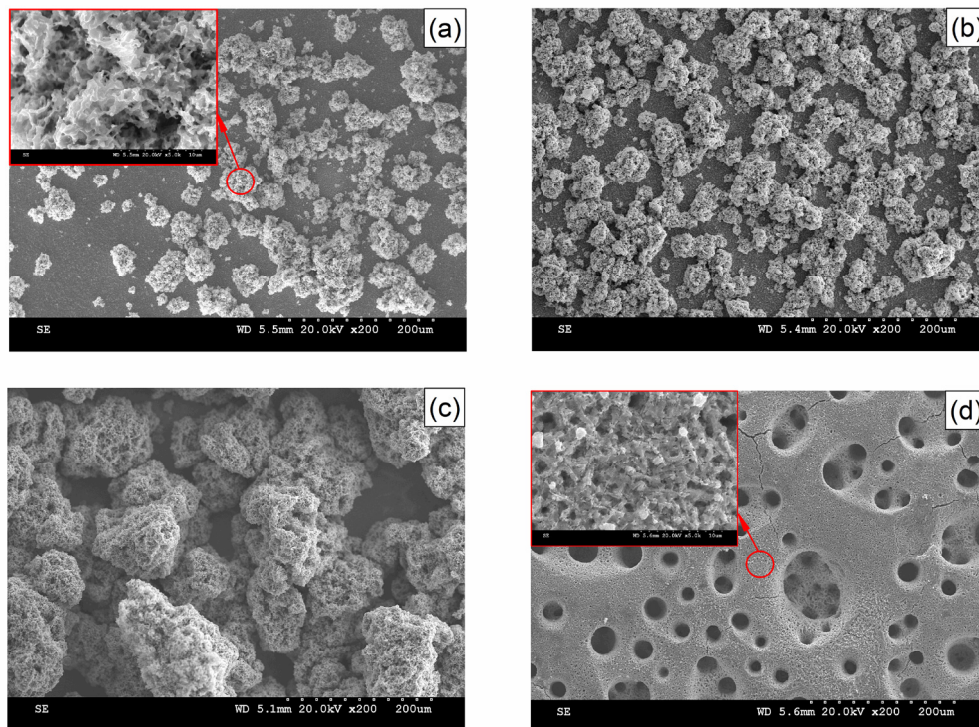


Fig. 6-2 SEM SE images of Zn electrodeposited on Pt coated Si substrates at a constant current density ( $20 \text{ mA/cm}^2$ ) from: (a) 9M KOH + 5 wt% ZnO, (b) 9M KOH + 5 wt% ZnO + 0.01 wt% EMI-DCA, (c) 9M KOH + 5 wt% ZnO + 0.1 wt% EMI-DCA and (d) 9M KOH + 5 wt% ZnO + 1 wt% EMI-DCA.

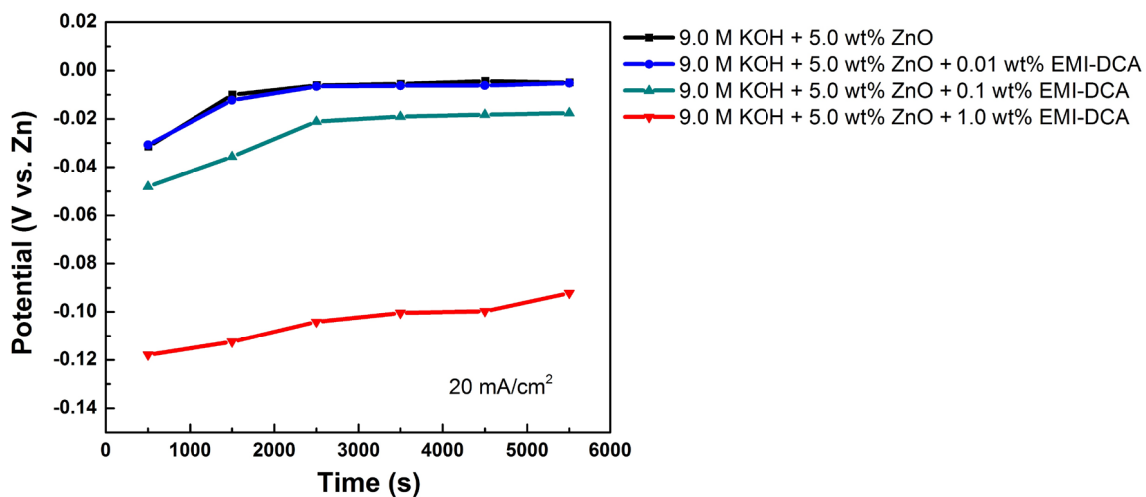


Fig. 6-3 Potential vs. time plots (at a current density of  $20 \text{ mA/cm}^2$ ) during Zn electrodeposition from 9.0 M KOH + 5.0 wt% ZnO electrolytes with the addition of different concentrations EMI-DCA.

As revealed in the CV plots in Fig. 6-4 and Table 6-1, adding EMI-DCA to the alkaline electrolyte leads to a decrease in the current density and diffusion coefficient, as well as an increase in the overpotential for Zn redox, even though the small amount of EMI-DCA maintains the Zn kinetic properties at the same order of magnitude as that without EMI-DCA addition. In order to guarantee good Zn kinetic performance and to achieve desirable Zn deposit morphology at the same time, a concentration of 0.5 wt% (within 0.1-1.0 wt%) of EMI-DCA is added to the 9.0 M KOH + 5.0 wt% ZnO electrolyte. Zinc deposits were obtained from 9.0 M KOH + 5.0 wt% ZnO electrolytes, without and with 0.5 wt% EMI-DCA addition, at applied current densities ranging from 40 to 100 mA/cm<sup>2</sup>; the results are shown in Fig. 6-5.

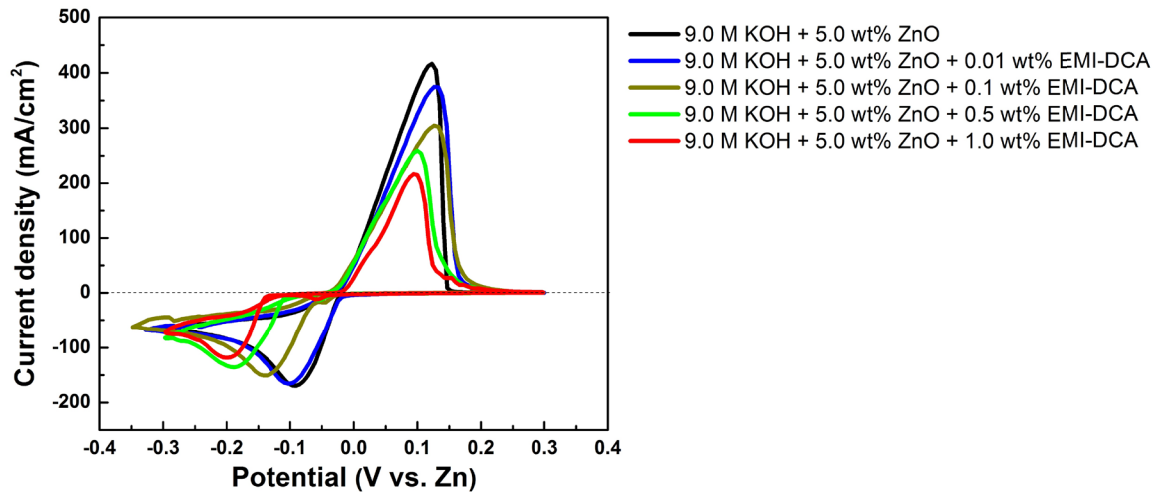


Fig. 6-4 CV plots at 50 mV/s for Zn redox in 9.0 M KOH + 5.0 wt% ZnO electrolytes with the addition of different concentrations EMI-DCA.

Table 6-1 Kinetic properties for Zn redox in 9.0 M KOH + 5.0 wt% ZnO added with EMI-DCA

Concentration of EMI-DCA (wt%)	$\Delta E_p$ (V)	$D_0$ ( $\times 10^{-4}$ cm <sup>2</sup> /s)	$j_0$ (mA/cm <sup>2</sup> )
0	0.21	6.0	5.5
0.01	0.23	4.2	4.7
0.1	0.27	2.1	3.3
0.5	0.29	1.6	2.0
1	0.30	0.70	1.5

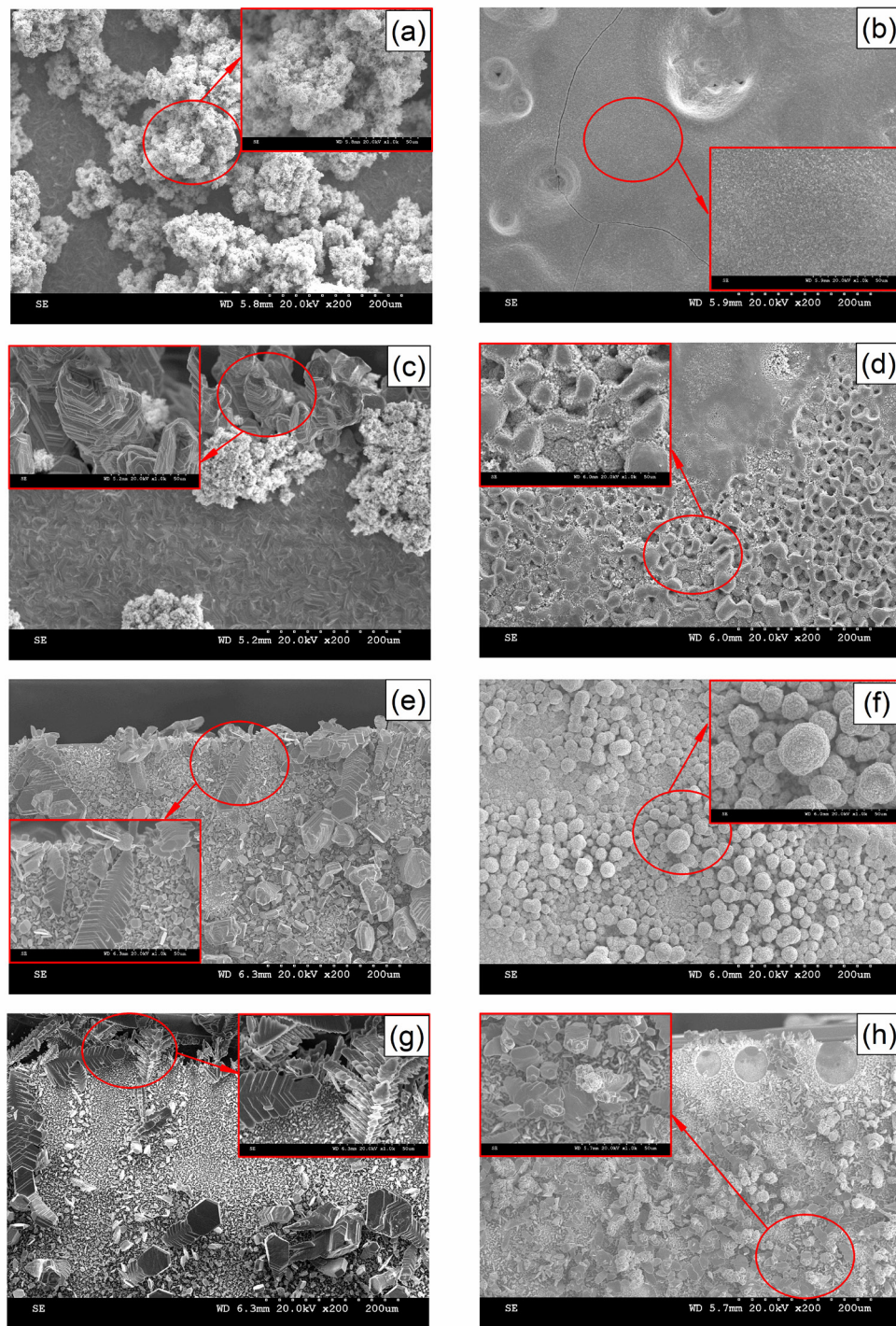


Fig. 6-5 SEM SE images of Zn deposited on Pt coated Si substrates from 9.0 M KOH + 5.0 wt% ZnO (left column) and 9.0 M KOH + 5.0 wt% ZnO + 0.5 wt% EMI-DCA (right column) at different current densities: (a) (b)  $40 \text{ mA/cm}^2$ , (c) (d)  $60 \text{ mA/cm}^2$ , (e) (f)  $80 \text{ mA/cm}^2$  and (g) (h)  $100 \text{ mA/cm}^2$ .

The formation of dendritic Zn is preferred at high current densities, while the addition of 0.5 wt% EMI-DCA postponed the initiation of Zn dendrites. As seen in Fig. 6-5 a and c, dendritic formation of Zn deposits occurs in the 9.0 M KOH + 5.0 wt% ZnO electrolyte when the current density increases from 40 to 60 mA/cm<sup>2</sup>. A further increase in the cathodic current density promotes the growth of Zn dendrites (Fig. 6-5 e and g). The formation of Zn dendrites does not take place in the 9.0 M KOH + 5.0 wt% ZnO + 0.5 wt% EMI-DCA electrolyte until the applied current density reaches 100 mA/cm<sup>2</sup> (Fig. 6-5 h). Moreover, it is interesting that at a current density of 80 mA/cm<sup>2</sup>, a desirable Zn deposit morphology characterized by homogenous granular clusters is obtained (Fig. 6-5 f) without the presence of cracks (Fig. 6-5 b) or dendrites (Fig. 6-5 h).

### **6.3.3 Mechanisms of Zn morphology control in alkaline electrolytes with EMI-DCA**

As revealed from the above study, a porous, dendrite-free Zn film characterized by clusters of small Zn particles was obtained from the alkaline electrolyte with the addition of 0.5 wt% EMI-DCA at a high deposition current density of 80 mA/cm<sup>2</sup>. This kind of morphology is desired for battery electrode applications, not only because of Zn dendrites are eliminated, but also due to its high surface areas that are good for power density. It is therefore also of interest to investigate the mechanism of Zn morphology control at this deposition condition.

From Fig. 6-4, it is noteworthy that during the cathodic CV scan, instead of the one reduction peak appearing at about -0.1 V for the 9.0 M KOH + 5.0 wt% ZnO electrolyte, two reduction peaks, with a small one near -0.05 V and another one near -0.2 V, are observed in the presence of EMI-DCA (>0.1 wt%). This is similar to the Zn redox behavior observed in pure ionic liquids BMP-DCA (Chapter 3) or in EMI-DCA without or with diluent addition (Chapter 4), i.e., the appearance of two Zn reduction peaks. This effect was ascribed to the formation of complex ions between Zn<sup>2+</sup> and DCA<sup>-</sup> and altered electrode reaction paths. The consequence is the redistribution of the electrode potential during electrodeposition. As shown in Fig. 6-6, the electrode potential varies with time during Zn electrodeposition at a constant current density of 80 mA/cm<sup>2</sup>. In the 9.0 M KOH + 5.0 wt% ZnO solution, the potential increases sharply for the first 300 s and then increases slowly thereafter. For the same solution with 0.5 wt% EMI-DCA, the potential also increases over the same time interval, but less sharply, and then stabilizes after about 300 s.

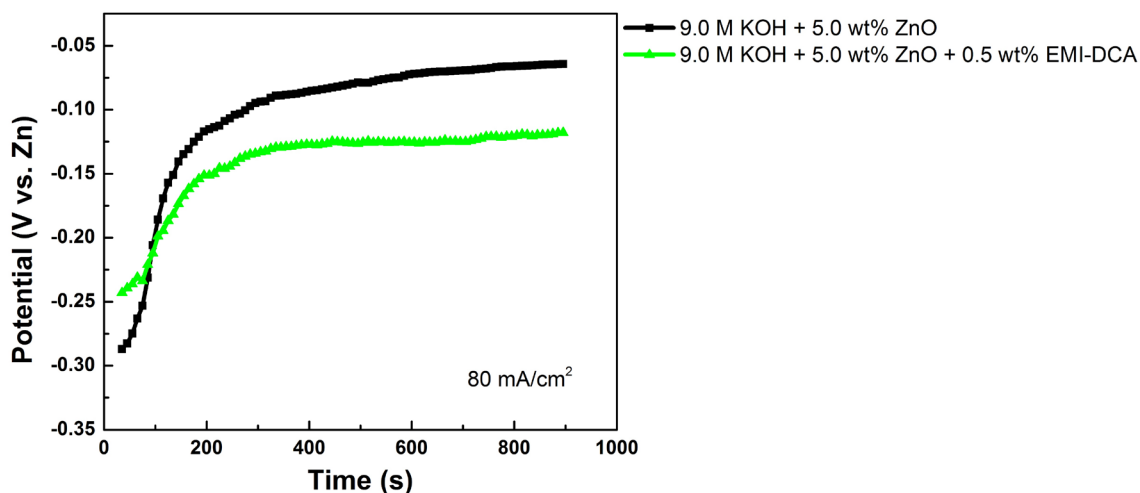


Fig. 6-6 Potential vs. time plots (at a current density of  $80 \text{ mA/cm}^2$ ) during Zn electrodeposition for electrolytes composed of  $9.0 \text{ M KOH} + 5.0 \text{ wt\% ZnO}$ , without and with  $0.5 \text{ wt\% EMI-DCA}$ .

Clearly, the addition of EMI-DCA facilitates a smaller change in potential upon the passage of current before and after the deposition. The formation of Zn dendrites is due to the uneven deposition of Zn at active sites, where discharged Zn species gather. The key to suppressing Zn dendrite formation is, therefore, to promote uniform deposition of Zn on charging. The smaller variation in deposition potential is beneficial for promoting the homogeneous deposition of Zn in the alkaline electrolyte containing EMI-DCA (Fig. 6-5 f).

The dominant Zn morphology is mainly determined by the first 300 s of deposition, i.e., the deposition time over which the potential keeps increasing (Fig 6-6). For the electrolyte without EMI-DCA, the electrode potential is in the range of  $-0.29 \text{ V}$  to  $-0.1 \text{ V}$  during this time period, where electrodeposition is mainly controlled by diffusion as indicated in the CV curve (black curve in Fig. 6-4) and the formation of dendritic Zn is favored. On the other hand, for the electrolyte containing  $0.5 \text{ wt\% EMI-DCA}$ , the electrode potential varies from  $-0.24 \text{ V}$  to  $-0.13 \text{ V}$ , which mainly corresponds to activation control (green CV curve in Fig. 6-4). As such, Zn dendrites do not form. The Nyquist plots shown in Fig. 6-7 further confirm that under the electrodeposition conditions, Zn reduction is diffusion controlled, as indicated by the linear plot ( $1\text{-}54 \text{ Hz}$ ) for the  $9.0 \text{ M KOH} + 5.0 \text{ wt\% ZnO}$  electrolyte. A larger charge transfer resistance is found for Zn reduction from the electrolyte with EMI-DCA, which suggests slower reaction kinetics and is consistent with the CV results. More notably, in the low frequency range ( $2\text{-}6 \text{ Hz}$ ), there is a half inductive loop for the electrolyte containing EMI-DCA. It is speculated that

specific adsorption of the alkyl groups of the  $\text{EMI}^+$  cations on the growing Zn deposits accounts for this impedance response. These adsorbed alkyl groups may block the reaction sites where Zn grows more rapidly and thus inhibit preferential Zn growth and Zn dendrite formation.

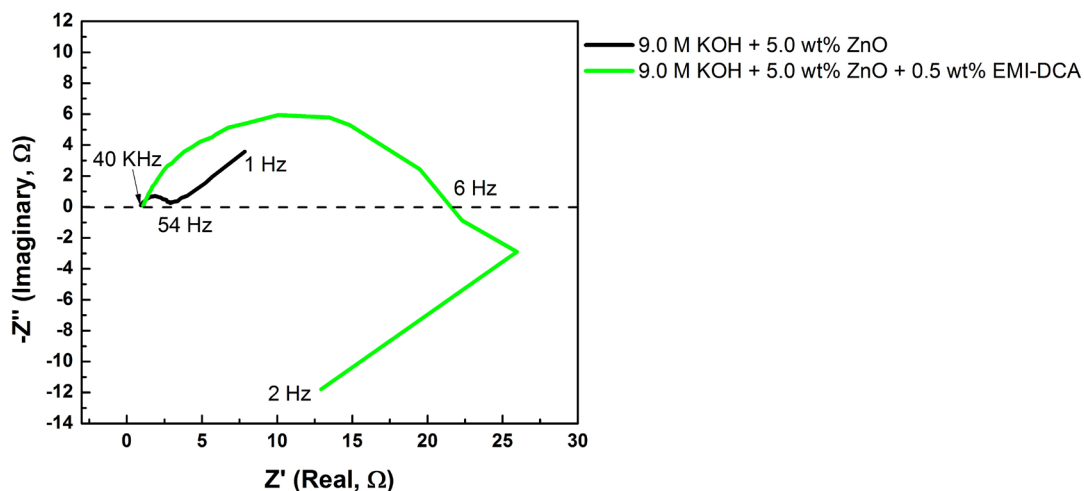


Fig. 6-7 Nyquist plots at a deposition current density of  $80 \text{ mA/cm}^2$  for electrolytes composed of 9.0 M KOH + 5.0 wt% ZnO, without and with 0.5 wt% EMI-DCA.

The current study demonstrates that a RTIL can be added to an alkaline aqueous electrolyte to beneficially modify Zn deposit morphology. It is worth mentioning that there is a threshold concentration for the added RTIL to eliminate the formation of Zn dendrites. As such, hydrophobic RTILs (e.g., EMI-TFSI) may be of no benefit in modifying Zn deposit morphology because of their low solubility ( $<0.1 \text{ wt}\%$ ) in aqueous electrolytes. Hydrophilic RTIL EMI-DCA, on the other hand, exhibits promising characteristics for generating more uniform Zn deposits. Based on the present study, the role of EMI-DCA on Zn deposit morphology is related to the intrinsic properties of both its anion  $\text{DCA}^-$  and cation  $\text{EMI}^+$ . The  $\text{DCA}^-$  anion optimizes the potential distribution and inhibits dendritic initiation during Zn electrodeposition, while the  $\text{EMI}^+$  cation may physically block Zn deposition sites and inhibit Zn dendritic growth.

#### 6.4 Summary

This chapter explored the use of RTILs as electrolyte additives to 9.0 M KOH + 5.0 wt% ZnO electrolytes with the purpose of developing novel electrolyte systems for Zn anode rechargeable batteries. The results show the advantages of using RTILs to eliminate Zn dendrite formation and

provide insights into the criteria for selecting appropriate RTIL additives for generating promising battery electrolytes.

(1) For conventional alkaline aqueous electrolytes, hydrophilic RTIL EMI-DCA is better relative to hydrophobic EMI-TFSI in terms of obtaining desirable Zn morphologies and preventing dendritic Zn formation. The former has a low solubility (around 0.01 wt%) in alkaline electrolytes and shows a negligible effect on modifying Zn deposit morphology.

(2) A critical amount of EMI-DCA, i.e., more than 0.1 wt%, is required to effectively modify Zn deposit morphology obtained from the alkaline aqueous electrolyte. In particular, 0.5 wt% is found to be the proper concentration to balance the Zn redox kinetics and Zn deposit morphology.

(3) EMI-DCA modifies the Zn deposit morphology by changing the Zn reduction process and the Zn film/electrolyte interface. The former effect was achieved by increasing the reduction overpotential, decreasing the reaction rate and narrowing the potential variation during electrodeposition. The latter effect was likely a result of EMI<sup>+</sup> cations being specifically adsorbed on the deposited Zn. All these modifications suppressed the uneven deposition of Zn in the conventional alkaline electrolyte and prevented Zn dendritic growth.

## **Chapter 7 Conclusions and Recommendations**

In this thesis, novel electrolyte systems with room temperature ionic liquids (RTILs) as the major or supporting components were investigated for application to Zn anode rechargeable batteries. As pointed out in Chapters 1-2, conventional alkaline aqueous electrolytes used for Zn anode rechargeable batteries have an intrinsic problem of drying-out during operation and they cause Zn dendrite formation and consequent short circuiting as well. The undesirable outcome is then short battery cycle life. RTILs, which are characterized by attractive properties of low or no volatility, low melting temperature, high thermal stability, wide electrochemical window and the capability of modifying metal deposits, were studied as advanced and safe electrolyte alternatives for Zn anode rechargeable batteries. The electrochemical examination of Zn redox reactions, together with the investigation of Zn deposit morphology in electrolytes containing selected RTILs, was highlighted in Chapters 3-6, with the purpose of uncovering the feasibility and potential of applying RTILs as electrolytes/electrolyte components.

In this final Chapter, the accomplishments and understanding obtained through this research work are reviewed and summarized. In addition, recommendations are given for future work in terms of further improving the electrolyte systems studied in this work and sharing ideas on developing electrolytes for Zn anode rechargeable batteries.

### **7.1 Electrolyte system based on RTILs with the addition of diluents**

The electrochemical behavior of Zn redox reactions and Zn deposit morphology were systematically investigated for six different RTILs, i.e., BMP-TFSI, MPP-TFSI, MPrP-TFSI, EMI-TFSI, BMP-DCA and EMI-DCA, without or with the addition of diluents (water and/or DMSO). The mechanisms regarding the dependence of Zn redox behavior (kinetics, reversibility and cyclability) on the types of cations/anions of the RTILs, and on water/DMSO diluents, were elucidated. On the basis of the present study, potential RTIL-based electrolytes were also suggested for application to Zn anode rechargeable batteries.

#### **(1) RTILs cations/anions effects on Zn redox behavior and Zn deposit morphology**

Depending on the RTILs anions involved, the Zn species dissolved in the studied RTILs exhibited different forms, which affected the Zn redox reaction mechanisms, the reaction kinetics and Zn redox cyclability. In RTILs with TFSI<sup>-</sup> anions (BMP-TFSI, MPP-TFSI, MPrP-TFSI and

EMI-TFSI),  $Zn^{2+}$  ions are present with the electrode reaction occurring in a single-step, two-electron transfer process. In RTILs with  $DCA^-$  anions (BMP-DCA and EMI-DCA), on the other hand, complex ions between Zn ions and  $DCA^-$  form, turning the electrode reaction into a two-step, single-electron process. The diffusion coefficient for  $Zn^{2+}$  ions in RTILs with TFSI anions is higher than that for the complex ion ( $Zn(DCA)_x^{(x-2)-}$ ) in RTILs with  $DCA^-$  anions. Similarly, Zn redox has a higher exchange current density in BMP-TFSI, MPP-TFSI, MPrP-TFSI and EMI-TFSI than that in BMP-DCA and EMI-DCA. On the other hand, in RTILs with  $DCA^-$  anions, Zn redox has a smaller overpotential and exhibits better cyclability as well.

With respect to Zn deposit morphology, this study confirms the benefits of using RTILs to obtain non-dendritic Zn deposits. Furthermore, the cations of the RTILs have an effect on the deposit size, while the morphology and the growth orientation of deposits are closely related to the RTIL anions. When comparing Zn deposits obtained from BMP-TFSI/MPrP-TFSI with those from EMI-TFSI/EMI-DCA, nanometer size Zn was observed in the former group with pyrrolidinium cations, while micrometer size Zn was found in the latter group with imidazolium cations. With the same  $EMI^+$  cations, different Zn morphologies, i.e., faceted Zn and plate-like Zn, are prevalent in EMI-TFSI and EMI-DCA, respectively.

## (2) Diluents effects on Zn redox behavior and Zn redox morphology

The incorporation of diluents, water and/or DMSO, into RTILs improves electrolyte conductivity. In the studied hydrophobic RTILs, BMP-TFSI, MPrP-TFSI and EMI-TFSI, 2.0-2.5 wt% water addition leads to the maximum conductivity achieved. The presence of water-ion interactions through H-bonding perturbs the ion-ion association of the RTILs, facilitates the dissociation of cation-anion pairs and results in decreased viscosity and increased conductivity. In hydrophilic EMI-DCA, water is found to be more effective than DMSO in improving electrolyte conductivity.

According to DFT calculations, water enhances the dissolution of Zn ions in the three hydrophobic RTILs with TFSI anions, which increases the concentration of  $Zn^{2+}$  involved in the redox reaction and improves the overall Zn redox reaction rate and diffusion rates as a consequence. Nevertheless, water impairs Zn redox reversibility in both hydrophobic (BMP-TFSI, MPrP-TFSI and EMI-TFSI) and hydrophilic (EMI-DCA) RTILs, which is most likely

induced by the decomposition of water and the formation of the irreversible product ZnO. The drawbacks caused by water can be compensated somewhat by adding DMSO as a supplementary diluent. Adding both water and DMSO to EMI-DCA leads to a synergistic effect that improves the electrochemical performance of the Zn redox reaction, in terms of reversibility and kinetics, that is not achievable with water or DMSO alone.

The influence of diluents on the Zn deposit morphology is related to the RTIL involved. For the two RTILs with pyrrolidinium cations, i.e., BMP-TFSI and MPrP-TFSI, the increased mass transfer rate upon water addition causes the growth of Zn deposits and the deposition is not compact. For the other two RTILs with imidazolium cations, i.e., EMI-TFSI and EMI-DCA, water addition does not affect the deposit size. However, a large amount of water in EMI-DCA (i.e., mole ratio of EMI-DCA to water equal to 1:6.6) is not preferred for electrodeposition as Zn deposits become non-uniform and less compact. It is also worth mentioning that the addition of both water and DMSO to EMI-DCA is beneficial for modifying Zn deposits as porous structures, which is good for battery electrode applications.

### (3) Potential RTIL-based electrolytes for Zn anode rechargeable batteries

For RTIL-based electrolytes, the conductivities and Zn redox kinetics are about two orders of magnitude lower than those for conventional alkaline aqueous electrolytes. Therefore, it is necessary to incorporate diluents into the RTILs to improve the electrolyte and Zn redox performance and to facilitate the full utilization of the merits of RTILs. Among the studied RTILs, the most promising electrolyte is composed of EMI-DCA with the addition of both H<sub>2</sub>O and DMSO in a mole ratio of 1:1.1:2.3. This EMI-DCA based electrolyte exhibits the best performance with respect to electrolyte conductivity, electrochemical properties for Zn redox and Zn deposit morphology.

Considering the relatively high viscosity of RTILs, one of the essential subjects for future studies is to incorporate other organic/inorganic diluents to decrease viscosities and increase conductivities of RTIL-based electrolytes. With respect to the application for Zn anode rechargeable batteries, some fundamental studies are suggested below for future work.

(I) Further selection of promising RTILs candidates, together with proper diluents, is an ongoing task to optimize an RTIL-based electrolyte system. In addition to RTILs with pyrrolidinium and

imidazolium cations investigated in this study, those with ammonium cations having low viscosities and wide electrochemical windows are worth examining. Good diluent candidates are expected to be nontoxic, show low viscosity and have a minimal effect on RTIL electrochemical stability at the same time. Propylene carbonate and triglyme are potential electrolyte additives, from this point of view. The cathode used for Zn anode recharge batteries may also determine the choice of diluents. For example, DMSO appears to be the preferred diluent for Zn-air batteries, since it is capable of stabilizing oxygen reduction reaction intermediates (superoxide radicals) [150].

(II) Understanding of the RTIL-diluent interactions, as well as the solvation of Zn salts in the RTIL-based electrolytes, needs to be elucidated for any new RTIL system proposed, as it is important for predicting the transport properties and the kinetic performance of electrochemical reactions. For the promising electrolyte system EMI-DCA, with the addition of both water and DMSO, the complex interactions among EMI-DCA, water, DMSO and dissolved Zn ions are not clear. The combination of experimental techniques, such as infrared (IR) and nuclear magnetic resonance (NMR) spectroscopies, with theoretical calculations including density functional theory (DFT) and the conductor-like screening model for real solvents (COSMO-RS) are expected to be effective to improve this knowledge.

(III) In order to take full advantage of using RTILs to modify/predict Zn deposit morphology, obtaining an understanding of RTIL/electrode interfacial structure, as well as the potential distribution in RTILs at the charged interface, is key. Apart from traditional electrochemical methods such as electrochemical impedance spectroscopy used in this study, in-situ atomic force microscopy (AFM) and in-situ scanning tunnelling microscopy (STM) are recommended techniques for revealing the RTIL/electrode interface structure (RTIL layer structure near the interface, electrode surface morphology, etc.) without and with the addition of Zn ions and diluents, and uncovering the mechanisms responsible for the Zn deposit morphology (i.e., with various orientations and sizes) obtained under an applied deposition potential or current density.

## **7.2 Electrolyte system based on alkaline aqueous solutions with the addition of RTILs**

With the goal of combining the benefit of Zn morphology control using RTILs with the benefit of high Zn redox kinetics in alkaline aqueous electrolytes, an electrolyte using an RTIL as an additive to an alkaline aqueous electrolyte was also explored as a novel system. In particular, a

comparison of using hydrophobic EMI-TFSI and hydrophilic EMI-DCA as electrolyte additives for a 9.0 M KOH + 5.0 wt% ZnO electrolyte was presented, providing insights into the criteria for selecting appropriate RTIL additives for generating promising battery electrolytes. The mechanisms of Zn morphology control in an EMI-DCA added alkaline electrolyte were demonstrated as well.

(1) A threshold concentration for the added RTIL in an alkaline aqueous electrolyte is required to eliminate Zn dendrite formation. In a 9.0 M KOH + 5.0 wt% ZnO electrolyte containing EMI-TFSI, where only around 0.01 wt% EMI-TFSI can be added (limited by its solubility), Zn deposit morphology shows negligible improvement. In a 9.0 M KOH + 5.0 wt% ZnO electrolyte containing EMI-DCA, more than 0.1 wt% EMI-DCA is mandatory to eliminate the formation of Zn dendrites.

(2) Based on the present study, the role of EMI-DCA on Zn deposit morphology is linked to the intrinsic properties of both its anion  $\text{DCA}^-$  and cation  $\text{EMI}^+$ . The  $\text{DCA}^-$  anion optimizes the potential distribution and inhibits dendritic initiation during Zn electrodeposition, while the  $\text{EMI}^+$  cation could physically block Zn deposition sites and inhibit Zn dendritic growth.

(3) The experimental results suggest that a 9.0 M KOH + 5.0 wt% ZnO electrolyte with EMI-DCA added in a proper concentration of 0.5 wt% guarantees balanced Zn redox kinetics and desirable Zn deposit morphology. As such, it is a promising electrolyte system for Zn anode rechargeable batteries.

This work examined the use of RTILs as electrolytes/electrolyte components for the potential application to Zn anode rechargeable batteries, providing insight on the way to develop a novel electrolyte system with RTILs. It should be pointed out that a simple electrolyte system composed of a pure RTIL, or RTILs with diluents or RTIL modified alkaline aqueous solutions as investigated here, is still unable to fulfill all the needs that are required by rechargeable batteries (e.g., high energy/power density and long cycle life). The way of adopting electrolytes for a particular Zn anode rechargeable cell is also of interest. With the aim of achieving practical application for these RTIL-based electrolytes, efforts that are required to make in future studies include:

(I) Fabrication of a Zn-anode cell and cell performance tests (charge-discharge, etc.) are recommended for any proposed RTIL-containing electrolytes. As examples, electrolytes composed of EMI-DCA + H<sub>2</sub>O + DMSO in a mole ratio of 1:1.1:2.3 and 9.0 M KOH + 5.0 wt% ZnO + 0.5 wt% EMI-DCA are suggested to be incorporated and tested in a Zn-air cell and a Zn-MnO<sub>2</sub> cell, respectively.

(II) To employ a separated electrolyte system for the battery configuration, i.e., using an RTIL-containing electrolyte for the Zn anode part (to avoid Zn dendrite formation) and an aqueous electrolyte for the cathode (to achieve high kinetic performance). This concept has been examined recently, for developing stationary batteries, by Chou et al. [151], where they adopted ionic liquids for the Li anode and aqueous electrolytes for MnO<sub>2</sub> cathode, with the benefits of achieving both high energy and long cycle life.

In closing, RTILs are not only potential but promising electrolyte components for Zn anode rechargeable batteries. An applicable RTIL-containing electrolyte system relies on proper electrolyte formulation (the selection of RTILs and their concentration, the adoption of cosolvents/diluents, etc.), as well as the battery configuration (the use of cathode, the distribution of electrolytes, the selection of the separator, etc.), which require collaborative work from both fundamental experiments and computer simulations.

## References

- [1] N. Serizawa, Y. Katayama, T. Miura, *Electrochimica Acta*, 56 (2010) 346-351.
- [2] C. Gerbaldi, J.R. Nair, S. Ahmad, G. Meligrana, R. Bongiovanni, S. Bodoardo, N. Penazzi, *Journal of Power Sources*, 195 (2010) 1706-1713.
- [3] Y.L. Zhu, Y. Kozuma, Y. Katayama, T. Miura, *Electrochimica Acta*, 54 (2009) 7502-7506.
- [4] S. Zein El Abedin, E.M. Moustafa, R. Hempelmann, H. Natter, F. Endres, *ChemPhysChem*, 7 (2006) 1535-1543.
- [5] X.G. Sun, C. Liao, N. Shao, J.R. Bell, B. Guo, H. Luo, D.E. Jiang, S. Dai, *Journal of Power Sources*, 237 (2013) 5-12.
- [6] K. Tsunashima, S. Kodama, M. Sugiya, Y. Kunugi, *Electrochimica Acta*, 56 (2010) 762-766.
- [7] T.I. Leong, Y.T. Hsieh, I.W. Sun, *Electrochimica Acta*, 56 (2011) 3941-3946.
- [8] P. Hapiot, C. Lagrost, *Chemical Reviews*, 108 (2008) 2238-2264.
- [9] G. Bronoel, A. Millot, N. Tassin, *Journal of Power Sources*, 34 (1991) 243-255.
- [10] H. Huang, L. Zhang, W.K. Zhang, Y.P. Gan, H. Shao, *Journal of Power Sources*, 184 (2008) 663-667.
- [11] C. Ponce de Leon, F.C. Walsh, Secondary batteries - zinc systems: zinc-bromine, in: *Encyclopedia of Electrochemical Power Sources*, C. Dyer, Garche, Juergen, Moseley, Patrick, Ogumi, Zempachi, Rand, David and Scrosati, Bruno (Ed.), Elsevier, Amsterdam, NL, 2009, pp. 487-496.
- [12] P.C. Butler, P.A. Eidler, P.G. Grimes, S.E. Klassen, R.C. Miles, Zinc/Bromine Batteries, in: *Handbook of Batteries*, D. Linden, T.B. Reddy (Eds.), McGraw-Hill, 2001, pp. 37.01-37.16.
- [13] J. Zhang, D. Shan, S. Mu, *Journal of Power Sources*, 161 (2006) 685-691.
- [14] M.S. Rahmanifar, M.F. Mousavi, M. Shamsipur, *Journal of Power Sources*, 110 (2002) 229-232.
- [15] W.J. Wruck, B. Reichman, K.R. Bullock, W.H. Kao, *Journal of the Electrochemical Society*, 138 (1991) 3560-3567.
- [16] Q.f. Li, N.J. Bjerrum, *Journal of Power Sources*, 110 (2002) 1-10.
- [17] C. Chakkaravarthy, A.K.A. Waheed, H.V.K. Udupa, *Journal of Power Sources*, 6 (1981) 203-228.
- [18] K.T. Chau, Y.S. Wong, C.C. Chan, *Energy Conversion and Management*, 40 (1999) 1021-1039.

- [19] S. Yang, H. Knickle, *Journal of Power Sources*, 112 (2002) 162-173.
- [20] B. Scrosati, J. Garche, *Journal of Power Sources*, 195 (2010) 2419-2430.
- [21] R. Padbury, X. Zhang, *Journal of Power Sources*, 196 (2011) 4436-4444.
- [22] T.B. Reddy, D. Linden, McGraw-Hill, New York, 2011.
- [23] T. Huh, G. Savaskan, J.W. Evans, *Journal of Applied Electrochemistry*, 22 (1992) 916-921.
- [24] D.A.J. Rand, *Journal of Power Sources*, 4 (1979) 101-143.
- [25] D. Anderson, Nicholas School of the Environment and Earth Sciences, Duke University, May 2009, pp. 3.
- [26] O. Bitsche, G. Gutmann, *Journal of Power Sources*, 127 (2004) 8-15.
- [27] W. Tahl, Meridian International Research, 2007, pp. 2.
- [28] K. Bass, P.J. Mitchell, G.D. Wilcox, J. Smith, *Journal of Power Sources*, 35 (1991) 333-351.
- [29] C.W. Lee, K. Sathiyarayanan, S.W. Eom, M.S. Yun, *Journal of Power Sources*, 160 (2006) 1436-1441.
- [30] J.L. Zhu, Y.H. Zhou, H.X. Yang, *Journal of Power Sources*, 69 (1997) 169-173.
- [31] J.L. Zhu, Y.H. Zhou, *Journal of Power Sources*, 73 (1998) 266-270.
- [32] J.W. Diggle, A. Damjanovic, *Journal of the Electrochemical Society*, 117 (1970) 65-68.
- [33] J.W. Diggle, A. Damjanovic, *Journal of the Electrochemical Society*, 119 (1972) 1649-1658.
- [34] R.F. Thornton, E.J. Carlson, *Journal of the Electrochemical Society*, 127 (1980) 1448-1452.
- [35] J.M. Wang, L. Zhang, C. Zhang, J.Q. Zhang, *Journal of Power Sources*, 102 (2001) 139-143.
- [36] J. McBreen, E. Gannon, *Journal of Power Sources*, 15 (1985) 169-177.
- [37] Y.F. Yuan, J.P. Tu, H.M. Wu, S.F. Wang, W.K. Zhang, H. Huang, *Journal of Applied Electrochemistry*, 37 (2007) 249-253.
- [38] G.D. Wilcox, P.J. Mitchell, *Journal of Power Sources*, 32 (1990) 31-41.
- [39] C.J. Lan, C.Y. Lee, T.S. Chin, *Electrochimica Acta*, 52 (2007) 5407-5416.
- [40] Y. Sato, M. Kanda, H. Niki, M. Ueno, K. Murata, T. Shirogami, T. Takamura, *Journal of Power Sources*, 9 (1983) 147-159.
- [41] J.T. Lundquist Jr, *Journal of Membrane Science*, 13 (1983) 337-347.
- [42] C.C. Yang, J.M. Yang, C.Y. Wu, *Journal of Power Sources*, 191 (2009) 669-677.

- [43] W.G. Sunu, D.N. Bennion, *Journal of the Electrochemical Society*, 127 (1980) 2007-2016.
- [44] R. Jain, T.C. Adler, F.R. McLarnon, E.J. Cairns, *Journal of Applied Electrochemistry*, 22 (1992) 1039-1048.
- [45] C. Zhang, J.M. Wang, L. Zhang, J.Q. Zhang, C.N. Cao, *Journal of Applied Electrochemistry*, 31 (2001) 1049-1054.
- [46] E.G. Gagnon, *Journal of the Electrochemical Society*, 133 (1986) 1989-1995.
- [47] E.G. Gagnon, *Journal of the Electrochemical Society*, 138 (1991) 3173-3176.
- [48] J. McBreen, E. Gannon, *Electrochimica Acta*, 26 (1981) 1439-1446.
- [49] J. McBreen, E. Gannon, *Journal of the Electrochemical Society*, 130 (1983) 1980-1982.
- [50] Y. Sharma, M. Aziz, J. Yusof, K. Kordesch, *Journal of Power Sources*, 94 (2001) 129-131.
- [51] T.C. Adler, F.R. McLarnon, E.J. Cairns, *Journal of the Electrochemical Society*, 140 (1993) 289-294.
- [52] E.D. Farmer, A.H. Webb, *Journal of Applied Electrochemistry*, 2 (1972) 123-136.
- [53] S. Müller, F. Holzer, O. Haas, *Journal of Applied Electrochemistry*, 28 (1998) 895-898.
- [54] H. Yang, Y. Cao, X. Ai, L. Xiao, *Journal of Power Sources*, 128 (2004) 97-101.
- [55] F. Mansfeld, S. Gilman, *Journal of the Electrochemical Society*, 117 (1970) 1328-1333.
- [56] D.P. Gregory, P.C. Jones, D.P. Redfearn, *Journal of the Electrochemical Society*, 119 (1972) 1288-1292.
- [57] J. McBreen, *Journal of the Electrochemical Society*, 119 (1972) 1620-1628.
- [58] F. Mansfeld, S. Gilman, *Journal of the Electrochemical Society*, 117 (1970) 588-592.
- [59] R. Shivkumar, G. Paruthimal Kalaignan, T. Vasudevan, *Journal of Power Sources*, 55 (1995) 53-62.
- [60] R. Shivkumar, G.P. Kalaignan, T. Vasudevan, *Journal of Power Sources*, 75 (1998) 90-100.
- [61] T.P. Dirkse, R. Timmer, *Journal of the Electrochemical Society*, 116 (1969) 162-165.
- [62] E.L. Dewi, K. Oyaizu, H. Nishide, E. Tsuchida, *Journal of Power Sources*, 115 (2003) 149-152.
- [63] A.R. El-Sayed, H.S. Mohran, H.M. Abd El-Lateef, *Journal of Power Sources*, 196 (2011) 6573-6582.
- [64] J.L. Zhu, Y.H. Zhou, C.Q. Gao, *Journal of Power Sources*, 72 (1998) 231-235.
- [65] S. Martirosyan, *Journal of Power Sources*, 172 (2007) 984-987.

- [66] K. Bass, P.J. Mitchell, G.D. Wilcox, J. Smith, *Journal of Power Sources*, 39 (1992) 273-284.
- [67] E. Frackowiak, J.M. Skowronski, *Journal of Power Sources*, 73 (1998) 175-181.
- [68] C. Chiappe, D. Pieraccini, *Journal of Physical Organic Chemistry*, 18 (2005) 275-297.
- [69] G.T. Kim, S.S. Jeong, M. Joost, E. Rocca, M. Winter, S. Passerini, A. Balducci, *Journal of Power Sources*, 196 (2011) 2187-2194.
- [70] M. Galinski, A. Lewandowski, I. Stepniak, *Electrochimica Acta*, 51 (2006) 5567-5580.
- [71] H. Ohno, Hoboken, N.J. Wiley-Interscience, 2005.
- [72] B. Jastorff, K. Molter, P. Behrend, U. Bottin-Weber, J. Filser, A. Heimers, B. Ondruschka, J. Ranke, M. Schaefer, H. Schroder, A. Stark, P. Stepnowski, F. Stock, R. Stormann, S. Stolte, U. Welz-Biermann, S. Ziegert, J. Thoming, *Green Chemistry*, 7 (2005) 362-372.
- [73] J. James H. Davis, *Chemistry Letters*, 33 (2004) 1072-1077.
- [74] S.g. Lee, *Chemical Communications*, (2006) 1049-1063.
- [75] L.C. Branco, J.N. Rosa, J.J. Moura Ramos, C.A.M. Afonso, *Chemistry-A European Journal*, 8 (2002) 3671-3677.
- [76] T.L. Merrigan, E.D. Bates, S.C. Dorman, J.H. Davis Jr, *Chemical Communications*, (2000) 2051-2052.
- [77] P. Bonhôte, A.P. Dias, N. Papageorgiou, K. Kalyanasundaram, M. Grätzel, *Inorganic Chemistry*, 35 (1996) 1168-1178.
- [78] D.R. MacFarlane, P. Meakin, J. Sun, N. Amini, M. Forsyth, *The Journal of Physical Chemistry B*, 103 (1999) 4164-4170.
- [79] H. Matsumoto, M. Yanagida, K. Tanimoto, M. Nomura, Y. Kitagawa, Y. Miyazaki, *Chemistry Letters*, 29 (2000) 922-923.
- [80] A. Lewandowski, A. Swiderska-Mocek, *Journal of Power Sources*, 194 (2009) 601-609.
- [81] W. Xu, L.M. Wang, R.A. Nieman, C.A. Angell, *The Journal of Physical Chemistry B*, 107 (2003) 11749-11756.
- [82] J.M. Pringle, J. Golding, K. Baranyai, C.M. Forsyth, G.B. Deacon, J.L. Scott, D.R. MacFarlane, *New Journal of Chemistry*, 27 (2003) 1504-1510.
- [83] S.V. Dzyuba, R.A. Bartsch, *ChemPhysChem*, 3 (2002) 161-166.
- [84] H. Vogel, *Physikalische Zeitschrift*, 22 (1921) 645-646.
- [85] G.S. Fulcher, *Journal of the American Ceramic Society*, 8 (1925) 339-355.

- [86] G. Tammann, W. Hesse, *Zeitschrift für anorganische und allgemeine Chemie*, 156 (1926) 245-257.
- [87] H. Liu, Y. Liu, J. Li, *Physical Chemistry Chemical Physics*, 12 (2010) 1685-1697.
- [88] R. Seddon Kenneth, A. Stark, M.J. Torres, *Pure and Applied Chemistry*, 72 (2000) 2275-2287.
- [89] H. Tokuda, K. Hayamizu, K. Ishii, M.A.B.H. Susan, M. Watanabe, *The Journal of Physical Chemistry B*, 109 (2005) 6103-6110.
- [90] M. Zistler, P. Wachter, P. Wasserscheid, D. Gerhard, A. Hinsch, R. Sastrawan, H.J. Gores, *Electrochimica Acta*, 52 (2006) 161-169.
- [91] N. Tachikawa, N. Serizawa, Y. Katayama, T. Miura, *Electrochimica Acta*, 53 (2008) 6530-6534.
- [92] A.C. Herath, J.Y. Becker, *Electrochimica Acta*, 55 (2010) 8319-8324.
- [93] Y. Yoshida, O. Baba, C. Larriba, G. Saito, *The Journal of Physical Chemistry B*, 111 (2007) 12204-12210.
- [94] R. Hagiwara, K. Matsumoto, Y. Nakamori, T. Tsuda, Y. Ito, H. Matsumoto, K. Momota, *Journal of the Electrochemical Society*, 150 (2003) D195-D199.
- [95] C. Reichardt, *Organic Process Research & Development*, 11 (2007) 105-113.
- [96] R. Byrne, S. Coleman, S. Gallagher, D. Diamond, *Physical Chemistry Chemical Physics*, 12 (2010) 1895-1904.
- [97] B.M. Quinn, Z. Ding, R. Moulton, A.J. Bard, *Langmuir*, 18 (2002) 1734-1742.
- [98] K. Murase, K. Nitta, T. Hirato, Y. Awakura, *Journal of Applied Electrochemistry*, 31 (2001) 1089-1094.
- [99] M.J. Deng, P.Y. Chen, I.W. Sun, *Electrochimica Acta*, 53 (2007) 1931-1938.
- [100] T. Tsuda, R. Hagiwara, *Journal of Fluorine Chemistry*, 129 (2008) 4-13.
- [101] J.D. Holbrey, W.M. Reichert, R.P. Swatloski, G.A. Broker, W.R. Pitner, K.R. Seddon, R.D. Rogers, *Green Chemistry*, 4 (2002) 407-413.
- [102] P.Y. Chen, M.J. Deng, D.X. Zhuang, *Electrochimica Acta*, 54 (2009) 6935-6940.
- [103] W. Simka, D. Puszczuk, G. Nawrat, *Electrochimica Acta*, 54 (2009) 5307-5319.
- [104] O. Raz, G. Cohn, W. Freyland, O. Mann, Y. Ein-Eli, *Electrochimica Acta*, 54 (2009) 6042-6045.

- [105] T. Kuboki, T. Okuyama, T. Ohsaki, N. Takami, *Journal of Power Sources*, 146 (2005) 766-769.
- [106] G.B. Appetecchi, M. Montanino, A. Balducci, S.F. Lux, M. Winterb, S. Passerini, *Journal of Power Sources*, 192 (2009) 599-605.
- [107] M. Li, L. Yang, S. Fang, S. Dong, Y. Jin, S.-i. Hirano, K. Tachibana, *Journal of Power Sources*, 196 (2011) 6502-6506.
- [108] Y. Yan, Y.X. Yin, S. Xin, J. Su, Y.G. Guo, L.J. Wan, *Electrochimica Acta*, 91 (2013) 58-61.
- [109] M. Wang, Z. Shan, J. Tian, K. Yang, X. Liu, H. Liu, K. Zhu, *Electrochimica Acta*, 95 (2013) 301-307.
- [110] S.S. Zhang, *Electrochimica Acta*, 97 (2013) 226-230.
- [111] S. Menne, J. Pires, M. Anouti, A. Balducci, *Electrochemistry Communications*, 31 (2013) 39-41.
- [112] Z. Ma, J. Kan, *Synthetic Metals*, 174 (2013) 58-62.
- [113] Y. Zhao, H. Wang, G. Gao, L. Qi, *Ionics*, 19 (2013) 1595-1602.
- [114] G. Cohn, Y. Ein-Eli, *Journal of Power Sources*, 195 (2010) 4963-4970.
- [115] S. Menne, R.S. Kühnel, A. Balducci, *Electrochimica Acta*, 90 (2013) 641-648.
- [116] N. Böckenfeld, M. Willeke, J. Pires, M. Anouti, A. Balducci, *Journal of the Electrochemical Society*, 160 (2013) A559-A563.
- [117] L.G. Bettini, M. Galluzzi, A. Podestà, P. Milani, P. Piseri, *Carbon*, 59 (2013) 212-220.
- [118] M. Anouti, L. Timperman, *Physical Chemistry Chemical Physics*, 15 (2013) 6539-6548.
- [119] E. Iwama, P.L. Taberna, P. Azais, L. Brégeon, P. Simon, *Journal of Power Sources*, 219 (2012) 235-239.
- [120] M.M. Hantel, A. Płatek, T. Kaspar, R. Nesper, A. Wokaun, R. Kötz, *Electrochimica Acta*, 110 (2013) 234-239.
- [121] M. Díaz, A. Ortiz, M. Vilas, E. Tojo, I. Ortiz, *International Journal of Hydrogen Energy*, 39 (2014) 3970-3977.
- [122] J. Mališ, P. Mazúr, J. Schauer, M. Paidar, K. Bouzek, *International Journal of Hydrogen Energy*, 38 (2013) 4697-4704.
- [123] S. Liu, L. Zhou, P. Wang, Z. Shao, B. Yi, *Journal of Materials Chemistry A*, 1 (2013) 4423-4426.

- [124] W. Weng, Z. Zhang, J.A. Schlueter, K. Amine, *Electrochimica Acta*, 92 (2013) 392-396.
- [125] S. Ferrari, E. Quartarone, P. Mustarelli, A. Magistris, M. Fagnoni, S. Protti, C. Gerbaldi, A. Spinella, *Journal of Power Sources*, 195 (2010) 559-566.
- [126] S. Ferrari, E. Quartarone, C. Tomasi, D. Ravelli, S. Protti, M. Fagnoni, P. Mustarelli, *Journal of Power Sources*, 235 (2013) 142-147.
- [127] S. Zhang, Z. Chen, X. Qi, Y. Deng, *New Journal of Chemistry*, 36 (2012) 1043-1050.
- [128] M. Kar, B. Winther-Jensen, M. Forsyth, D.R. MacFarlane, *Physical Chemistry Chemical Physics*, 15 (2013) 7191-7197.
- [129] J.C. Forgie, S. El Khakani, D.D. MacNeil, D. Rochefort, *Physical Chemistry Chemical Physics*, 15 (2013) 7713-7721.
- [130] K. Tsunashima, H. Taguchi, F. Yonekawa, *ECS Transactions*, 50 (2013) 419-424.
- [131] J. Xiang, F. Wu, R. Chen, L. Li, H. Yu, *Journal of Power Sources*, 233 (2013) 115-120.
- [132] O.N. Kalugin, I.V. Voroshylova, A.V. Riabchunova, E.V. Lukinova, V.V. Chaban, *Electrochimica Acta*, 105 (2013) 188-199.
- [133] D. Xu, Z.-l. Wang, J.-j. Xu, L.-l. Zhang, X.-b. Zhang, *Chemical Communications*, 48 (2012) 6948-6950.
- [134] T.J. Simons, A.A.J. Torriero, P.C. Howlett, D.R. MacFarlane, M. Forsyth, *Electrochemistry Communications*, 18 (2012) 119-122.
- [135] M.D. Stoller, R.S. Ruoff, *Energy & Environmental Science*, 3 (2010) 1294-1301.
- [136] M.J. Deng, P.C. Lin, J.K. Chang, J.M. Chen, K.T. Lu, *Electrochimica Acta*, 56 (2011) 6071-6077.
- [137] A.J. Bard, L.R. Faulkner, *Electrochemical Methods: Fundamentals and Applications*, 2nd Edition, John Wiley & Sons, New York, 2001.
- [138] M. J. Frisch, G. W. Trucks, H. B. Schlegel, G. E. Scuseria, M. A. Robb, J. R. Cheeseman, G. Scalmani, B.M. V. Barone, G. A. Petersson, H. Nakatsuji, M. Caricato, X. Li, H. P. Hratchian, A. F. Izmaylov, J. Bloino, G. Zheng, J. L. Sonnenberg, M. Hada, M. Ehara, K. Toyota, R. Fukuda, J. Hasegawa, M. Ishida, T. Nakajima, Y. Honda, O. Kitao, H. Nakai, T. Vreven, J. A. Montgomery, Jr., J. E. Peralta, F. Ogliaro, M. Bearpark, J. J. Heyd, E. Brothers, K. N. Kudin, V. N. Staroverov, R. Kobayashi, J. Normand, K. Raghavachari, A. Rendell, J. C. Burant, S. S. Iyengar, J. Tomasi, M. Cossi, N. Rega, J. M. Millam, M. Klene, J. E. Knox, J. B. Cross, V. Bakken, C. Adamo, J. Jaramillo, R. Gomperts, R. E. Stratmann, O. Yazyev, A. J.

Austin, R. Cammi, C. Pomelli, J. W. Ochterski, R. L. Martin, K. Morokuma, V. G. Zakrzewski, G. A. Voth, P. Salvador, J. J. Dannenberg, S. Dapprich, A. D. Daniels, Ö. Farkas, J. B. Foresman, J. V. Ortiz, J. Cioslowski, and D. J. Fox, Gaussian, Inc., Wallingford, CT, 2009.

[139] K. Xu, *Chemical Reviews*, 104 (2004) 4303-4418.

[140] L. Cammarata, S.G. Kazarian, P.A. Salter, T. Welton, *Physical Chemistry Chemical Physics*, 3 (2001) 5192-5200.

[141] J.R. Scherer, in: R. J. H. Clark, R.E. Hester (Eds.), Heyden, London, 1978.

[142] M. Pavlov, P.E.M. Siegbahn, M. Sandström, *The Journal of Physical Chemistry A*, 102 (1998) 219-228.

[143] Z. Liu, S. Zein El Abedin, F. Endres, *Electrochimica Acta*, 89 (2013) 635-643.

[144] F. Endres, O. Hofft, N. Borisenko, L.H. Gasparotto, A. Prowald, R. Al-Salman, T. Carstens, R. Atkin, A. Bund, S. Zein El Abedin, *Physical Chemistry Chemical Physics*, 12 (2010) 1724-1732.

[145] X. Qian, B. Han, Y. Liu, H. Yan, R. Liu, *Journal of Solution Chemistry*, 24 (1995) 1183-1189.

[146] I. Persson, *Acta Chemica Scandinavica A*, 36 (1982) 7-13.

[147] M. Monev, L. Mirkova, I. Krastev, H. Tsvetkova, S. Rashkov, W. Richtering, *Journal of Applied Electrochemistry*, 28 (1998) 1107-1112.

[148] Z. Mao, S. Srinivasan, A.J. Appleby, *Journal of Applied Electrochemistry*, 22 (1992) 693-698.

[149] D.G. Ivey, Series book: *Microscopy: Science, Technology, Applications and Education* (A. Mendez-Vilas, J.Diaz (Eds.)), 2010, pp. 1219-1231.

[150] M.J. Trahan, S. Mukerjee, E.J. Plichta, M.A. Hendrickson, K.M. Abraham, *Journal of The Electrochemical Society*, 160 (2013) A259-A267.

[151] S.L. Chou, Y.X. Wang, J. Xu, J.Z. Wang, H.K. Liu, S.X. Dou, *Electrochemistry Communications*, 31 (2013) 35-38.